

ASSESSMENT AND IMPROVEMENT OF ANALYTICAL EQUATIONS FOR  
BACKWARD CAN EXTRUSION

A THESIS SUBMITTED TO  
THE GRADUATE SCHOOL OF NATURAL AND APPLIED SCIENCES  
OF  
THE MIDDLE EAST TECHNICAL UNIVERSITY

BY

143537

METE EGEMEN

T.C. YÜKSEKÖĞRETİM BAKANLIĞI  
DOKÜMANTASYON BİRİMİ

IN PARTIAL FULFILLMENT OF THE REQUIREMENTS FOR THE DEGREE  
OF

MASTER OF SCIENCE

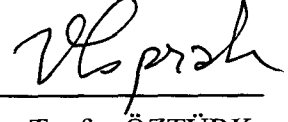
IN

THE DEPARTMENT OF MECHANICAL ENGINEERING

- 143537 -

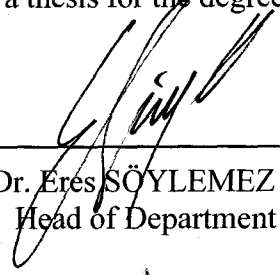
JUNE 2003

Approval of the Graduate School of Natural and Applied Sciences




Prof. Dr. Tayfur ÖZTÜRK  
Director

I certify that this thesis satisfies all the requirements as a thesis for the degree of Master of Science.



Prof. Dr. Eres SÖYLEMEZ  
Head of Department

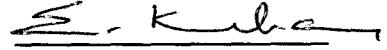
This is to certify that we have read this thesis and that in our opinion it is fully adequate, in scope and quality, as a thesis for the degree of Master of Science.




Prof. Dr. A. Erman Tekkaya  
Supervisor

Examining Committee Members

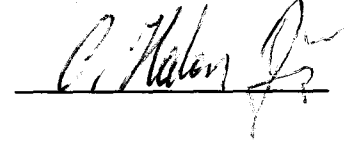
Prof. Dr. S. Engin Kılıç (Chairman)




Prof. Dr. A. Erman Tekkaya (Supervisor)



Assoc. Prof. Dr. Hakan Gür (METU  
Metallurgical and Materials Eng. Dept.)



Assoc. Prof. Dr. Suat Kadioğlu



Asst. Prof. Dr. Serkan Dağ



## **ABSTRACT**

### **ASSESSMENT AND IMPROVEMENT OF ANALYTICAL METHODS TO PREDICT BACKWARD CAN EXTRUSION FORCES**

**Egemen, Mete**

**M.S., Department of Mechanical Engineering**

**Supervisor: Prof. Dr.-Ing. A. Erman Tekkaya**

**June 2003, 190 pages**

Various well-known force equations for backward can extrusion process are evaluated by means of precise finite element computations. For backward can extrusion the upper-bound models of Avitzur, Kudo and Hoogenboom and Dipper's elementary plasticity solution are considered. The effect of the assumptions is studied. The non-hardening solutions are assessed by finite element results. The definition of total equivalent strain and flow stress for the process are done and the non-hardening equations are modified for hardening materials. The results obtained are compared with finite element analysis results and the success of each formulation is assessed. The effect of friction and the geometry are also considered.

**Keywords: Cold Forging, Force Prediction, Finite Element Method**

## ÖZ

# GERİYE ÇANAK EKSTURÜZYON KUVVETİ TAHMİNİ İÇİN ANALİTİK DENKLEMLERİN DEĞERLENDİRİLMESİ VE GELİŞTİRİLMESİ

Egemen, Mete

Yüksek Lisans, Makina Mühendisliği Bölümü

Tez Yöneticisi: Prof. Dr. A. Erman Tekkaya

Haziran 2003, 190 sayfa

Geri ekstürüzyon prosesi için bilinen çeşitli kuvvet denklemleri, sonlu elemanlar hesaplamalarıyla değerlendirilmiştir. Geri ekstürüzyon için Avitzur'un, Hoogenboom'un ve Kudo'nun üst sınır metodları ve Dipper'in temel plastisite teorisi çözümü ele alınmıştır. Varsayımların etkisi incelenmiştir. Sertleşmeyen malzemeler için yapılan çözümler sonlu elemanlar metodu ışığında değerlendirilmiştir. Toplam eşdeğer plastik genleme ve akma gerilmesi tanımlaması yapılmış ve sertleşmeyen malzemeler için olan çözümler sertleşen malzemeler için değiştirilmiştir. Elde edilen sonuçlar sonlu elemanlar yöntemi ile elde edilen sonuçlarla karşılaştırılmıştır ve her çözümün etkinliği incelenmiştir. Çalışmada sürtünme ve geometrinin etkisi de dikkate alınmıştır.

Anahtar Kelimeler: Soğuk Dövme, Kuvvet Tahmini, Sonlu Eleman Metodu





*To My Family*

## ACKNOWLEDGMENTS

I would like to express my deepest gratitude and appreciation to my supervisor Prof. Dr.-Ing. A . Erman Tekkaya, who inspired, encouraged and supported me for this study.

I would like to thank to my colleague Muhsin Öcal for his support and contribution

I would like to thank Bahadır Koçaker for being such a great friend and being with me in many memorable moments. I would like to thank Gülşah Gümrükçü for her positive energy that motivated me to write this thesis.

I would like to thank Özgür Koçak for his understanding and support as a friend and a roommate. I would like to thank Ahmet Kurt and Kürşat Kayatürk for their patience and support.

I would like to thank, Oya, Çağrı, Erge, Erkan, Murat, Nagihan Canderim and Çiğdem who made my assistantship in METU a great experience. I am happy to be their assistant and friend as well.

To my mum who believed in me and was always there for me whenever I need. Your love and smile is a bliss. To my dad whose experience and love always gives me strength and confidence. To my sister for her love, patience, and common sense...you are loved deeply.

## TABLE OF CONTENTS

ABSTRACT.....	iii
ÖZ.....	iv
ACKNOWLEDGEMENT.....	vi
TABLE OF CONTENTS.....	vii
LIST OF FIGURES.....	xii
LIST OF TABLES.....	xviii

### CHAPTER

1. INTRODUCTION.....	1
1.1. Metal Forming.....	1
1.2. Backward Can Extrusion.....	4
1.3. Tool Design and Forming Force Prediction.....	5
1.4. The Aim and Scope of the Study.....	6
2. LITERATURE SURVEY.....	8
2.1. Introduction.....	8
2.2. Methods of Analysis in Metal Forming.....	8
2.2.1. Analytical Methods.....	9
2.2.1.1 Elementary Methods.....	9
2.2.1.2 Energy Methods.....	10

2.2.2. Empirical Methods.....	10
2.2.3. Numerical Methods.....	11
2.3. Forming Force Formulations Available in the Literature .....	12
2.4. Friction Models in Metal Forming.....	16
2.5. Conclusion .....	20
3. ASSESSED ANALYTICAL FORMULATIONS.....	22
3.1. Introduction .....	22
3.2. Elementary Methods .....	22
3.2.1. Dipper's Solution .....	22
3.3. Upper Bound Solution .....	27
3.3.1. Late Stage.. .....	29
3.3.1.1 Two-Zone Velocity Field .....	29
3.3.1.2 Three Zone Velocity Field with Thick-Walled Solution...	39
3.3.1.3 Three Zone Velocity Field with Thick-Walled Solution...	54
3.3.2. Early Stage .....	66
3.3.2.1 Spherical Velocity Field .....	67
3.3.2.2 Three Zone Velocity Field with Thick-Walled Solution...	77
3.3.2.3 Three Zone Velocity Field with Thick-Walled Solution...	82

4. FINITE ELEMENT METHOD .....	85
4.1. Introduction .....	85
4.2. Theoretical Background of Finite Element Method.....	85
4.2.1. Finite Element Approach for Large Plastic Deformation.....	86
4.2.2. Elastic-Plastic Solution by Updated Lagrangian Approach ....	88
4.2.3. Numerical Solutions of Equations .....	92
4.2.3.1 Newton Raphson Method.....	93
4.2.3.2 Convergence Limits.....	94
4.3. Finite Element Model of Backward Can Extrusion .....	96
4.3.1. Geometry .....	96
4.3.2. Boundary Conditions .....	98
4.3.3. Material Properties.....	98
4.4. Convergence Study .....	99
4.4.1. Element Size .....	99
4.4.2. Friction Model .....	102
4.5. Verification of Finite Element Model with Experimental Results.	103
5. ASSESSMENT OF ANALYTICAL EQUATIONS FOR NON-HARDENING MATERIAL.....	109
5.1. Introduction.....	109
5.2. Modification of Dipper's Solution.....	109
5.3. The Comparison of Thick and Thin Walled Solutions for Three Zone Velocity Field .....	113

5.4. The Comparison of Analytical Equations with FEA Results .....	122
5.4.1. The Comparison of Analytical Equations with FEA without Friction .....	123
5.4.2. The Comparison of Analytical Equations with FEA with Friction .....	128
5.4.3. Transition from "Early Stage" to "Late Stage" .....	132
5.5. The Effect of Initial Geometry .....	134
6. ASSESSMENT OF ANALYTICAL EQUATIONS FOR HARDENING MATERIALS.....	139
6.1. Introduction.....	139
6.2. Definition of Strain and Flow Stress.....	139
6.3. The Modifications for Two-Zone Velocity Field Solution.....	140
6.4. The Modifications for Spherical Velocity Field Solution.....	145
6.5. The Modifications for Three-Zone Velocity Field Solution.....	147
6.5.1. Late Stage Solution.....	147
6.5.2. Early Stage Solution .....	149
6.6. Comparison of Results .....	149
6.6.1. The Comparison of Analytical Equations with FEA without Friction.....	150
6.6.2. The Comparison of Analytical Equations with FEA with Friction.....	155
6.7. The Effect of Initial Geometry .....	161

7. CONCLUSION AND DISCUSSION .....	164
8. FURTHER RECOMMENDATIONS.....	168
REFERENCES .....	169
APPENDICES	
A. Upper Bound Solution for Upsetting .....	172
B. Material Data .....	176
C. Results for Hardening Materials.....	178
D. The Geometry of Punch for Verification Simulations.....	181
E. Visual Basic Code.....	185



## LIST OF FIGURES

### FIGURES

1.1 Backward Can Extrusion .....	4
2.1 Methods of Analysis in Metal Forming .....	8
2.2 Visio plasticity .....	11
2.3 Relationships of Normal and Shear Stress for Coulomb Model .....	18
2.4 Friction stress as a function normal pressure and friction factor .....	20
3.1 Dipper's Velocity Field.....	23
3.2 Double Upsetting Process .....	23
3.3 Velocity Field for Late Stage .....	29
3.4 Two-Zone Velocity Field.....	30
3.5 Velocity Components.....	31
3.6 Three Zone Velocity Field .....	40
3.7 Velocity Field for Early Stage .....	67
3.8 Spherical Velocity Field.....	68
3.9 Velocity Discontinuities.....	68
3.10 Velocities for Deformation Zone .....	69



3.11 The Shear and Friction Planes for Early Stage .....	69
3.12 Three-Zone Velocity Field for Early Stage.....	77
4.1 Newton-Raphson Method .....	93
4.2 Convergence Study .....	95
4.3 Backward Can Extrusion 2-D Model.....	97
4.4 Finite Element Model for Backward Can Extrusion.....	97
4.5 Boundary Conditions for Finite Element Model.....	98
4.6 Flow Curve for Non-hardening Material .....	99
4.7 Remeshing Problems.....	100
4.8 Effect of Maximum Element Edge Length .....	101
4.9 Smoothing of the Curve .....	102
4.10 Finite Element Model of the punch used by Schmitt.....	103
4.11 Comparison of Experimental Data with FEA for 16% Area Reduction ( $b_0/d_0=1.07$ ).....	105
4.12 Comparison of Experimental Data with FEA for 16% Area Reduction ( $b_0/d_0=0.67$ ).....	105
4.13 Comparison of Experimental Data with FEA for 16% Area Reduction ( $b_0/d_0=0.37$ ).....	106
4.14 Comparison of Experimental Data with FEA for 57% Area Reduction ( $b_0/d_0=1.07$ ).....	107
4.15 Comparison of Experimental Data with FEA for 57% Area Reduction ( $b_0/d_0=0.67$ ).....	107

4.16 Comparison of Experimental Data with FEA for 57% Area Reduction ( $b_0/d_0=0.37$ ).....	108
5.1 Comparison of Deformation Power for Zone II.....	117
5.2 Error Comparison of Deformation Power for Zone II.....	118
5.3 Comparison of Thin and Thick Walled Solutions for Three-Zone Velocity Field (80% Area Reduction) .....	119
5.4 Comparison of Thin and Thick Walled Solutions for Three-Zone Velocity Field (60% Area Reduction) .....	119
5.5 Comparison of Thin and Thick Walled Solutions for Three-Zone Velocity Field (40% Area Reduction) .....	120
5.6 Comparison of Thin and Thick Walled Solutions for Three-Zone Velocity Field for 80% Area Reduction ( $m=0.2$ ) .....	121
5.7 Comparison of Thin and Thick Walled Solutions for Three-Zone Velocity Field for 60% Area Reduction ( $m=0.2$ ) .....	121
5.8 Comparison of Thin and Thick Walled Solutions for Three-Zone Velocity Field for 40% Area Reduction ( $m=0.2$ ) .....	122
5.9 Total Power Comparison for 40% Area Reduction .....	124
5.10 Total Power Comparison for 60% Area Reduction .....	125
5.11 Total Power Comparison for 80% Area Reduction .....	126
5.12 Total Power Comparison for 80% Area Reduction (Early Stage) .....	127
5.13 Total Power Comparison for 80% Area Reduction (Late Stage) .....	128
5.14 Total Power Comparison for 40% Area Reduction ( $m=0.1$ ) .....	129

5.15 Total Power Comparison for 60% Area Reduction ( $m=0.1$ ) .....	130
5.16 Total Power Comparison for 80% Area Reduction ( $m=0.1$ ) .....	130
5.17 Total Power Comparison for 60% Area Reduction ( $m=0.2$ ) .....	131
5.18 Total Power Comparison for 80% Area Reduction ( $m=0.2$ ) .....	132
5.19 Normalized Punch Force-Displacement Curve for a Non-hardening Material .....	133
5.20 Transformation from Early to Late Stage .....	134
5.21 Effect of Initial Billet Length ( $m=0$ ) .....	135
5.22 Effect of Initial Billet Length ( $m=0.1$ ) .....	137
5.23 Effect of Initial Billet Length ( $m=0.2$ ) .....	137
5.24 Effect of Initial Billet Length ( $m=0.3$ ) .....	138
6.1 Determination of Total Eq. Plastic Strain for Deforming Zone.....	141
6.2 Total Eq. Pl. Strain for Late Stage .....	141
6.3 Two-Zone Velocity Field.....	142
6.4 Determination of Total Eq. Plastic Strain for Rigid Zone .....	143
6.5 Total Eq. Pl. Strain for Early Stage.....	144
6.6 Spherical Velocity Field.....	145
6.7 Velocity Discontinuities for Spherical Velocity Field.....	146
6.8 Three-Zone Velocity Field.....	147
6.9 Three-Zone Velocity Field with a dead-zone_ .....	149
6.10 Flow Curves for the Materials .....	150

6.11 Total Power Comparison for 40% Area Reduction (Late Stage).....	151
6.12 Total Power Comparison for 60% Area Reduction (Late Stage).....	152
6.13 Total Power Comparison for 80% Area Reduction (Late Stage).....	152
6.14 Total Power Comparison for 80% Area Reduc. ( $b_0=0.37$ ) (Late Stage)	153
6.15 Total Power Comparison for 40% Area Reduction (Early Stage) .....	154
6.16 Total Power Comparison for 60% Area Reduction (Early Stage) .....	154
6.17 Total Power Comparison for 80% Area Reduction (Early Stage) .....	155
6.18 Total Power Comparison for 40% Area Reduction for Late Stage ( $m=0.1$ ) .....	156
6.19 Total Power Comparison for 60% Area Reduction for Late Stage ( $m=0.1$ ). .....	156
6.20 Total Power Comparison for 80% Area Reduction for Late Stage ( $m=0.1$ ) .....	157
6.21 Total Power Comparison for 60% Area Reduction for Late Stage ( $m=0.2$ ) .....	157
6.22 Total Power Comparison for 80% Area Reduction for Late Stage ( $m=0.2$ ) .....	158
6.23 Total Power Comparison for 40% Area Reduction for Early Stage ( $m=0.1$ ) .....	159
6.24 Total Power Comparison for 60% Area Reduction for Early Stage ( $m=0.1$ ) .....	159
6.25 Total Power Comparison for 80% Area Reduction for Early Stage ( $m=0.1$ ).....	160

6.26 Total Power Comparison for 60% Area Reduction for Early Stage ( $m=0.2$ ).....	160
6.27 Total Power Comparison for 80% Area Reduction for Early Stage ( $m=0.2$ ).....	161
6.28 Effect of Initial Length Billet Length ( $m=0$ ) .....	162
6.29 Effect of Initial Length Billet Length ( $m=0.2$ ) .....	162
6.30 Effect of Initial Length Billet Length ( $m=0.2$ ) .....	163
A.1 Velocity Field for Axis-symmetric Upsetting.....	173
B.1 Flow Curves .....	177
C.1 Total Power Comparison for 80% Area Reduction for Late Stage for Ck10 ( $m=0.2$ ).....	178
C.2 Total Power Comparison for 60% Area Reduction for Late Stage for Ck10 ( $m=0.2$ ).....	179
C.3 Total Power Comparison for 80% Area Reduction for Early Stage for Ck10 ( $m=0.2$ ).....	179
C.4 Total Power Comparison for 60% Area Reduction for Early Stage for Ck10 ( $m=0.2$ ).....	180
D.1 Punch Geometry for Experimental Verification .....	181
D.2 Flat Punch.....	183
E.1 Material Database Menu.....	186
E.2 Main Menu .....	187
E.3 Process Data Menu .....	189
E.4 Process Results Menu.....	190
E.5 Excel Worksheet.....	190

## LIST OF TABLES

### TABLES

4.1 Dimensions of Initial Billet .....	104
B.1 Material Data.....	176
D.1 Dimensions of the Nosed Punch .....	182
D.2 Initial Billet Dimensions for Verification of FEA Results.....	182
D.3 Dimensions of the Flat Punch .....	183
D.4 Initial Billet Dimensions for Flat Punch .....	184



## **CHAPTER 1**

### **INTRODUCTION**

#### **1.1 Metal Forming**

Metal forming is a group of processes in which the material is deformed and given a required shape without a change in mass or composition of the material. The advantages of metal forming processes are:

- High material utilization
- High productivity with short production times
- High dimensional and shape accuracy within certain tolerances
- Superior mechanical material properties

High production rate is one of the most common properties of metal forming processes. Other common properties of such methods are as follows:

- The loads are very high and they result in high stress values in the material. The stresses are in 50-2500 N/mm<sup>2</sup> range depending on the selected process and material.
- The tools and dies are very large, heavy and costly due to the need for high loads. Especially for cold forging, the processes mainly require highly skilled, experienced workers and well-equipped workshops due to the tight tolerances.

- The high expense of the tooling and work power requires high amount of production quantities in considerably shorter times for the process to be feasible

The metal forming processes can be grouped according to the dimensions of the initial workpiece (Tekkaya, 2001(b)):

- **Bulk Metal Forming:** Involves multi-axial compressive loading with high forces. The amount of change of dimensions of the initial workpiece is high. The material deforms in all spatial directions.
- **Sheet Metal Forming:** Involves considerably lower forces and small changes in the initial dimensions of the workpiece. The amount of rigidity of the tools and machines are low compared to the bulk metal forming processes. The deformation mainly takes place in one of the directions.

The metal forming processes can also be grouped according to the temperature that the deformation takes place (Tekkaya, 2001(b)):

- **Cold Forming:** Plastic deformation that takes place under the recrystallization temperature of the material, and is considered as cold forming. The process is usually utilized at room temperature but slightly elevated temperatures are also considered as cold forming and they provided increased ductility and lower strength. Cold forming has various advantages that make this kind of processes very favorable:
  1. Heating is not required.
  2. The surface finish is better compared to hot forming which results in little or no machining after the process
  3. Better dimensional accuracy
  4. The material processes such as wear, strength and fatigue are improved due to strain hardening.
  5. Directional properties are imparted



- **Hot Forming:** Plastic deformation of the material at temperatures above recrystallization temperature of the material is called as hot forming. The recrystallization temperature is a material dependent property so the hot working temperature changes with material. The recrystallization temperature of steel is around 1200°C whereas tin is close to hot forming conditions at room temperature. The elevated temperatures increase the formability of the material by reducing its strength and increasing the ductility. The temperature increase in the material eliminates the effects of strain hardening. As a consequence of this fact the workpiece that is formed has no significant increase in its strength or hardness. Severe deformations can be utilized since the shape can be altered drastically without any fracture. The forces that are required are considerably low.
  
- **Warm Forming:** Deformation at temperatures that are intermediate to hot and cold forming is called warm forming(DeGarmo(1997)):
  1. Certain amount of heating is required.
  2. The use of higher temperatures compared to cold forming expands the range of materials and geometries that can be formed.
  3. Compared to cold forming ductility of the material is increased.
  4. Reduced load on the tooling and equipment compared to cold forming.
  5. Due to less heating compared to hot forming, there is less decarburization.
  6. The dimensional accuracy is better compared to hot forming and the amount of finish machining is reduced.
  7. Warm regime generally requires less energy than hot working.

## 1.2 Backward Can Extrusion

One of the most commonly utilized metal forming process is backward can extrusion (Figure 1.1). The process of backward can extrusion (also named as impact extrusion) is utilized to produce hollow shells from solid rods or disks. The process can be utilized in all temperature ranges. It is a non-steady bulk forming process.

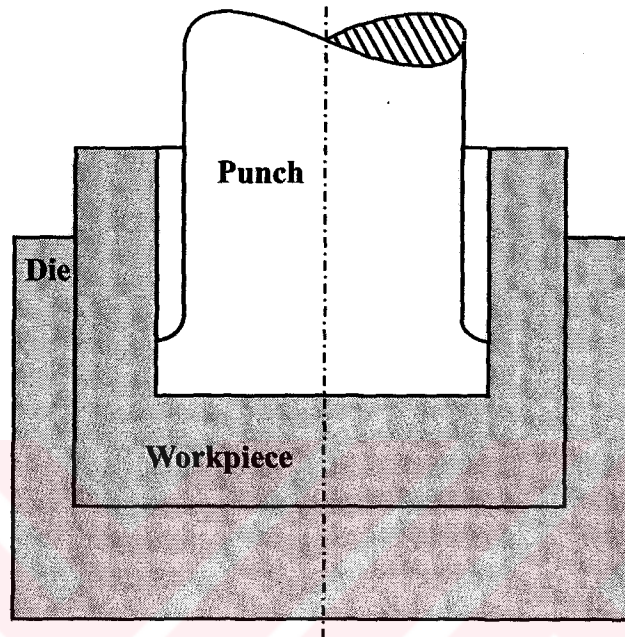


Figure 1.1 Backward Can Extrusion

The materials that are used in this process are carbon and alloy steels, aluminum alloys, copper alloys, magnesium alloys and titanium alloys.

The workpiece is placed into the die cavity and the punch is forced into the material. As the punch penetrates, the gap between the die and the punch is filled with the material that is moving in the opposite direction of the punch.

The area under the punch displacement vs. punch force curve is used to calculate the total amount of energy that is required for the formation of the final geometry. The value of the strain and the flow stress alter from point to point in the material. As a result of this fact, an average strain and a flow stress have to be defined in order to describe the process.

The total load in the backward can extrusion process is influenced by different process variables (Avitzur, 1983):

- **Area Reduction:** The ratio of final area of the ring ( $A_0-A_1$ ) to the area of the initial billet ( $A_0$ ) is named as the area reduction. The area reduction increases the total amount of deformation which results in an increase of the total load.
- **Die Geometry:** The material flow is influenced by the die geometry. The effective strain distribution and the flow stress, the angle of the tip of the die effects the shear components of the extrusion load. The change in the length of the die alters the die friction force load due to the increase or decrease in the total contact area between the die and the material.
- **Lubrication:** An effective lubrication is very useful for the reduction of the friction force between the die-workpiece and punch-workpiece interface.
- **The Workpiece Material:** The flow stress of the material is effective for the total load calculation. The knowledge of history of the material (pre-heating, pre-deformation) is very vital for the calculation of the total force.

### **1.3 Tool Design and Forming Force Prediction**

The design of the tooling is one of the main problems of the production by backward can extrusion. The high cost of the die makes die design and life a critical issue. The design and utilization of proper tooling is vital for the success and the reliability of the production. If the critical factors are not taken into consideration, tools are very likely to fail.

The failure of the tooling is due to several factors such as unsuitable tooling, improper lubrication and inadequate tool material. Gardner (1958) states that the orifice (annular gap) of backward extrusion process should be short enough not to

cause any funnel effect which will result in unequal material flow, choking and increased friction. During the deformation the material flows through the orifice between the punch and the die. For this reason, no restrictions should be present in the direction of flow. There should not be any sharp corners that will hinder the flow of the material. It is always preferable to have geometries with fillets and rounded corners. The bottom angle of the punch should to be designed in such a way that it will ease the formation.

The punch is under a compressive load. The ratio of slenderness is an important factor for the design of the punch in order to reduce the risk of buckling. The buckling ratio sets a limit on the length of the punch that will be produced. In the production of the parts with backward can extrusion, the punch should be long enough. It should be supported from one end and tends to float. For this particular reason it is always beneficial to aim symmetry in the parts that are designed.

The length of a formed part should be within the allowable limits. As the length increases so does the tendency to float which results in the variation of the wall thickness.

There are many formulations for force calculation for backward can extrusion in the literature for various types of materials such as steel, lead and aluminum. The formulations that are available in the literature are explained in Chapter 2 and the formulations that are used in this study are explained in detail in Chapter 3.

#### **1.4 The Aim and Scope of the Study**

The wide usage of backward can extrusion in industry makes the force calculation for the process critical. For many years several scientists have developed models and tried to predict the force necessary for the deformation. All of these solutions have certain advantages and drawbacks. The aim of this study is to compare some

common available solutions and mention their advantages and disadvantages within specified limits.

Furthermore by using FEA, we try to improve or diminish pitfalls of the solutions proposed by the scientists. The FE software used for this study is MSC/AutoForge which enables the calculation of the necessary results for the process. In addition, the effect of die ratio, workpiece material, die geometry and friction will be examined by parameter study. The results will also be cross-checked by experimental results that are available in the literature.

The thesis can be divided into eight chapters. In the first chapter, general information about the study will be given. The next chapter will be the literature survey which will include the historical information about the process, the friction models in metal forming and material information. Chapter 3 will consist of information about the models that are proposed by the scientists; their evaluation, limits, advantages and drawbacks. Chapter 4 will be dedicated to Finite Element Method and its theoretical background. The model that is used for the simulations will be mentioned and the parameters will be examined. In chapter 5, the assessment of analytical equations will be done. Chapter 6 will be dedicated to the improvement of the analytical equations. Finally, conclusion, discussions and further recommendations will be the content of the last two chapters.

## CHAPTER 2

### LITERATURE SURVEY

#### 2.1 Introduction

In this chapter some concepts about metal forming will be discussed. In the first part, the analysis methods will be discussed. Later, friction models in metal forming are explained.

#### 2.2 Methods of Analysis in Metal Forming

As seen in Figure 2.1, there are three methods that are utilized to calculate or predict the forming force in metal forming (Tekkaya, 2001(b)):

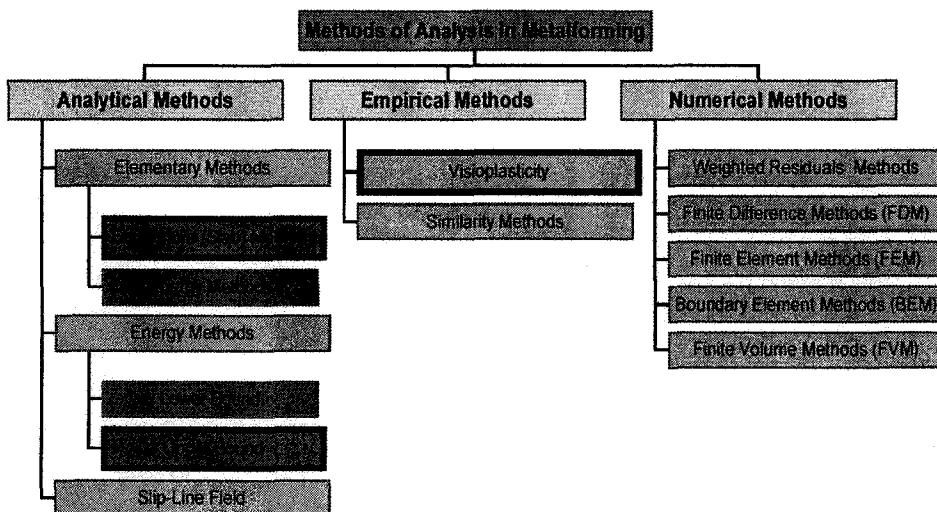


Figure 2.1 Methods of Analysis in Metal Forming

### **Analytical Methods:**

- Elementary Methods ( Slab Methods, Energy Methods)
- Energy Methods (Upper Bound, Lower Bound)
- Slip Line Field

### **Empirical Methods:**

- Viscoplasticity
- Similarity Methods

### **Numerical Methods:**

- Weighted Residuals Methods
- Finite Difference Methods
- Finite Element Methods
- Boundary Element Methods
- Finite Volume Methods

## **2.2.1 Analytical Methods**

### **2.2.1.1 Elementary Methods**

Slab method which is also named as the free body-equilibrium approach, requires a force balance on a strip of metal of differential thickness. This formulation ends up with a differential equation in one direction. The boundary conditions are utilized to reach a solution under the following assumptions:

1. The tool is symmetric
2. Coulomb or shear type friction exists
3. Flow curves are given as a function of strain, strain rate and temperature.
4. The weight and inertial forces are neglected.

5. Plain sections remain plain during the deformation
6. The effect of friction does not effect the principal directions

### **2.2.1.2 Energy Methods**

#### **Upper-Bound Analysis (Kinematically Admissible Solution)**

The upper-bound approach can be stated as follows: For any kinematically admissible velocity field the power term is always larger than the actual one, so the forming forces are always larger than the actual ones. A kinematically admissible velocity field is one that ensures volume constancy and satisfies all kinematic boundary conditions. The internal flow field which is assumed should be in consistency with the shape change (Tekkaya 2001(b)).

#### **Lower-Bound Analysis (Statically Admissible Solution)**

For any statically admissible stress field the power term is always lower than the actual one, so that the forming forces computed are always smaller than the actual ones. A statically admissible stress field is one which fulfills the equilibrium equations and all force boundary conditions (Tekkaya 2001(b)).

### **2.2.2 Empirical Methods**

#### **Visioplasticity**

The determination of the velocity field in metal forming processes is necessary for the prediction of the total power required. The grid that will be used to observe the velocity field after deformation will be produced on a symmetry plane. The grid



can be formed by mechanical, photomechanical and electrochemical means. The workpiece is deformed in one step and the location of the nodes is compared with the initial locations to determine the displacements. The velocities are obtained from the displacements. The knowledge of velocities makes the determination of the strain

rates possible. The stresses and strains are computed by using the strain rates. The calculation of the stresses and strain with viscoplasticity requires some assumption like all other analysis methods. In viscoplasticity the plane sections of the specimen is assumed to remain plane after the deformation. Also the deformation is assumed not to be affected by the grids (Lange, 1985).

**Applications:**

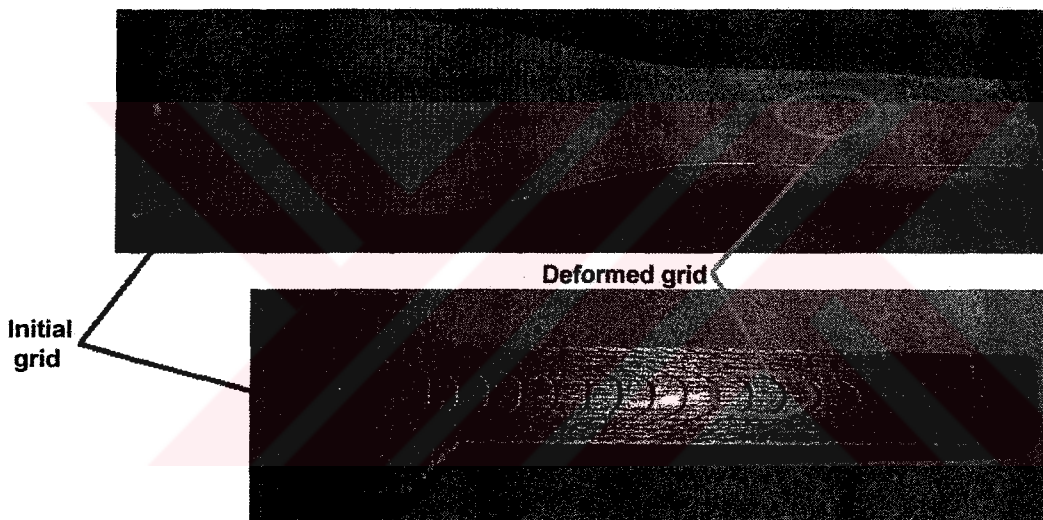


**Figure 2.2** Visioplasticity (Tekkaya, 2000(b))

**2.2.3 Numerical Methods**

**Finite-Element Method**

This method has been used for elastic problems. The utilization of computer for the calculations improved the efficiency of the method in recent years. The basis of the

method is to construct the geometry by using elements that have finite dimensions. The elements are combined at the nodes. The elements are assumed to have uniform stress. The overall behavior of the structure depends on the combined effect of all elements. The accuracy depends highly on the parameters such as element size, type of problem, convergence ratio.

The success of this method has invoked the usage of FEM in plastic deformations. The strain was defined by two components, elastic and plastic. Whereas in large deformations which is the case in most metal forming processes the elastic strain are so small that they can easily be neglected, therefore rigid-plastic model can be employed. The elastic strains are required to be included in the calculations if the forming defects are necessary to be predicted. The rigid –plastic model utilizes a modified upper-bound theorem. The incompressibility restriction has been removed by means of Lagrangian parameter.

### 2.3 Forming Force Formulations Available in the Literature

One of the early studies of force computation for backward can extrusion was done by Sieber (1952). According to Sieber, the fundamental laws of cold plastic deformation are volume constancy and degree of dimensional change in the three principal directions. Sieber defined the term degree of deformation as:

$$\varepsilon = \ln \left( \frac{A_0}{A_1} \right) \quad (2.1)$$

In his work Sieber also pointed out the dependency of forming force on material properties. The flow stress is defined empirically as:

$$\sigma_f = f(\varepsilon) = \sqrt[3]{3P \ln \frac{x_1}{x_0} + \sigma_{f0}} \quad (2.2)$$

where  $P$  is a constant for the material obtained by experiments,  $\sigma_{f0}$  is the elastic

limit,  $x_0$  is the initial length and  $x_1$  is the final length.

The flow stress definition by Sieber is applicable to all cold forming applications. The integration of this flow stress formulation with respect to geometry results in  $k_{fm}$ .

Sieber showed that the total force for backward can extrusion is:

$$P_{\max} = A_0 k_{fm} \left( \ln \left( \frac{A_0}{A_1} \right) + 0.6 \right) \times \left( 1.25 + \frac{\pi (d_0 + d_i) h \mu}{A_0} \right) \quad (2.3)$$

Sachs (1951) has proposed a simple equation for the extrusion pressure. His formula is based on the dimensional change in the part and the compressive resistance of the metal.

$$P = Ak \ln \left( \frac{A}{a} \right) \quad (2.4)$$

where  $A$  is the cross-sectional area of the die,  $a$  is the cross-sectional area of the shell and  $k$  is a constant for the metal.

Dipper (1949) has done his Ph.D. Thesis on backward can extrusion and performed an elementary solution for force calculation.

$$\sigma_{z,m} = \sigma_{r,m} - \sigma_{f1} = -C\bar{\epsilon}_1^n \left( 1 + \frac{2}{3} \mu_1 \frac{r_i}{b} \right) - C\bar{\epsilon}_2^n \left( 1 + \mu \frac{b}{s} \right) \quad (2.5)$$

Dipper assumed backward can extrusion to be double upsetting process and defined a strain values for each zone

$$\text{Zone I} \rightarrow \bar{\epsilon}_1 = \ln\left(\frac{b_0}{b}\right) \quad (2.6)$$

$$\text{Zone II} \rightarrow \bar{\epsilon}_{total} = \bar{\epsilon}_1 + \bar{\epsilon}_2 = \bar{\epsilon}_1 \left(1 + \frac{r_i}{4s}\right) \quad (2.7)$$

His formulation is explained in more detail in Chapter 3.

The forming load formulation by James-Kottcamp (1965) is based on average plastic strain  $\bar{\epsilon}_a$  determined by model test is as follows:

$$P = A_0 \sigma_{f0} \left(\frac{1 + F_n}{2.4}\right) \bar{\epsilon}_a \quad (2.8)$$

$$\bar{\epsilon}_a = 2.36 \ln R + 0.28 \quad (2.9)$$

$$F_n = \left(\frac{e \bar{\epsilon}_a}{n}\right) \quad (2.10)$$

where  $e$  is taken as 2.71828

Avitzur (1964, 1972, 1979, and 1983) has done various studies on extrusion with upper bound method. He assumed backward can extrusion to be a two stage process and developed different velocity field models for both of the stages.

Avitzur (1979) has calculated the total forming power for the second (late) stage by using a two-zone velocity field. The non-dimensional total power is:

$$p_T = \frac{-2}{1-(r_0/r_i)^2} \ln(r_0/r_i) + \frac{1}{\sqrt{3}} \left\{ \frac{1}{3} \frac{(r_0/r_i)^3 + 1}{b/r_i} \left( 1 + \frac{4(r_0/r_i)(b/r_i)^2}{[(r_0/r_i)^2 - 1]^2} \right) \right. \\ \left. + m \left( \frac{1}{3} \frac{(r_0/r_i)^2 + 1}{b/r_i} + \frac{2(r_i/r_0)}{1-(r_i/r_0)^2} \left( \frac{b_0}{r_i} + \frac{r_0}{r_i} \frac{h}{r_i} \right) \right) \right\} \quad (2.11)$$

where  $r_i$ ,  $r_0$ ,  $b$ ,  $b_0$ ,  $h$  are all process dimensions later explained in Chapter 3.

Avitzur (1972) also formulated the forming force for initial (early) stage of the process by using a spherical velocity field. The non-dimensional total power is:

$$p_T = \frac{2}{\sqrt{3}} \frac{1}{1-(r_i/r_0)^2} \left\{ \sqrt{3} \ln(r_0/r_i) + \frac{\alpha}{\sin^2 \alpha} - \cot \alpha \right. \\ \left. + (\cot \alpha) \ln(r_0/r_i) + m \left[ \frac{h}{r_i} + \frac{r_i}{r_0} \left[ \frac{b_0}{r_i} + \left( \frac{r_0}{r_i} - 1 \right) \cot \alpha \right] \right] \right\} \quad (2.12)$$

where angle  $\alpha$  defines the spherical velocity field.

Another formulation by Schoffmann (Altan, 1970) is for steel as:

$$P = A_0 K_c \sigma_u \ln \left( \frac{A_0}{A_1} \right) \quad (2.13)$$

where  $K_c$  is taken in range 2.5-3.0

The force for backward extrusion is also examined by P.E.R.A (Altan, 2000) with 0.1-0.3% C steel is:

$$P = A_0 \sigma_{f0} \left( 3.45 \ln \left( \frac{A_0}{A_1} \right) + 1.15 \right) \quad (2.14)$$

Hoogenboom (2002) had also formulated the total force for the initial (early) stage of the process by modifying the velocity field and defining a free parameter  $\gamma$  for optimization:

$$P_{i(early)} = 1 + \frac{2}{\sqrt{3}} + \frac{1}{\sqrt{3}} \frac{1}{\gamma} + \frac{m+1}{2\sqrt{3}} \gamma + \frac{m+1}{3\sqrt{3}} \frac{1}{\gamma} \frac{r_i}{s} \quad (2.16)$$

The optimum value for  $\gamma$  is found as:

$$\gamma = \sqrt{\frac{2}{m+1} + \frac{2}{3} \frac{r_i}{s}} \quad (2.17)$$

## 2.4 Friction Models in Metal Forming

Friction is resistance to motion, which occurs when two bodies slide over each other. One of the most critical considerations in the metal forming processes is friction which is due to tool and workpiece contact. The friction in metal forming can be due to velocity differences, or can develop as a result of the nature of the deformation process. The energy that is required to overcome the friction in a metal forming process can be more than 50 % of the total energy input. The final properties of the product such as the surface finish and the dimensional precision are strongly dependent on the friction. The production rate, tool design, tool wear and the process optimization depend on the ability to determine and control the process friction. The stress which is formed by friction can be named as  $\tau_f$  which is the average stress at the interface. As soon as this value reaches to the shear flow stress of the material, deformation of the workpiece becomes favorable and the motion at the interface starts. This is called sticking friction.

The friction under metal forming conditions is very different from any other application. In many cases, friction is present between two or more machine parts that have similar mechanical properties and stress and strain values are in the elastic limits. Also the processes take place at low temperatures and with wear-in cycles that produce surface compatibility. On the other hand the metal forming processes have totally different characteristics. The processes involve severe deformation of a soft workpiece material subjected to high forces by hard, nondeforming tool. The workpiece material deforms undergoing plastic flow with a single pass of the tool. The temperature of both the workpiece and the tool tend to increase to at least 300°C for the case of cold forming even more for warm and hot forming processes.

There are two friction models that are used for analysis in metal forming. The first one is Coulomb friction model, and the other one is Shear Model. In a process the maximum friction stress is assumed to be equal to  $k$ , where  $k$  is

$$k = \frac{Y}{2} \quad (\text{Tresca}) \text{ or } k = \frac{Y}{\sqrt{3}} \quad (\text{von Mises}) \quad (2.18)$$

Coulomb's definition states that the coefficient of friction is the ratio between frictional shear stress and the normal stress at the die/workpiece interface.

$$\mu = \frac{\tau_{friction}}{\sigma_n} \quad (2.19)$$

The friction coefficient increases till it reaches a constant value, where the maximum frictional shear stress is obtained. The maximum shear stress is defined in the Eq. (2.18). As a result of this definition the coefficient of friction has an upper limit:

$$0 \leq \mu \leq 0.5 \quad (\text{Tresca}) \quad (2.20a)$$

$$0 \leq m \leq 0.577 \quad (\text{von Mises}) \quad (2.20b)$$

The relationship between frictional shear stress and the normal stress at the interface can be seen from the Figure 2.3

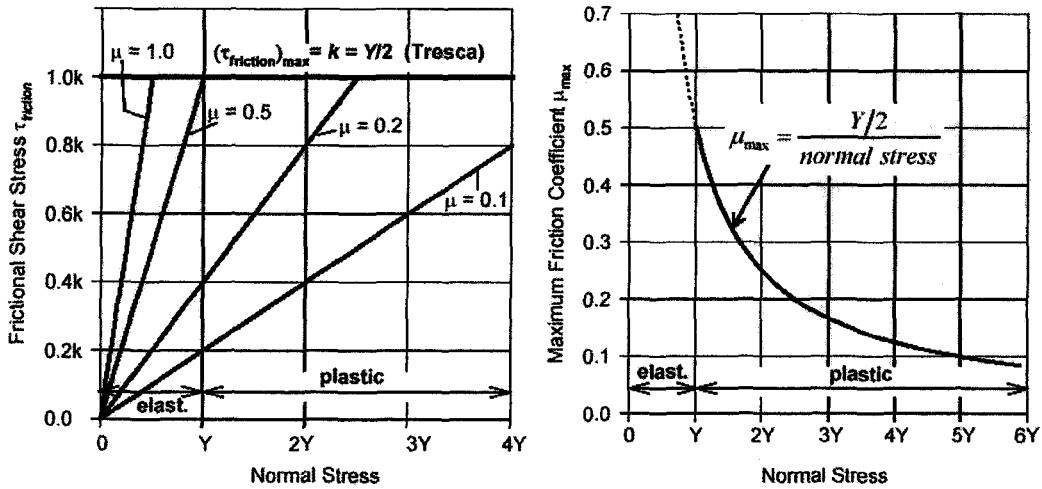


**Figure 2.3** Relationships of Normal and Shear Stress for Coulomb Model

Since the coefficient of friction has a maximum value, there is another type of definition necessary for the cases when the frictional shear stress exceeds the flow stress. This is valid for most of the bulk forming processes where  $\mu\sigma_n \gg k$ . The sliding friction definition becomes invalid since no sliding exists between the tool and the workpiece. The definition of frictional shear factor is necessary for such situations.

$$\tau_{friction} = mk \quad (2.21)$$

This definition links the known material property to the frictional shear stress, which simplifies the calculations. This factor is used in upper-bound solutions and numerical techniques.



The relationship between the shear friction and coulomb friction is always a matter of argument. In the ideal case the two definitions are assumed to be equal:

$$\mu\sigma_n = mk \quad (2.22)$$

When the definition by Tresca for  $k$  is inserted to the equality:

$$\mu\sigma_n = m\frac{Y}{2} \quad (2.23)$$

and the normal stress  $\sigma_n$  is assumed to be equal to flow stress  $\sigma_f$

$$\mu Y = m\frac{Y}{2} \quad (2.24)$$

Then the result will be,

$$m = 2\mu \quad (2.25)$$

This is only valid for the ideal case, in practice the normal stress is much higher than the flow stress, if a factor  $S$  is assigned to the relationship between the flow and normal stress,

$$\sigma_n = SY \quad (2.26)$$

If Eq. (2.26) is inserted in to Eq. (2.22), we will obtain

$$m = 2S\mu \quad (2.27)$$

The equation above states that the friction factor varies with respect to process and the severity of the deformation, since it depends on the normal stress at the specified location

Niels Bay (1983) friction model is a new friction model different than both coulomb friction model and shear friction model but a combination of these models. He claims that at low normal pressure, the friction stress and normal pressure are proportional and coulomb's friction model is applicable. However, for high normal pressure, the friction stress is constant and shear friction model should be used. According to these statements, he proposes a new friction stress versus normal pressure diagram which is a combination of both friction models, Figure 2.4. The normal pressure and the friction stress are normalized by dividing yield stress  $\sigma_0$  and the yield stress in pure shear,  $k$  respectively.

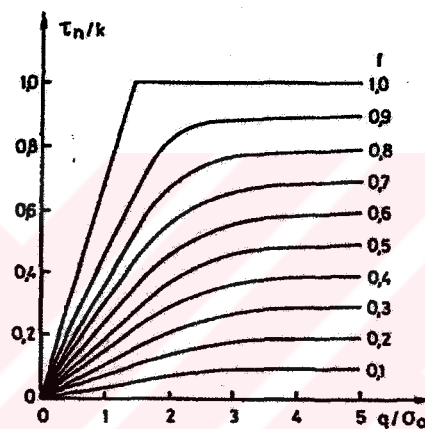


**Figure 2.4** Friction stress as a function normal pressure and friction factor

## 2.5 Conclusion

The analytical equations available in the literature are based on various assumptions. The performance and the range of application for these formulations have never been deeply examined. On the other hand finite element analysis is a very powerful tool for estimating the forming force for metal forming processes. The need for highly skilled staff and need for expensive hardware and software make finite element impractical. This study is done to overcome the disadvantages of both ways and to

come up with results that clarifies the doubts about the performance of commonly used formulations with the help of finite element analysis.



## **CHAPTER 3**

### **ASSESSED ANALYTICAL FORMULATIONS**

#### **3.1 Introduction**

In this chapter the previous literature for analytical equations related to the current study will be discussed. The analytical solutions that are commonly used for the force calculations are examined. Firstly, the elementary solution by Dipper (1949), then later in the chapter the upper-bound solutions that were done by different scientists, Avitzur (1964, 1972, 1979, 1983), Dipper (1949), Hoogenboom (2002) with various assumptions and velocity fields are discussed.

#### **3.2 Elementary Methods**

##### **3.2.1 Dipper's Solution**

Dipper (1949) considered the backward can extrusion as a double upsetting process. In the solution workpiece is divided into three zones as it can be seen in the Figure 3.1. Zone I which lies under the punch is assumed to be upsetted axially between the punch and the die bottom, and the region that is between zone I and the die is assumed to be upsetted radially. Finally, third zone is assumed to go through rigid body motion. Another assumption is that the cans that are extruded have more than 50% area reduction.

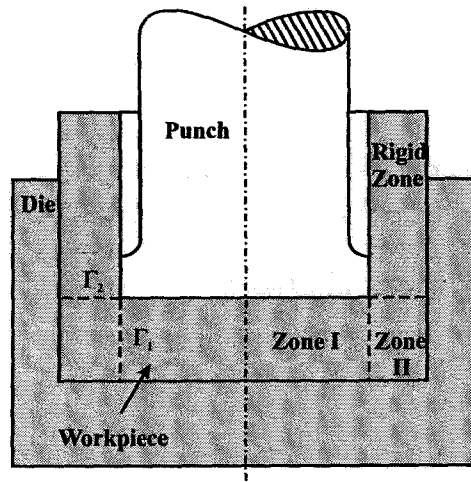


Figure 3.1 Dipper's Velocity Field

Dipper suggested that the friction coefficient between zone I and zone II is 0.5 according to Tresca, due to the fact that the material experiences shear on  $\Gamma_1$ . The friction on the die wall is  $\mu_1$ . The coefficient of friction can be calculated as follows:

$$\mu = \frac{1}{2}(\mu_1 + 0.5) \quad (3.1)$$

The solution was developed by considering force equilibrium in both of the deforming zones (Figure 3.2).

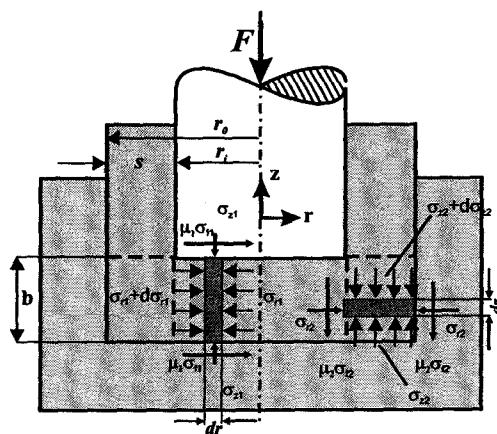


Figure 3.2 Double Upsetting Process

For zone II, the frictional forces are calculated by taking an average cylinder radius for the sake of simplicity.

$$r_{av} = \frac{r_i + r_0}{2} = r_i + \frac{s}{2} \quad (3.2)$$

The force equilibrium is as follows

$$[-\sigma_{z,2} + (\sigma_{z,2} + d\sigma_{z,2})] \pi (r_0^2 - r_i^2) = 2\mu\sigma_{f2} (r_i + s/2) 2\pi dz \quad (3.3)$$

$$s d\sigma_{z,2} = 2\mu\sigma_{f2} dz \quad (3.4)$$

Integrating the terms with the boundary condition  $\sigma_{z,2} = 0$  at  $z = b$  will result

$$\sigma_{z,2} = \frac{2\mu\sigma_{f2}}{s} (b - z) \quad (3.5)$$

The average normal stress can be calculated for zone II with the average area  $A_2$

$$A_2 = 2r_{av}\pi b = 2\left(r_i + \frac{s}{2}\right)\pi b \quad (3.6)$$

The mean stress in  $z$ -direction for zone II can be found as

$$\sigma_{z,2,m} = \frac{\int_0^b \sigma_{z,2} dA}{A_2} = \frac{\int_0^b \frac{2\mu\sigma_{f2}}{s} (b - z) 2\left(r_i + \frac{s}{2}\right) \pi dz}{2\left(r_i + \frac{s}{2}\right)\pi b} \quad (3.7)$$

$$\sigma_{z,2,m} = \frac{\frac{4\mu\sigma_{f2}}{s} \left(r_i + \frac{s}{2}\right) \pi \int_0^b (b-z) dz}{2 \left(r_i + \frac{s}{2}\right) \pi b} = \frac{2\mu\sigma_{f2}}{sb} \int_0^b (b-z) dz \quad (3.8)$$

$$\sigma_{z,2,m} = \frac{\mu\sigma_{f2}}{sb} \left[ (2bz - z^2) \right]_0^b = \frac{\mu\sigma_{f2}}{sb} (2b^2 - b^2) = \mu\sigma_{f2} \frac{b}{s} \quad (3.9)$$

According to the Tresca flow condition

$$\sigma_{r,2,m} = \sigma_{z,2,m} - \sigma_{f2} = -\sigma_{f2} \left(1 + \mu \frac{b}{s}\right) \quad (3.10)$$

For Zone I, which goes through axial upsetting, the force equilibrium equation is

$$\left[ -\sigma_{r,1} + (\sigma_{r,1} + d\sigma_{r,1}) \right] \pi r b = 2\mu_1 \sigma_{f1} \pi r dz \quad (3.11)$$

$$d\sigma_{r,1} b = 2\mu_1 \sigma_{f1} dr \quad (3.12)$$

Integrating the terms with the boundary condition  $\sigma_{r,1} = \sigma_{r,2,m}$  at  $r = r_i$ , the result will be

$$\sigma_{r,1} = \frac{\mu_1 \sigma_{f1}}{b} (r_i - r) + \sigma_{r,2,m} \quad (3.13)$$

The average radial stress over the area  $\pi r_i^2$  is given by

$$\sigma_{r,1,m} = -\frac{1}{3} \mu_1 \sigma_{f1} \frac{2r_i}{b} + \sigma_{r,2,m} \quad (3.14)$$

When  $\sigma_{r,2,m}$  is substituted from the Eq. (3.9), the average radial stress will be

$$\sigma_{r,m} = \sigma_{r,1,m} + \sigma_{r,2,m} = -\frac{2}{3}\mu_1\sigma_{f1}\frac{r_i}{b} - \sigma_{f2}\left(1 + \mu\frac{b}{s}\right) \quad (3.15)$$

Applying the Tresca flow condition, the axial stress on the punch is

$$\sigma_{z,m} = \sigma_{r,m} - \sigma_{f1} = -\sigma_{f1}\left(1 + \frac{2}{3}\mu_1\frac{r_i}{b}\right) - \sigma_{f2}\left(1 + \mu\frac{b}{s}\right) \quad (3.16)$$

Where the strains in zone I and zone II are defined as:

$$\text{Zone I} \rightarrow \bar{\epsilon}_1 = \ln\left(\frac{b_0}{b}\right) \quad (3.17)$$

$$\text{Zone II} \rightarrow \bar{\epsilon}_{total} = \bar{\epsilon}_1 + \bar{\epsilon}_2 = \bar{\epsilon}_1\left(1 + \frac{r_i}{4s}\right) \quad (3.18)$$

The flow stress is defined by Eq. (3.19) for a flow rule of Ludwik's type

$$\sigma_f = C\bar{\epsilon}^n \quad (3.19)$$

where  $C$  and  $n$  are material constants.

Inserting the strain values in Eq. (3.17) and Eq. (3.18), the flow stress for each zone can be calculated.

$$\sigma_{f1} = C\bar{\epsilon}_1^n \quad (3.20)$$



$$\sigma_{f2} = C\bar{\epsilon}_2^n \quad (3.21)$$

Then the axial stress on punch will become

$$\sigma_{z,m} = \sigma_{r,m} - \sigma_{f1} = -C\bar{\epsilon}_1^n \left(1 + \frac{2}{3}\mu_1 \frac{r_i}{b}\right) - C\bar{\epsilon}_2^n \left(1 + \mu \frac{b}{s}\right) \quad (3.22)$$

### 3.3 Upper Bound Solution

The total power calculated by the upper bound predicts a forming power which is more than the real forming power. The result is adequate to overcome the friction, shear losses and power of internal deformation. In some cases it may be necessary to calculate the power losses due to external tractions or inertia effects.

The formulation of the upper bound was presented by Prager and Hodge (1951). They have stated that: "Among all kinematically admissible strain rate fields, the actual one minimizes the expression

$$J^* = k\sqrt{2} \int_V \sqrt{\dot{\epsilon}_{ij}^* \dot{\epsilon}_{ij}^*} dV - \int_{S_T} T_i v_i^* dS \quad (3.23)$$

where

$J^*$  is the upper bound on power

$k$  is the yield stress in shear

$V$  is the volume of the deforming zone

$\dot{\epsilon}_{ij}$  is the strain rate

$T_i$  is the external tractions

$v_i$  are surface discontinuity velocities

$S_T$  is the surface over which the transactions are exerted

For an upper bound solution to exist, a kinematically admissible velocity field has to be assigned. A kinematically admissible velocity field is one that ensures volume

constancy and satisfies all kinematic boundary conditions. The velocity field is used to calculate the strain rate field. The selection of the velocity field is critical since the appropriate velocity field will decrease the power calculated and bring it closer to actual values.

The material obeys to von Mises yield criterion with the definition:

$$k = \frac{\sigma_{f0}}{\sqrt{3}} \quad (3.24)$$

where  $\sigma_{f0}$  is the initial flow stress of the material, which is constant.

As a result of inserting Eq. (3.24) to Eq. (3.23), the upper bound equation becomes

$$J^* = \frac{2\sigma_{f0}}{\sqrt{3}} \int_V \sqrt{\frac{1}{2} \dot{\epsilon}_{ij}^* \dot{\epsilon}_{ij}^*} dV - \int_{S_T} T_i v_i^* dS \quad (3.25)$$

The upper bound equation was modified by Drucker (1951), by adding the friction term which is present between the workpiece and the tool and shear term which is present with in the deforming material. This was done using the concept of surfaces of velocity discontinuity, which are defined by the velocity field. As a result the upper bound equation becomes:

$$J^* = \frac{2\sigma_{f0}}{\sqrt{3}} \int_V \sqrt{\frac{1}{2} \dot{\epsilon}_{ij}^* \dot{\epsilon}_{ij}^*} dV + \int_{S_T} \tau |\Delta v| dS - \int_{S_T} T_i v_i^* dS \quad (3.26)$$

where

$\tau$  is the shear stress

$S_T$  is the surface of velocity discontinuity

$\Delta v$  is the tangential velocity acting on the discontinuity surface

The upper bound solution for backward can extrusion is divided into two stages. This is due to the presence of the so-called dead-zone at the early stage of the process. This zone diminishes later in the deformation, which directly effects the definition of the velocity field for the model. The proposed solutions will be examined separately for each situation in the coming parts of this chapter.

### 3.3.1 Late Stage

The late stage of backward can extrusion is characterized with the deformation of the whole material that lies under the punch. The upper-bound formulation of the late stage can be formulated by two different velocity fields which are shown in Figure 3.3.

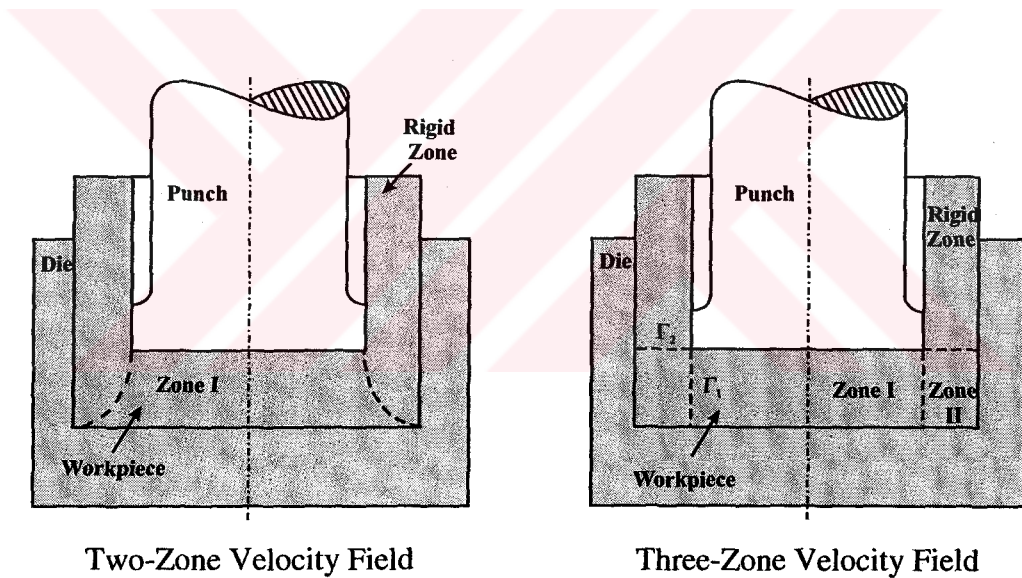


**Figure 3.3** Velocity Field for the Late Stage

#### 3.3.1.1 Two-Zone Velocity Field

Avitzur (1979) has used the two-zone velocity field model for the upper-bound solution for the end of stroke as it can be seen in the Figure 3.4. In this model, there

is one surface velocity discontinuity. Material under the punch is plastically deformed like a thin-disk, whereas the material in the annular gap goes through rigid-body motion.

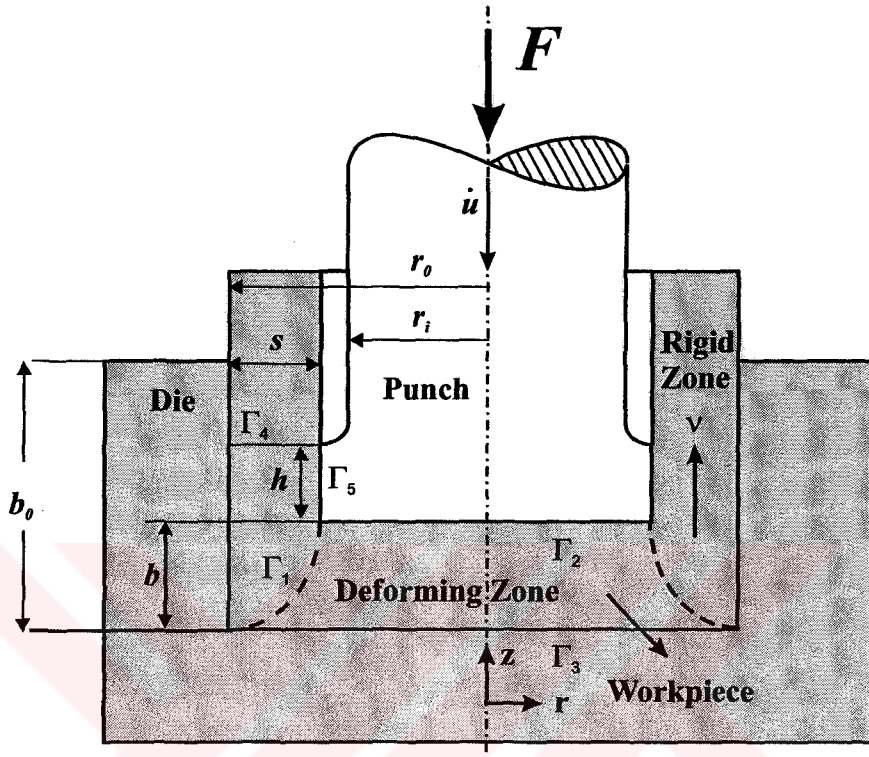


**Figure 3.4** Two-Zone Velocity Field

The formulation of velocities and strain rates for upsetting, which is used in this section is given in Appendix A. The velocities for the deformation zone are:

$$\begin{aligned}
 \dot{u}_\theta &= 0 && \text{velocity in } \theta \text{ direction} \\
 \dot{u}_z &= \frac{z}{b} \dot{u} && \text{velocity in } z \text{ direction} \\
 \dot{u}_r &= -\frac{1}{2} \frac{r}{b} \dot{u} && \text{velocity in } r \text{ direction}
 \end{aligned} \tag{3.27}$$

where  $\dot{u}$  is the punch velocity.

The velocity of the rigid zone that goes through rigid body motion can be calculated from volume constancy of the material:

$$\begin{aligned}
 v\pi(r_0^2 - r_i^2) &= -\dot{u}\pi r_i^2 \\
 v &= \frac{-\dot{u}r_i^2}{(r_0^2 - r_i^2)} \\
 v &= \frac{\dot{u}}{1 - (r_0/r_i)^2} \tag{3.28}
 \end{aligned}$$

Where  $v$  is the exit velocity

The discontinuity surface  $\Gamma_1$  has a specific topography. The radial and axial velocities can be seen in Figure 3.5.

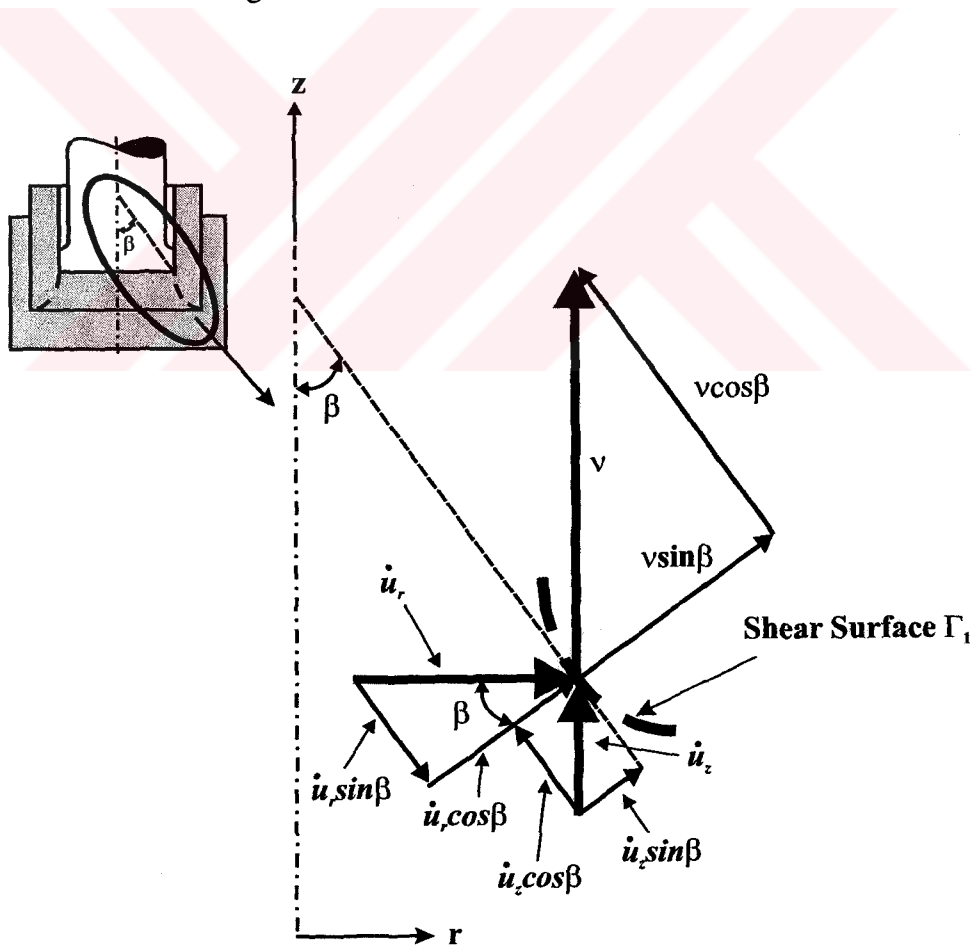


Figure 3.5 Velocity Components

The topography of shear surface  $\Gamma_1$  is calculated by equating the normal components of the velocity fields in zone I and II:

$$\dot{u}_r \cos \beta + \dot{u}_z \sin \beta = v \sin \beta \quad (3.29)$$

$$\dot{u}_r \cos \beta = (v - \dot{u}_z) \sin \beta \quad (3.30)$$

When we divide both sides by  $\sin \beta$  and then by  $\dot{u}_r$ , we will obtain

$$\cot \beta = \frac{v - \dot{u}_z}{\dot{u}_r} = -\frac{dz}{dr} \quad (3.31)$$

When the values of  $\dot{u}_z$  and  $\dot{u}_r$  are substituted from Eq. (3.27), Eq. (3.31) becomes

$$2 \frac{b}{\dot{u}} \frac{dr}{r} = \frac{dz}{v - \dot{u}z/b} \quad (3.32)$$

The solution of Eq. (3.32) will be

$$2 \frac{b}{\dot{u}} \ln r + \frac{b}{\dot{u}} \ln C = -\frac{b}{\dot{u}} \ln \left| v - z \frac{\dot{u}}{b} \right| \quad (3.33)$$

where  $C$  is the integration constant.

Using the rules for natural logarithm

$$\frac{b}{\dot{u}} \ln(Cr^2) + \frac{b}{\dot{u}} \ln \left| v - z \frac{\dot{u}}{b} \right| = 0 \quad (3.34)$$

$$\ln \left[ (Cr^2) \left( v - z \frac{\dot{u}}{b} \right) \right] = 0 \quad (3.35)$$

$$Cr^2 \left( \nu - z \frac{\dot{u}}{b} \right) = 1 \quad (3.36)$$

Boundary condition for Eq. (3.36) is

$$r \Big|_{z=0} = r_0 \quad (3.37)$$

As a result, the constant  $C$  will become

$$C = \frac{1}{\nu r_0^2} \quad (3.38)$$

When the value of  $C$  is inserted to Eq. (3.36)

$$\frac{1}{\nu} \left( \frac{r}{r_0} \right)^2 \left( \nu - z \frac{\dot{u}}{b} \right) = 1 \quad (3.39)$$

$$\left( \frac{r}{r_0} \right)^2 \left( 1 - \frac{z \dot{u}}{\nu b} \right) = 1$$

When we leave  $(r/r_0)^2$  ratio on one side of the equality

$$\left( \frac{r}{r_0} \right)^2 = \frac{1}{\left( 1 - \frac{z \dot{u}}{\nu b} \right)} \quad (3.40)$$

Taking square root of both sides

$$\frac{r}{r_0} = \frac{1}{\sqrt{\left( 1 - (z/\nu)(\dot{u}/b) \right)}} \quad (3.41)$$

When we substitute the value of  $v$  from Eq. (3.28), we will obtain the relationship between  $z$  and  $r$ ;

$$\frac{r}{r_0} = \frac{1}{\sqrt{1 - [1 - (r_0/r_i)^2](z/b)}} \quad (3.42)$$

For the calculation of the power for zone I, the strain rates are necessary:

$$\dot{\epsilon}_{rr} = \dot{\epsilon}_{\theta\theta} = -\frac{1}{2}\dot{\epsilon}_{zz} = -\frac{1}{2}\frac{\dot{u}}{b} \quad (3.43)$$

$$\dot{\epsilon}_{r\theta} = \dot{\epsilon}_{\theta z} = \dot{\epsilon}_{rz} = 0 \quad (3.44)$$

The deformation power for zone I, referring to the upper bound formulation, is:

$$\begin{aligned} \dot{W}_i &= \frac{2\sigma_{f0}}{\sqrt{3}} \int_V \sqrt{\frac{1}{2}\dot{\epsilon}_{ij}^*\dot{\epsilon}_{ij}^*} dV = 2\sigma_{f0} \int_V \dot{\epsilon}_{rr} dV \\ \dot{W}_i &= 2\sigma_{f0} \dot{\epsilon}_{rr} \int_V dV = 2\sigma_{f0} \dot{\epsilon}_{rr} V \end{aligned} \quad (3.45)$$

The volume for this portion of the material can be calculated as:

$$V = \pi \int_{z=0}^b r^2 dz \quad (3.46)$$

When we substitute the value for  $r$  from the Eq. (3.42) the integral becomes

$$V = \pi \int_{z=0}^b \frac{r_0^2}{1 - [1 - (r_0/r_i)^2](z/b)} dz \quad (3.47)$$



$$V = -2\pi r_0^2 \frac{b}{1 - (r_0/r_i)^2} \ln(r_0/r_i) \quad (3.48)$$

Inserting the expression for the volume and strain rate into Eq. (3.45), the deformation power for deformation zone becomes

$$\dot{W}_i = \frac{-2}{1 - (r_0/r_i)^2} \sigma_{f0} \pi \dot{u} r_0^2 \ln(r_0/r_i) \quad (3.49)$$

The power for shear losses will be calculated for the surface of discontinuity. The formulation of upper bound for the shear loss is:

$$\dot{W}_{S_{\Gamma 1}} = \int_{\Gamma 1} \tau |\Delta v| dS \quad (3.50)$$

where shear stress is

$$\tau = \frac{\sigma_{f0}}{\sqrt{3}} \quad (3.51)$$

The area of the discontinuity surface

$$dS = 2\pi r \frac{dr}{\sin \beta} \quad (3.52)$$

The surface discontinuity velocity

$$\Delta v = v \cos \beta + \dot{u}_r \sin \beta - \dot{u}_r \cos \beta \quad (3.53)$$

When Eq. (3.51), Eq. (3.52) and Eq. (3.53) are inserted to the Eq. (3.50), the result will be:

$$\dot{W}_{s_{\Gamma_1}} = \frac{2}{\sqrt{3}} \pi \sigma_{f_0} \int_{r_0}^{r_i} (v \cos \beta + \dot{u}_r \sin \beta - \dot{u}_z \cos \beta) dr \quad (3.54)$$

Inserting the value of  $v$  from the Eq. (3.28) and  $\dot{u}_z$  and  $\dot{u}_r$  from Eq. (3.27),

$$\dot{W}_{s_{\Gamma_1}} = \frac{2}{\sqrt{3}} \pi \sigma_{f_0} \dot{u} \int_{r_i}^{r_0} \left[ \frac{\cot \beta}{1 - (r_0/r_i)^2} - \frac{1}{2} \frac{r}{b} - \frac{z}{b} \cot \beta \right] r dr \quad (3.55)$$

Since  $\cot \beta = -\frac{dz}{dr}$  (3.56)

The shear power for  $\Gamma_1$ -plane will be

$$\dot{W}_{s_{\Gamma_1}} = \frac{2}{\sqrt{3}} \pi \sigma_{f_0} \dot{u} \left[ -\frac{1}{1 - (r_0/r_i)^2} \int_{r_i}^{r_0} r dz - \frac{1}{2} \frac{1}{b} \int_{r_i}^{r_0} r^2 dr + \frac{1}{b} \int_{r_i}^{r_0} z r dz \right] \quad (3.57)$$

The relationship between  $r$  and  $z$  is given by Eq. (3.42) which will result in

$$\dot{W}_{s_{\Gamma_1}} = \frac{2}{\sqrt{3}} \pi \sigma_{f_0} \dot{u} \left\{ \frac{r_0}{1 - (r_0/r_i)^2} \int_{z=b}^0 \frac{dz}{\sqrt{1 - [1 - (r_0/r_i)^2] (z/b)}} \right. \\ \left. - \frac{1}{6} \frac{1}{b} (r_0^3 - r_i^3) + \frac{r_0}{b} \int_{z=b}^0 \frac{z dz}{\sqrt{1 - [1 - (r_0/r_i)^2] (z/b)}} \right\} \quad (3.58)$$

When simplified

$$\dot{W}_{s_{\Gamma_1}} = \frac{2}{\sqrt{3}} \pi \sigma_{f0} \dot{u} \left\{ -\frac{r_0}{1-(r_0/r_i)^2} \frac{2b}{1-(r_0/r_i)^2} ((r_0/r_i)-1) \right. \\ \left. - \frac{1}{6} \frac{r_0^3 - r_i^3}{b} - \frac{r_0}{b} \frac{2b^2}{[1-(r_0/r_i)^2]^2} \left( \frac{[(r_0/r_i)^3 - 1]}{3} - ((r_0/r_i)-1) \right) \right\} \quad (3.59)$$

When the Eq. (3.59) is further simplified the shear losses on  $\Gamma_1$  will become

$$\dot{W}_{s_{\Gamma_1}} = -\frac{2}{\sqrt{3}} \pi \sigma_{f0} \dot{u} \left[ (r_0/r_i)^3 - 1 \right] \left\{ \frac{1}{2} \frac{r_i^3}{b} - \frac{2br_0}{[(r_0/r_i)^2 - 1]^2} \right\} \quad (3.60)$$

The friction power for the surfaces  $\Gamma_2$ ,  $\Gamma_3$ ,  $\Gamma_4$  and  $\Gamma_5$  can be calculated as:

$$\tau = m \frac{\sigma_{f0}}{\sqrt{3}} \quad (3.61)$$

where  $m$  is the friction factor and  $\sigma_{f0}$  is the initial flow stress of the material.

For  $\Gamma_2$ ,  $\Gamma_3$ ; the surface discontinuity velocity is:

$$\Delta v = \dot{u}_r = -\frac{1}{2} \frac{\dot{u}}{b} r \quad (3.62)$$

For  $\Gamma_4$  the surface discontinuity velocity is:

$$\Delta v = v \quad (3.63)$$

For  $\Gamma_5$  the surface discontinuity velocity is:

$$\Delta v = v - \dot{u} \quad (3.64)$$

The integrations will provide the friction losses for each surface

For  $\Gamma_2$ ,

$$\dot{W}_{S2} = \int_{\Gamma_2} \tau |\Delta v| ds = -\pi m \frac{\sigma_{f0}}{\sqrt{3}} \frac{\dot{u}}{b} \int_0^{r_i} r^2 dr = -\frac{\pi}{3\sqrt{3}} m \sigma_{f0} \frac{\dot{u}}{b} r_i^3 \quad (3.65)$$

For  $\Gamma_3$ ,

$$\dot{W}_{S3} = \int_{\Gamma_3} \tau |\Delta v| ds = -\pi m \frac{\sigma_{f0}}{\sqrt{3}} \frac{\dot{u}}{b} \int_0^{r_0} r^2 dr = -\frac{\pi}{3\sqrt{3}} m \sigma_{f0} \frac{\dot{u}}{b} r_0^3 \quad (3.66)$$

For  $\Gamma_4$ ,

$$\dot{W}_{S4} = \int_{\Gamma_4} \tau |\Delta v| ds = m \frac{\sigma_{f0}}{\sqrt{3}} \int_0^{b_0} 2\pi r_0 v dz \quad (3.67)$$

$$\dot{W}_{S4} = \frac{2}{\sqrt{3}} \pi m \sigma_{f0} r_0 b_0 v = \frac{2}{\sqrt{3}} \pi m \sigma_{f0} \dot{u} b_0 \frac{r_0}{1 - (r_0/r_i)^2}$$

Where  $b_0$  is the initial billet length.

$$\dot{W}_{S5} = \int_{\Gamma_5} \tau |\Delta v| ds = m \frac{\sigma_{f0}}{\sqrt{3}} \int_0^h 2\pi r_i (v - \dot{u}) dz \quad (3.68)$$

$$\dot{W}_{S5} = \frac{2}{\sqrt{3}} \pi m \sigma_{f0} r_i h (v - \dot{u}) = \frac{2}{\sqrt{3}} \pi m \sigma_{f0} \dot{u} h \frac{(r_0/r_i) r_0}{1 - (r_0/r_i)^2}$$

Where  $h$  is punch land

When we substitute all the power components to Eq. (3.26) the non-dimensionalized total power ( $p_T$ ) will be

$$p_T = \frac{-2}{1-(r_0/r_i)^2} \ln(r_0/r_i) + \frac{1}{\sqrt{3}} \left\{ \frac{1}{3} \frac{(r_0/r_i)^3 + 1}{b/r_i} \left( 1 + \frac{4(r_0/r_i)(b/r_i)^2}{[(r_0/r_i)^2 - 1]^2} \right) \right. \\ \left. + m \left( \frac{1}{3} \frac{(r_0/r_i)^2 + 1}{b/r_i} + \frac{2(r_i/r_0)}{1-(r_i/r_0)^2} \left( \frac{b_0}{r_i} + \frac{r_0}{r_i} \frac{h}{r_i} \right) \right) \right\} \quad (3.69)$$

For thin-tubes ( $s/r_i \ll 1$ ), Eq. (3.69) becomes

$$\frac{p_T}{\sigma_{f0}} = 1 + \frac{1}{\sqrt{3}} \left\{ \frac{s/r_i}{b/r_i} + \frac{b/r_i}{s/r_i} + m \left( \frac{2}{3(b/r_i)} + \frac{b_0/r_i + (r_0/r_i)(h/r_i)}{s/r_i} \right) \right\} \quad (3.70)$$

Where  $\frac{s}{r_i} = \frac{r_0 - r_i}{r_i}$  (3.71)

### 3.3.1.2 Three Zone Velocity Field with Thick-Walled Solution

As stated before for the upper bound solution a velocity field or a set of velocity fields has to be assumed for the deformation process. Due to the nature of the process of backward can extrusion it is not possible to have a single velocity field for the whole system. One of the applicable velocity fields for backward can extrusion is the so-called parallel velocity field as seen in Figure 3.6. This velocity field is proposed by Kudo (1960) for both early and late stages of backward can extrusion.

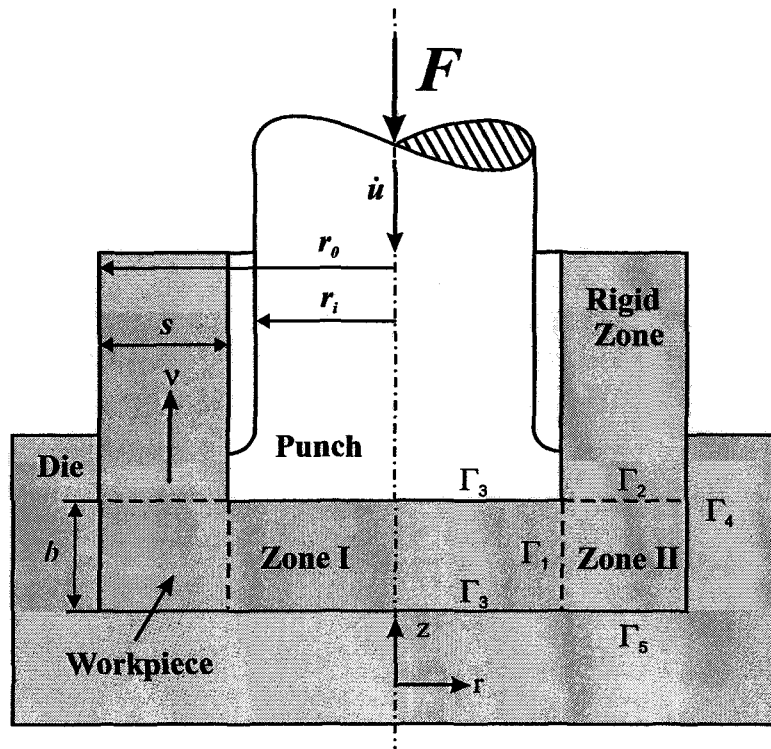


Figure 3.6 Three Zone Velocity Field

The solution for this velocity field has been derived by applying the necessary boundary conditions. In zone I, the upper bound solution for upsetting is used, since this zone experiences the same type of deformation. Therefore, the velocity components are:

$$\dot{u}_{rI} = \frac{\dot{u}}{b} \frac{r}{2} \quad \dot{u}_{zI} = -\frac{\dot{u}}{b} z \quad (3.72)$$

The velocities for zone II can be calculated by the volume constancy in the velocity discontinuity surface  $\Gamma_1$ ,

$$\dot{u}_{zII} \pi \left[ (r_i + s)^2 - (r_i)^2 \right] = \dot{u}_{rI(r=r_i)} 2\pi r_i z \quad (3.73)$$

Inserting the value  $\dot{u}_{rI}$  to the Eq. (3.73);

$$\dot{u}_{zII} = \frac{r_i^2}{s(2r_i + s)} \frac{\dot{u}}{b} z \quad (3.74)$$

The radial velocity in zone II can be found by using the volume constancy

$$\dot{\epsilon}_{rr} + \dot{\epsilon}_{\theta\theta} + \dot{\epsilon}_{zz} = 0 \quad (3.75a)$$

$$\dot{\epsilon}_{rr} = \frac{\partial \dot{u}_{rII}}{\partial r} \quad \dot{\epsilon}_{\theta\theta} = \frac{\dot{u}_{rII}}{r} \quad \dot{\epsilon}_{zz} = \frac{\partial \dot{u}_{zII}}{\partial z} \quad (3.75b)$$

$$\frac{\partial \dot{u}_{rII}}{\partial r} + \frac{1}{r} \dot{u}_{rII} + \dot{\epsilon}_{zz} = 0 \quad (3.75c)$$

The strain rate for z-axis can be calculated as

$$\dot{\epsilon}_{zz} = \frac{\partial \dot{u}_{zII}}{\partial z} = \frac{r_i^2}{s(2r_i + s)} \frac{\dot{u}}{b} \quad (3.76)$$

When we simplify Eq. (3.75c)

$$\frac{1}{r} \frac{\partial (\dot{u}_{rII} r)}{\partial r} = -\dot{\epsilon}_{zz} \quad (3.77)$$

$$\frac{\partial (\dot{u}_{rII} r)}{\partial r} = -r \dot{\epsilon}_{zz} \quad (3.78)$$

When the both sides are integrated

$$\int d(\dot{u}_{rII} r) = - \int (-r) \dot{\epsilon}_{zz} dr \quad (3.79)$$

$$\dot{u}_{rII} r = -\frac{r^2}{2} \dot{\epsilon}_{zz} + C \quad (3.80)$$

Where  $C$  is the integration constant,

$$\dot{u}_{rII} = -\frac{r}{2} \dot{\epsilon}_{zz} + \frac{C}{r} \quad (3.81)$$

The boundary conditions for the radial velocity in zone II are:

$$\dot{u}_{rII}(r=r_0) = 0 \quad (3.82)$$

$$\dot{u}_{rII}(r=r_i) = \dot{u}_{rI}$$

When we insert the boundary conditions into Eq. (3.81) then the constant  $C$  will turn out to be

$$C = \frac{r_i^2 (r_i + s)^2 \dot{u}}{2s(2r_i + s) b} \quad (3.83)$$

When we insert the Eq. (3.76) and Eq. (3.83) to Eq. (3.81) then the result will be

$$\dot{u}_{rII} = -r \left( \frac{r_i^2}{2s(2r_i + s) b} \dot{u} \right) + \frac{1}{r} \left( \frac{r_i^2 (r_i + s)^2 \dot{u}}{2s(2r_i + s) b} \right) \quad (3.84)$$

When we arrange the terms

$$\dot{u}_{rII} = \frac{r_i^2}{2s(2r_i + s) b} \dot{u} \left( -r + \frac{(r_i + s)^2}{r} \right) \quad (3.85)$$



The axial velocity in rigid zone (the upward velocity for the can) can be calculated by continuity at the surface of velocity discontinuity  $\Gamma_2$

$$\dot{u}_{zIII} = \dot{u}_{zII(z=h)} = \frac{r_i^2}{s(2r_i + s)} \dot{u} \quad (3.86)$$

The strain rates and the corresponding strains for the zones can be derived from the velocities for each zone.

Zone I

$$\dot{\epsilon}_r = \dot{\epsilon}_\theta = -\frac{1}{2} \dot{\epsilon}_z = \frac{\dot{u}}{2b} \quad (3.87)$$

$$\dot{\epsilon}_{\theta r} = \dot{\epsilon}_{\theta z} = \dot{\epsilon}_{zr} = 0$$

The total equivalent plastic strain rate for zone I is

$$\dot{\bar{\epsilon}}_I = \sqrt{\frac{2}{3}(\dot{\epsilon}_r^2 + \dot{\epsilon}_\theta^2 + \dot{\epsilon}_z^2) + 2(\dot{\epsilon}_{\theta r}^2 + \dot{\epsilon}_{\theta z}^2 + \dot{\epsilon}_{zr}^2)} = -\frac{\dot{u}}{b} \quad (3.88)$$

Zone II

$$\dot{\epsilon}_r = \frac{\partial \dot{u}_r}{\partial r} = \frac{r_i^2}{2s(2r_i + s)} \frac{\dot{u}}{b} \left( -1 + \frac{(r_i + s)^2}{r^2} \right)$$

$$\dot{\epsilon}_\theta = \frac{\dot{u}_r}{r} = \frac{r_i^2}{2s(2r_i + s)} \frac{\dot{u}}{b} \left( -1 + \frac{(r_i + s)^2}{r^2} \right)$$

(3.89)

$$\dot{\epsilon}_z = \frac{r_i^2}{s(2r_i + s)} \frac{\dot{u}}{b}$$

$$\dot{\epsilon}_{\theta r} = \dot{\epsilon}_{\theta z} = \dot{\epsilon}_{zr} = 0$$

The total equivalent plastic strain rate for zone II is

$$\dot{\bar{\epsilon}}_{II} = \sqrt{\frac{2}{3}(\dot{\epsilon}_r^2 + \dot{\epsilon}_\theta^2 + \dot{\epsilon}_z^2) + 2(\dot{\epsilon}_{\theta r}^2 + \dot{\epsilon}_{\theta z}^2 + \dot{\epsilon}_{rz}^2)} \quad (3.90)$$

$$\dot{\bar{\epsilon}}_{II} = \frac{\dot{u}}{b} \sqrt{\frac{2}{3}} \sqrt{\left(\frac{r_i^2}{s(2r_i + s)}\right)^2 \left(1 + \frac{(r_i + s)^4}{r^4}\right) + 1} \quad (3.91)$$

For the sake of simplicity

$$\zeta_1 = \left(\frac{r_i^2}{s(2r_i + s)}\right)^2 + 1 \quad (3.92)$$

$$\zeta_2 = \left(\frac{r_i^2}{s(2r_i + s)}\right)^2 (r_i + s)^4 \quad (3.93)$$

Eq. (3.91) can be written as

$$\dot{\bar{\epsilon}}_{II} = \frac{\dot{u}}{b} \sqrt{\frac{2}{3}} \sqrt{\zeta_1 + \frac{\zeta_2}{r^4}} \quad (3.94)$$

**Rigid Zone**

The strain rates and the total equivalent plastic strain are equal to zero since this zone does rigid body motion.

$$\dot{\epsilon}_{ij} = 0 \quad \dot{\bar{\epsilon}}_{III} = 0 \quad (3.95)$$

The total power can be calculated by using the Eq. (3.26) for Upper Bound Formulation. The internal power for deformation zone I is:

$$P_I = \int_0^{r_i} \sigma_{f0} \dot{\epsilon}_I dV = \int_0^{r_i} \sigma_{f0} \frac{\dot{u}}{b} 2\pi r b dr \quad (3.96)$$

$$P_I = \int_0^{r_i} \sigma_{f0} \dot{u} 2\pi r dr \quad (3.97)$$

$$P_I = \sigma_{f0} \dot{u} \pi r_i^2 \quad (3.98)$$

The internal power for deformation for zone II is:

$$P_{II} = \int_{r_i}^{r_i+s} \sigma_{f0} \dot{\epsilon}_{II} dV \quad (3.99)$$

$$P_{II} = \int_{r_i}^{r_i+s} \sigma_{f0} \frac{\dot{u}}{b} \sqrt{\frac{2}{3}} \sqrt{\zeta_1 + \frac{\zeta_2}{r^4}} 2\pi r b dr \quad (3.100)$$

When the constant terms are factored out

$$P_{II} = 2\pi \sqrt{\frac{2}{3}} \dot{u} \sigma_{f0} \int_{r_i}^{r_i+s} \sqrt{\zeta_1 + \frac{\zeta_2}{r^4}} r dr \quad (3.101)$$

When we integrate

$$P_{II} = 2\pi \sqrt{\frac{2}{3}} \dot{u} \sigma_{f0} \left[ \frac{1}{2} \left( \sqrt{\zeta_1 r^4 + \zeta_2} - \sqrt{\zeta_2} \operatorname{atanh} \left( \frac{\sqrt{\zeta_2}}{\sqrt{\zeta_1 r^4 + \zeta_2}} \right) \right) \right]_{r_i}^{r_i+s} \quad (3.102)$$

Inserting integration limits Eq. (3.102)

$$\begin{aligned}
 P_{II} = & 2\sqrt{\frac{2}{3}}\dot{u}\pi\sigma_{f0} \left[ \left( \sqrt{\zeta_1 r_i^4 + \zeta_2} \right. \right. \\
 & \left. \left. - \sqrt{\zeta_2} \operatorname{atanh} \left( \frac{\sqrt{\zeta_2}}{\sqrt{\zeta_1 (r_i + s)^4 + \zeta_2}} \right) \right) \right] \\
 & - \left[ \left( \sqrt{\zeta_1 r_i^4 + \zeta_2} - \sqrt{\zeta_2} \operatorname{atanh} \left( \frac{\sqrt{\zeta_2}}{\sqrt{\zeta_1 r_i^4 + \zeta_2}} \right) \right) \right]
 \end{aligned} \tag{3.103}$$

When we substitute Eq. (3.92) and Eq. (3.93) and arrange the terms

$$\begin{aligned}
 P_{II} = & \sqrt{\frac{2}{3}}\dot{u}\pi\sigma_{f0} \left\{ \left[ \left( \frac{(r_i + s)^2}{s(2r_i + s)} \zeta_3 \right) - \frac{r_i^2 (r_i + s)^2}{s(2r_i + s)} \operatorname{atanh} \left( \frac{\frac{r_i^2 (r_i + s)^2}{s(2r_i + s)}}{\frac{(r_i + s)^2}{s(2r_i + s)} \zeta_3} \right) \right] \right. \\
 & \left. - \left[ \left( \frac{r_i^2}{s(2r_i + s)} \zeta_4 \right) - \frac{r_i^2 (r_i + s)^2}{s(2r_i + s)} \operatorname{atanh} \left( \frac{\frac{r_i^2 (r_i + s)^2}{s(2r_i + s)}}{\frac{r_i^2}{s(2r_i + s)} \zeta_4} \right) \right] \right\}
 \end{aligned} \tag{3.104}$$

where,

$$\zeta_3 = \sqrt{2r_i^4 + 4r_i^2 s^2 + 4r_i s^3 + s^4} \tag{3.105}$$

$$\zeta_4 = \sqrt{r_i^4 + (r_i + s)^4 + 4r_i^2 s^2 + 4r_i s^3 + s^4} \tag{3.106}$$

When we simplify Eq. (3.104)

$$P_{II} = \sqrt{\frac{2}{3}} \dot{\mu} \pi \sigma_{f0} \left\{ \left[ \left( \frac{(r_i + s)^2}{s(2r_i + s)} \zeta_3 \right) - \frac{r_i^2 (r_i + s)^2}{s(2r_i + s)} \operatorname{atanh} \left( \frac{r_i^2}{\zeta_3} \right) \right] \right. \\ \left. - \left[ \left( \frac{r_i^2}{s(2r_i + s)} \zeta_4 \right) - \frac{r_i^2 (r_i + s)^2}{s(2r_i + s)} \operatorname{atanh} \left( \frac{(r_i + s)^2}{\zeta_4} \right) \right] \right\} \quad (3.107)$$

When we factor out the  $r_i^2$  from Eq. (3.107)

$$P_{II} = \sqrt{\frac{2}{3}} \dot{\mu} \pi \sigma_{f0} \left\{ \left[ \left( \frac{(r_i + s)^2}{r_i^2 s(2r_i + s)} \zeta_3 \right) - \frac{(r_i + s)^2}{s(2r_i + s)} \operatorname{atanh} \left( \frac{r_i^2}{\zeta_3} \right) \right] \right. \\ \left. - \left[ \left( \frac{1}{s(2r_i + s)} \zeta_4 \right) - \frac{(r_i + s)^2}{s(2r_i + s)} \operatorname{atanh} \left( \frac{(r_i + s)^2}{\zeta_4} \right) \right] \right\} \quad (3.108)$$

The shear power for zone I is:

$$P_{\Gamma_1} = \int_0^h \frac{\sigma_{f0}}{\sqrt{3}} |\Delta v_t| d\Gamma_1 = \int_0^h \frac{\sigma_{f0}}{\sqrt{3}} |\dot{u}_{zII} - \dot{u}_{zI}|_{r=r_i} 2\pi r_i dz \quad (3.109)$$

The velocities in z-direction are:

$$\dot{u}_{zII} = \frac{r_i^2}{s(2r_i + s)} \frac{\dot{u}}{b} z \\ \dot{u}_{zI} = \frac{\dot{u}}{b} z \quad (3.110)$$

Inserting them into the equation:

$$P_{\Gamma_1} = \int_0^b \frac{\sigma_{f0}}{\sqrt{3}} \left| \frac{r_i^2}{s(2r_i + s)} \frac{\dot{u}}{b} z + \frac{\dot{u}}{b} z \right|_{r=r_i} 2\pi r_i dz \quad (3.111)$$

$$P_{\Gamma_1} = \frac{\sigma_{f0}}{\sqrt{3}} 2\pi r_i \frac{\dot{u}}{b} \left[ \frac{r_i^2}{s(2r_i + s)} + 1 \right] \int_0^b z dz \quad (3.112)$$

$$P_{\Gamma_1} = \frac{\sigma_{f0}}{\sqrt{3}} 2\pi r_i \frac{\dot{u}}{b} \left[ \frac{r_i^2}{s(2r_i + s)} + 1 \right] \frac{b^2}{2} \quad (3.113)$$

$$P_{\Gamma_1} = \frac{\sigma_{f0}}{\sqrt{3}} \pi r_i \dot{u} b \left[ \frac{r_i^2}{s(2r_i + s)} + 1 \right] \quad (3.114)$$

The shear power for zone II is:

$$P_{\Gamma_2} = \int_{r_i}^{r_i+s} \frac{\sigma_{f0}}{\sqrt{3}} |\Delta v_t|_{z=b} d\Gamma_2 = \int_{r_i}^{r_i+s} \frac{\sigma_{f0}}{\sqrt{3}} |\dot{u}_{nl}|_{z=b} 2\pi r_i dr \quad (3.115)$$

The velocities for the discontinuities are:

$$\dot{u}_{nl} = \frac{r_i^2}{2s(2r_i + s)} \frac{\dot{u}}{b} \left( -r + \frac{(r_i + s)^2}{r} \right) \quad (3.116)$$

Inserting them into the Eq. (3.104)

$$P_{\Gamma_2} = \int_{r_i}^{r_i+s} \frac{\sigma_{f0}}{\sqrt{3}} \frac{r_i^2}{2s(2r_i + s)} \frac{\dot{u}}{b} \left( -r + \frac{(r_i + s)^2}{r} \right) 2\pi r dr \quad (3.117)$$

$$P_{\Gamma_2} = \int_{r_i}^{r_i+s} \frac{\sigma_{f0}}{\sqrt{3}} \frac{r_i^2}{2s(2r_i+s)} \frac{\dot{u}}{b} (-r^2 + (r_i+s)^2) 2\pi dr \quad (3.118)$$

When we integrate with respect to  $r$

$$P_{\Gamma_2} = \frac{\sigma_{f0}}{\sqrt{3}} \frac{\pi r_i^2}{s(2r_i+s)} \frac{\dot{u}}{b} \left[ -\frac{r^3}{3} + r(r_i+s)^2 \right]_{r_i}^{r_i+s} \quad (3.119)$$

$$P_{\Gamma_2} = \frac{\sigma_{f0}}{\sqrt{3}} \frac{\pi r_i^2}{s(2r_i+s)} \frac{\dot{u}}{b} \left[ \left( \frac{(r_i+s)^3}{3} - (r_i+s)^3 \right) - \left( -\frac{r_i^3}{3} + (r_i+s)^2 r_i \right) \right] \quad (3.120)$$

When simplified

$$P_{\Gamma_2} = \frac{\sigma_{f0}}{\sqrt{3}} \frac{\pi r_i^2}{s(2r_i+s)} \frac{\dot{u}}{b} \left[ \left( \frac{2(r_i+s)^3}{3} \right) + \left( \frac{r_i^3}{3} \right) - (r_i+s)^2 r_i \right] \quad (3.121)$$

$$P_{\Gamma_2} = \frac{\sigma_{f0}}{\sqrt{3}} \frac{\pi r_i^2}{s(2r_i+s)} \frac{\dot{u}}{b} \left[ \frac{s^2(2s+3r_i)}{3} \right] \quad (3.122)$$

The friction power can be calculated for the three surfaces of velocity discontinuity.

$$P_f = \int_{S_{\Gamma}} \tau |\Delta v| dS \quad (3.123)$$

Where the shear stress is

$$\tau_{fr} = \frac{m\sigma_{f0}}{\sqrt{3}} \quad (3.124)$$

The friction power that is necessary to overcome the friction between the workpiece and die, workpiece and punch in zone I can be calculated as

$$P_{\Gamma 3} = 2 \int_0^{r_i} \frac{m\sigma_{f0}}{\sqrt{3}} |\dot{u}_{r1}| 2\pi r dr \quad (3.125)$$

$$P_{\Gamma 3} = \frac{2m\sigma_{f0}}{\sqrt{3}} \pi \frac{\dot{u}}{b} \int_0^{r_i} r^2 dr \quad (3.126)$$

$$P_{\Gamma 3} = \frac{2m\sigma_{f0}}{3\sqrt{3}} \pi r_i^3 \frac{\dot{u}}{b} \quad (3.127)$$

Notice that the power is multiplied with a factor two due to the fact that there are two friction surfaces.

The friction power for zone II has two components. The first friction surface is at the bottom of the die and the second is at the die wall. The formulation of the total friction power is as follows:

$$P_{\Gamma 4} = \int_0^b \frac{m\sigma_{f0}}{\sqrt{3}} |\dot{u}_{z1}| 2\pi r_i dz \quad (3.128)$$

$$P_{\Gamma 5} = \int_{r_i}^{r_i+s} \frac{m\sigma_{f0}}{\sqrt{3}} |\dot{u}_{r1}| 2\pi r dr \quad (3.129)$$

Where the first term is the friction power at the die bottom:

$$P_{\Gamma 4} = \int_0^b \frac{m\sigma_{f0}}{\sqrt{3}} \left( \frac{r_i^2}{s(2r_i + s)} \frac{\dot{u}}{b} z \right) 2\pi r_i dz \quad (3.130)$$



When constant terms are factored out

$$P_{\Gamma 4} = \frac{m\sigma_{f0}}{\sqrt{3}} \left( \frac{r_i^2}{s(2r_i + s)} \frac{\dot{u}}{b} \right) 2\pi r_i \int_0^b z dz \quad (3.131)$$

Integrating with respect to  $r$

$$P_{\Gamma 4} = \frac{m\sigma_{f0}}{\sqrt{3}} \left( \frac{r_i^2}{s(2r_i + s)} \frac{\dot{u}}{b} \right) 2\pi r_i \left[ \frac{z^2}{2} \right]_0^b \quad (3.132)$$

$$P_{\Gamma 4} = \frac{m\sigma_{f0}}{\sqrt{3}} \left( \frac{r_i^2}{s(2r_i + s)} \right) \dot{u} b \pi r_i \quad (3.133)$$

$$P_{\Gamma 4} = \frac{m\sigma_{f0}}{\sqrt{3}} \left( \frac{r_i b}{s(2r_i + s)} \right) \dot{u} \pi r_i^2 \quad (3.134)$$

The second term is the friction power at the die wall.

$$P_{\Gamma 5} = \int_r^{r_i+s} \frac{m\sigma_{f0}}{\sqrt{3}} \frac{r_i^2}{2s(2r_i + s)} \frac{\dot{u}}{b} \left( -r + \frac{(r_i + s)^2}{r} \right) 2\pi r dr \quad (3.135)$$

When we factor out the constant terms

$$P_{\Gamma 5} = \frac{m\sigma_{f0}}{2\sqrt{3}} \frac{\pi r_i^2}{s(2r_i + s)} \frac{\dot{u}}{b} \int_r^{r_i+s} \left( -r^2 + (r_i + s)^2 \right) dr \quad (3.136)$$

When we integrate with respect to  $r$

$$P_{\Gamma 5} = \frac{m\sigma_{f0}}{2\sqrt{3}} \frac{\pi r_i^2}{s(2r_i + s)} \frac{\dot{u}}{b} \left[ \left( -\frac{r^3}{3} + r(r_i + s)^2 \right) \right]_r^{r_i+s} \quad (3.137)$$

$$P_{rs} = \frac{m\sigma_{f0}}{2\sqrt{3}} \frac{r_i^2}{s(2r_i+s)} \dot{u} \left[ \left( \frac{(r_i+s)^3}{3} + (r_i+s)^3 \right) - \left( -\frac{r_i^3}{3} + (r_i+s)^2 r_i \right) \right] \quad (3.138)$$

When we simplify the terms

$$P_{rs} = \frac{m\sigma_{f0}}{2\sqrt{3}} \frac{r_i^2}{s(2r_i+s)} \dot{u} \left[ \left( \frac{2(r_i+s)^3}{3} \right) + \left( \frac{r_i^3}{3} \right) - (r_i+s)^2 r_i \right] \quad (3.139)$$

$$+ \frac{m\sigma_{f0}}{\sqrt{3}} \frac{\pi r_i^2}{s(2r_i+s)} \dot{u} \left[ \frac{s^2(2s+3r_i)}{3} \right]$$

When Eq. (3.139) is simplified

$$P_{rs} = \frac{m\sigma_{f0}}{2\sqrt{3}} \frac{r_i^2}{s(2r_i+s)} \dot{u} \left[ \left( \frac{(r_i+s)^3}{3} + (r_i+s)^3 \right) - \left( -\frac{r_i^3}{3} + (r_i+s)^2 r_i \right) \right] \quad (3.140)$$

When Eq. (3.140) is simplified

$$P_{rs} = \frac{m\sigma_{f0}}{\sqrt{3}} \frac{\pi r_i^2}{s(2r_i+s)} \dot{u} \left[ \frac{s^2(2s+3r_i)}{3} \right] \quad (3.141)$$

The total power ( $P_T$ ) is the summation of all the internal deformation, shear and friction losses.

$$\begin{aligned}
p_T = & \sigma_{f0} \dot{\mu} \pi r_i^2 + \sqrt{\frac{2}{3}} \sigma_{f0} \dot{\mu} \pi r_i^2 \left\{ \left[ \left( \frac{(r_i + s)^2}{s r_i^2 (2r_i + s)} \zeta_3 \right) - \frac{(r_i + s)^2}{s(2r_i + s)} \operatorname{atanh} \left( \frac{r_i^2}{\zeta_3} \right) \right] \right. \\
& - \left. \left[ \left( \frac{1}{s(2r_i + s)} \zeta_4 \right) - \frac{(r_i + s)^2}{s(2r_i + s)} \operatorname{atanh} \left( \frac{(r_i + s)^2}{\zeta_4} \right) \right] \right\} \\
& + \frac{\sigma_{f0} \dot{\mu} \pi r_i^2 b}{\sqrt{3}} \left[ \frac{(r_i + s)^2}{r_i (2r_i + s)} \right] + \frac{m \sigma_{f0} \dot{\mu} \pi r_i^2 b}{\sqrt{3}} \left( \frac{r_i}{(2r_i + s)} \right) \\
& + \frac{2m}{\sqrt{3}} r_i \frac{\sigma_{f0} \dot{\mu} \pi r_i^2}{b} + \frac{m+1}{\sqrt{3}} \frac{\sigma_{f0} \dot{\mu} \pi r_i^2}{s b (2r_i + s)} \left[ \frac{s^2 (2s + 3r_i)}{3} \right]
\end{aligned} \tag{3.142}$$

The non-dimensionalized total power ( $p_T$ ) can be expressed non-dimensionally simply by dividing Eq. (3.142) by ideal power term  $\sigma_{f0} \dot{\mu} \pi r_i^2$

$$p_T = \frac{P_T}{\sigma_{f0} \dot{\mu} \pi r_i^2} \tag{3.143}$$

Hence the final equation is found by the author as:

$$\begin{aligned}
p_T = & 1 + \sqrt{\frac{2}{3}} \left\{ \left[ \left( \frac{(r_i + s)^2}{s r_i^2 (2r_i + s)} \zeta_3 \right) - \frac{(r_i + s)^2}{s(2r_i + s)} \operatorname{atanh} \left( \frac{r_i^2}{\zeta_3} \right) \right] \right. \\
& - \left. \left[ \left( \frac{1}{s(2r_i + s)} \zeta_4 \right) - \frac{(r_i + s)^2}{s(2r_i + s)} \operatorname{atanh} \left( \frac{(r_i + s)^2}{\zeta_4} \right) \right] \right\} \\
& + \frac{1}{\sqrt{3}} \frac{b}{s} \left[ \frac{(r_i + s)^2}{r_i (2r_i + s)} \right] + \frac{m}{\sqrt{3}} \frac{b}{s} \left( \frac{r_i}{(2r_i + s)} \right) \\
& + \frac{2m}{\sqrt{3}} r_i \frac{1}{b} + \frac{m+1}{\sqrt{3}} \frac{1}{s b (2r_i + s)} \left[ \frac{s^2 (2s + 3r_i)}{3} \right]
\end{aligned} \tag{3.144}$$

### 3.3.1.3 Three Zone Velocity Field with Thin-Walled Solution

In the previous section, the upper bound solution for three-zone velocity field for a thick walled can was examined. For the previous solution, the wall thickness of the can is comparable with the radius of the die. For the cases of thin-walled cans, an assumption can be introduced. This assumption simplifies the overall solution and eases the force calculations. This approach is proposed by Hoogenboom (2002), for the late stage of backward can extrusion for a simplified solution

$$s/r_i \ll 1 \quad (3.145)$$

This means that the wall thickness of the can is so small compared to inner can diameter that it can be neglected for simplifications.

The following velocity models are used for the three zones stated above:

$$\text{Zone I: } \dot{u}_r = \dot{u}_r(z)$$

$$\text{Zone II: } \dot{u}_z = \dot{u}_z(r)$$

$$\text{Zone III: } \dot{u}_r = 0 \text{ and } \dot{u}_z = \text{constant}$$

In zone I, the upper bound solution for upsetting is used, since this zone experiences the same type of deformation. Therefore the velocity components are:

$$\dot{u}_r = \frac{r}{2b} \dot{u} \quad \dot{u}_z = -\frac{z}{b} \dot{u} \quad (3.146)$$

The corresponding equivalent strain rate is

$$\dot{\bar{\epsilon}} = \frac{\dot{u}}{b} \quad (3.147)$$

The velocities for zone II can be calculated by the volume constancy in the velocity discontinuity surface  $\Gamma_1$  along with the thin wall assumption,

$$\dot{u}_{zII} 2\pi r_i s = \dot{u}_{rI(r=r_i)} 2\pi r_i z \quad (3.148)$$

Inserting the value  $\dot{u}_{rI}$  to the Eq. (3.148);

$$\dot{u}_{zII} = \frac{r_i z}{2sb} \dot{u} \quad (3.149)$$

The radial velocity in zone II can be found by using the volume invariance

$$\frac{1}{r} (\dot{u}_r r)_r = -\dot{u}_{z,z} = -\frac{r_i}{2sb} \dot{u} \quad (3.150)$$

$$\dot{\epsilon}_{rr} + \dot{\epsilon}_{\theta\theta} + \dot{\epsilon}_{zz} = 0 \quad (3.150a)$$

$$\dot{\epsilon}_{rr} = \frac{\partial \dot{u}_{rII}}{\partial r} \quad \dot{\epsilon}_{\theta\theta} = \frac{\dot{u}_{rII}}{r} \quad \dot{\epsilon}_{zz} = \frac{\partial \dot{u}_{zII}}{\partial z} \quad (3.150b)$$

$$\frac{\partial \dot{u}_{rII}}{\partial r} + \frac{1}{r} \dot{u}_{rII} + \dot{\epsilon}_{zz} = 0 \quad (3.150c)$$

$$\frac{1}{r} (\dot{u}_{rII} r)_r = -\dot{\epsilon}_{zz} = -\frac{r_i}{2sb} \dot{u} \quad (3.150d)$$

When we integrate Eq. (3.150d)

$$(\dot{u}_{rII} r) = \int_{r_i}^{r_i+s} -\frac{r_i}{2sb} \dot{u} r dr \quad (3.151a)$$

$$(\dot{u}_{rII} r) = -\dot{u} \frac{r_i}{2sb} \left[ \frac{r^2}{2} \right]_{r_0}^r \quad (3.151b)$$

$$(\dot{u}_{rII} r) = \dot{u} \frac{r_i}{4sb} (r_0^2 - r^2) \quad (3.151c)$$

$$\dot{u}_{rII} = \frac{r_i}{4sb} \frac{r_0^2 - r^2}{r} \dot{u} \quad (3.151d)$$

and with the thin-tube assumption Eq. (3.151d) will become

$$\dot{u}_{rII} = \frac{r_i}{4sb} \frac{(r_0 + r)(r_0 + r)}{r} \dot{u} \quad (3.152)$$

$$\dot{u}_{rII} = \frac{r_i}{4sb} \frac{(r_i + s + r)(r_i - s + r)}{r} \dot{u} \quad (3.153)$$

Assuming  $r=r_i$  and  $s$  is negligible due to thin-walled assumption

$$\dot{u}_{rII} = \frac{r_i}{2sb} \frac{(r_i - s + r)}{r} \dot{u} \quad (3.154)$$

$$\dot{u}_{rII} = \frac{r_i}{2sb} (r_i + s - r) \dot{u} \quad (3.155)$$

The axial velocity in rigid zone (the upward velocity for the can) can be calculated by continuity at the surface of velocity discontinuity  $\Gamma_2$

$$\dot{u}_{III} = \dot{u}_{II(z=h)} = \frac{r_i}{2s} \dot{u} \quad (3.156)$$

The strain rates and the corresponding equivalent strains for the zones can be derived from the velocities.

### Zone I

$$\dot{\epsilon}_r = \dot{\epsilon}_\theta = -\frac{1}{2} \dot{\epsilon}_z = \frac{\dot{u}}{2b} \quad (3.157)$$

$$\dot{\epsilon}_{\theta r} = \dot{\epsilon}_{\theta z} = \dot{\epsilon}_{zr} = 0$$

The equivalent strain rate for zone I is

$$\dot{\bar{\epsilon}}_I = \sqrt{\frac{2}{3}(\dot{\epsilon}_r^2 + \dot{\epsilon}_\theta^2 + \dot{\epsilon}_z^2) + 2(\dot{\epsilon}_{\theta r}^2 + \dot{\epsilon}_{\theta z}^2 + \dot{\epsilon}_{zr}^2)} = -\frac{\dot{u}}{b} \quad (3.158)$$

### Zone II

$$\dot{\epsilon}_r = -\dot{\epsilon}_z = \frac{r_i \dot{u}}{2sb} \quad \dot{\epsilon}_\theta = 0 \quad (3.159)$$

$$\dot{\epsilon}_{\theta r} = \dot{\epsilon}_{\theta z} = \dot{\epsilon}_{zr} = 0$$

The equivalent strain rate for zone II is

$$\dot{\bar{\epsilon}}_{II} = \sqrt{\frac{2}{3}(\dot{\epsilon}_r^2 + \dot{\epsilon}_\theta^2 + \dot{\epsilon}_z^2) + 2(\dot{\epsilon}_{\theta r}^2 + \dot{\epsilon}_{\theta z}^2 + \dot{\epsilon}_{zr}^2)} = \frac{1}{\sqrt{3}} \frac{r_i \dot{u}}{sb} \quad (3.160)$$

### Rigid Zone

Since the rigid zone only experiences rigid body motion, there will be no deformation;

$$\dot{\epsilon}_{ij} = 0 \quad (3.161)$$

$$\dot{\bar{\epsilon}}_{III} = \sqrt{\frac{2}{3}(\dot{\epsilon}_r^2 + \dot{\epsilon}_\theta^2 + \dot{\epsilon}_z^2) + 2(\dot{\epsilon}_{\theta r}^2 + \dot{\epsilon}_{\theta z}^2 + \dot{\epsilon}_{zr}^2)} = 0 \quad (3.162)$$

The total power can be calculated by using the Eq. (3.26) for Upper Bound Formulation.

The internal power for deformation zone I is:

$$P_I = \int_0^{r_i} \sigma_{f0} \dot{\epsilon}_I dV = \int_0^{r_i} \sigma_{f0} \frac{\dot{u}}{b} 2\pi r b dr \quad (3.163)$$

$$P_I = \int_0^{r_i} \sigma_{f0} \dot{u} 2\pi r dr \quad (3.164)$$

$$P_I = \sigma_{f0} \dot{u} 2\pi r_i^2 \quad (3.165)$$



The internal power for deformation for zone II is:

$$P_{II} = \int_{r_i}^{r_i+s} \sigma_{f0} \dot{\epsilon}_{II} dV \quad (3.166)$$

When we insert the equivalent strain rate for zone II

$$P_{II} = \int_{r_i}^{r_i+s} \sigma_{f0} \frac{1}{\sqrt{3}} \frac{r_i}{sb} \dot{u} 2\pi r b dr \quad (3.167)$$

When we factor out the constant terms

$$P_{II} = \frac{2\pi}{\sqrt{3}} \frac{r_i}{s} \dot{u} \sigma_{f0} \int_{r_i}^{r_i+s} r dr \quad (3.168)$$

Integrating Eq. (3.168)

$$P_{II} = \frac{2\pi}{\sqrt{3}} \frac{r_i}{s} \dot{u} \sigma_{f0} \frac{(r_i+s)^2 - r_i^2}{2} \quad (3.169)$$

Simplifying Eq. (3.169)

$$P_{II} = \frac{2\pi}{\sqrt{3}} \frac{r_i}{s} \dot{u} \sigma_{f0} \frac{s(2r_i+s)}{2} \quad (3.170)$$

Due to the thin-walled assumption the wall thickness  $s$  is negligible

$$P_{II} = \frac{2\pi}{\sqrt{3}} \frac{r_i}{s} \dot{u} \sigma_{f0} \frac{(2r_i+s^0)s}{2} \quad (3.171)$$

$$P_{II} = \frac{2\pi}{\sqrt{3}} r_i^2 \dot{u} \sigma_{f0} \quad (3.172)$$

Due to the thin-walled assumption the wall thickness  $s$  is negligible

$$P_{II} = \frac{2\pi}{\sqrt{3}} \frac{r_i}{s} \dot{u} \sigma_{f0} \frac{(2r_i + s^0)s}{2} \quad (3.173)$$

When simplified

$$P_{II} = \frac{2\pi}{\sqrt{3}} r_i^2 \dot{u} \sigma_{f0} \quad (3.174)$$

The shear power for zone I is:

$$P_{\Gamma I} = \int_0^b \frac{\sigma_{f0}}{\sqrt{3}} |\Delta v_t| d\Gamma_1 = \int_0^b \frac{\sigma_{f0}}{\sqrt{3}} |\dot{u}_{zII} - \dot{u}_{zI}|_{r=r_i} 2\pi r_i dz \quad (3.175)$$

The velocities in  $z$ -direction are:

$$\dot{u}_{zI} = \frac{z}{2sb} \dot{u} \quad \dot{u}_{zII} = \frac{r_i z}{b} \dot{u} \quad (3.176)$$

Inserting them into the equation:

$$P_{\Gamma I} = \int_0^b \frac{\sigma_{f0}}{\sqrt{3}} \left| \frac{z}{2sb} \dot{u} - \frac{r_i z}{b} \dot{u} \right|_{r=r_i} 2\pi r_i dz \quad (3.177)$$

When we factor out the constant terms

$$P_{\Gamma 1} = \frac{\sigma_{f0}}{\sqrt{3}} 2\pi \dot{u} r_i \left( \frac{r_i}{2sb} + \frac{1}{b} \right) \int_0^b z dz \quad (3.178)$$

When we integrate with respect to  $z$  and insert boundary conditions

$$P_{\Gamma 1} = \frac{\sigma_{f0}}{\sqrt{3}} 2\pi \dot{u} r_i \left( \frac{r_i}{2sb} + \frac{1}{b} \right) \frac{b^2}{2} \quad (3.179)$$

Simplifying Eq. (3.179)

$$P_{\Gamma 1} = \frac{\sigma_{f0}}{\sqrt{3}} 2\pi \dot{u} r_i b \left( \frac{r_i}{2s} + 1 \right) \quad (3.180)$$

The thin-wall assumption results in

$$P_{\Gamma 1} = \frac{\sigma_{f0}}{\sqrt{3}} 2\pi \dot{u} r_i b \left( \frac{r_i + 2s}{2s} \right) \quad (3.181)$$

$$P_{\Gamma 1} = \frac{\pi}{2\sqrt{3}} \sigma_{f0} \dot{u} r_i^2 \frac{b}{s} \quad (3.182)$$

The shear power for zone II is:

$$P_{\Gamma 2} = \int_{r_i}^{r_i+s} \frac{\sigma_{f0}}{\sqrt{3}} |\Delta v_r|_{z=b} d\Gamma_2 = \int_{r_i}^{r_i+s} \frac{\sigma_{f0}}{\sqrt{3}} |\dot{u}_{rII}|_{z=b} 2\pi r_i dr \quad (3.183)$$

The velocity for the discontinuity is:

$$\dot{u}_{rII} = \frac{r_i}{2sb} (r_i + s - r) \dot{u} \quad (3.184)$$

Inserting them into the Eq. (3.183)

$$P_{r2} = \int_{r_i}^{r_i+s} \frac{\sigma_{f0}}{\sqrt{3}} \frac{r_i}{2sb} (r_i + s - r) \dot{u} 2\pi r_i dr \quad (3.185)$$

When we integrate with respect to  $r$

$$P_{r2} = \frac{\sigma_{f0}}{\sqrt{3}} \frac{r_i^2 \pi}{sb} \dot{u} \left[ (r_i + s)r - \frac{r^2}{2} \right]_{r_i}^{r_i+s} \quad (3.186)$$

When the boundary conditions are inserted

$$P_{rII} = \frac{\sigma_{f0}}{\sqrt{3}} \frac{r_i^2 \pi}{sb} \dot{u} \left[ \left( (r_i + s)^2 - \frac{(r_i + s)^2}{2} \right) - \left( (r_i + s)^2 r_i - \frac{r_i^2}{2} \right) \right] \quad (3.187)$$

$$P_{rII} = \frac{\sigma_{f0}}{\sqrt{3}} \frac{r_i^2 \pi}{sb} \dot{u} \left\{ \left[ \left( r_i^2 + s^2 + 2r_i s \right) - \left( \frac{r_i^2}{2} + \frac{s^2}{2} + r_i s \right) \right] - \left[ \left( r_i^2 + r_i s - \frac{r_i^2}{2} \right) \right] \right\} \quad (3.188)$$

When we simplify Eq. (3.188)

$$P_{rII} = \frac{\sigma_{f0}}{\sqrt{3}} \frac{r_i^2 \pi}{sb} \dot{u} \left[ \left( \frac{r_i^2}{2} + \frac{s^2}{2} + r_i s \right) - \left( \frac{r_i^2}{2} + r_i s \right) \right] \quad (3.189)$$

The thin-wall assumption results in:

$$P_{\Gamma II} = \frac{\sigma_{f0}}{\sqrt{3}} \frac{r_i^2 \pi}{2b} \dot{u} \frac{s^2}{2} \quad (3.190)$$

$$P_{\Gamma II} = \frac{\sigma_{f0}}{\sqrt{3}} \frac{\pi r_i^2}{b} \dot{u} \frac{s}{2} \quad (3.191)$$

The friction power can be calculated for the three surfaces of velocity discontinuities.

$$P_f = \int_{S_T} \tau |\Delta v| dS \quad (3.192)$$

Where the shear stress is

$$\tau_{fr} = \frac{m\sigma_{f0}}{\sqrt{3}} \quad (3.193)$$

The friction power that is necessary to overcome the friction between the workpiece and die, workpiece and punch in zone I can be calculated as

$$P_{\Gamma 3} = 2 \int_0^{r_i} \frac{m\sigma_{f0}}{\sqrt{3}} |\dot{u}_{r1}| 2\pi r dr \quad (3.194)$$

When we factor out the constant terms

$$P_{\Gamma 3} = \frac{2m\sigma_{f0}}{\sqrt{3}} \int_0^{r_i} \frac{r}{2b} \dot{u} 2\pi r dr \quad (3.195)$$

$$P_{\Gamma 3} = \frac{2m\sigma_{f0}\dot{u}\pi}{\sqrt{3}b} \int_0^{r_i} r^2 dr \quad (3.196)$$

When we integrate with respect to  $r$

$$P_{\Gamma 3} = \frac{2m\sigma_{f0}\dot{\mu}\pi r_i^2}{3\sqrt{3}} \frac{r_i}{b} \quad (3.197)$$

The friction power for zone II has two components. The first friction surface is at the bottom of the die and the second is at the die wall. The formulation of the total friction power is as follows:

$$P_{\Gamma 5+\Gamma 4} = \int_{r_i}^{r_i+s} \frac{m\sigma_{f0}}{\sqrt{3}} |\dot{\mu}_{rII}| 2\pi r_i dr + \int_0^b \frac{m\sigma_{f0}}{\sqrt{3}} |\dot{\mu}_{zII}| 2\pi r_i dz \quad (3.198)$$

Where the first term is the friction power at the die bottom and the second term is the friction power at the die wall.

$$P_{\Gamma 5+\Gamma 4} = \frac{m\sigma_{f0}}{\sqrt{3}} \int_{r_i}^{r_i+s} \frac{r_i}{2sb} (r_i + s - r) \dot{\mu} 2\pi r_i dr + \frac{m\sigma_{f0}}{\sqrt{3}} \int_0^b \frac{r_i z}{2sb} \dot{\mu} 2\pi r_i dz \quad (3.199)$$

When we factor out the constant terms

$$P_{\Gamma 5+\Gamma 4} = \frac{m\sigma_{f0}\dot{\mu}\pi r_i^2}{\sqrt{3}sb} \int_{r_i}^{r_i+s} (r_i + s - r) dr + \frac{m\sigma_{f0}\dot{\mu}\pi r_i^2}{\sqrt{3}sb} \int_0^b z dz \quad (3.200)$$

After integration

$$P_{\Gamma 5+\Gamma 4} = \frac{m\sigma_{f0}\dot{\mu}\pi r_i^2}{\sqrt{3}sb} \left[ (r_i + s)r - \frac{r^2}{2} \right]_{r_i}^{r_i+s} + \frac{m\sigma_{f0}\dot{\mu}\pi r_i^2}{\sqrt{3}sb} \left[ \frac{z^2}{2} \right]_0^b \quad (3.201)$$

$$P_{\Gamma5+\Gamma4} = \frac{m\sigma_{f0}\dot{\pi}r_i^2}{\sqrt{3}sb} \left[ \left( (r_i + s)^2 - \frac{(r_i + s)^2}{2} \right) - \left( (r_i + s)r_i - \frac{r_i^2}{2} \right) \right] + \frac{m\sigma_{f0}\dot{\pi}r_i^2}{\sqrt{3}sb} \frac{b}{s} \quad (3.202)$$

When simplified

$$P_{\Gamma5+\Gamma4} = \frac{m\sigma_{f0}\dot{\pi}r_i^2}{\sqrt{3}sb} \left[ \left( \frac{r_i^2}{2} + \frac{s^2}{2} + r_i s \right) - \left( \frac{r_i^2}{2} + r_i \right) \right] + \frac{m\sigma_{f0}\dot{\pi}r_i^2}{\sqrt{3}} \frac{b}{s} \quad (3.203)$$

$$P_{\Gamma5+\Gamma4} = \frac{m\sigma_{f0}\dot{\pi}r_i^2}{\sqrt{3}sb} \left( \frac{s^2}{2} \right) + \frac{m\sigma_{f0}\dot{\pi}r_i^2}{\sqrt{3}} \frac{b}{s} \quad (3.204)$$

$$P_{\Gamma5+\Gamma4} = \frac{m\sigma_{f0}\dot{\pi}r_i^2}{\sqrt{3}} \frac{s}{b} + \frac{m\sigma_{f0}\dot{\pi}r_i^2}{\sqrt{3}} \frac{b}{s} \quad (3.205)$$

The total power ( $P_T$ ) is the summation of all the internal deformation, shear and friction losses.

$$\begin{aligned} P_T &= \sigma_{f0}\dot{\pi}r_i^2 + \frac{2}{\sqrt{3}}\sigma_{f0}\dot{\pi}r_i^2 + \frac{1}{2\sqrt{3}}\sigma_{f0}\dot{\pi}r_i^2 \frac{b}{s} \\ &+ \frac{1}{2\sqrt{3}}\sigma_{f0}\dot{\pi}r_i^2 \frac{s}{b} + \frac{1}{\sqrt{3}}m\sigma_{f0}\dot{\pi}r_i^2 \frac{s}{b} + \frac{1}{\sqrt{3}}m\sigma_{f0}\dot{\pi}r_i^2 \frac{b}{s} \\ &+ \frac{2}{3\sqrt{3}}m\sigma_{f0}\dot{\pi}r_i^2 \frac{r_i}{b} \end{aligned} \quad (3.206)$$

The non-dimensionalized total power ( $p_T$ ) can be expressed non-dimensional simply by dividing the term into

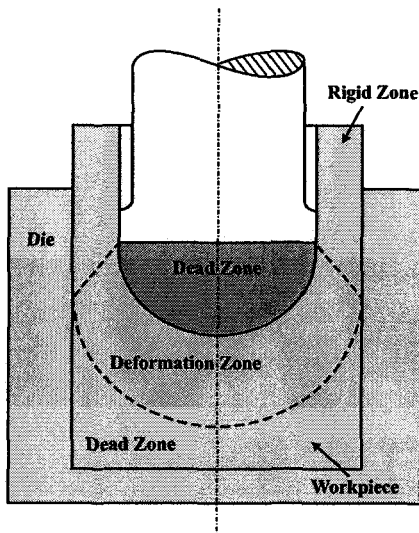
$$p_T = \frac{P_T}{\sigma_{f0}\dot{\pi}r_i^2} \quad (3.207)$$

$$p_r = 1 + \frac{2}{\sqrt{3}} + \frac{m+1}{2\sqrt{3}} \left( \frac{s}{b} + \frac{b}{s} \right) + \frac{2m}{3\sqrt{3}} \frac{r_i}{b} \quad (3.208)$$

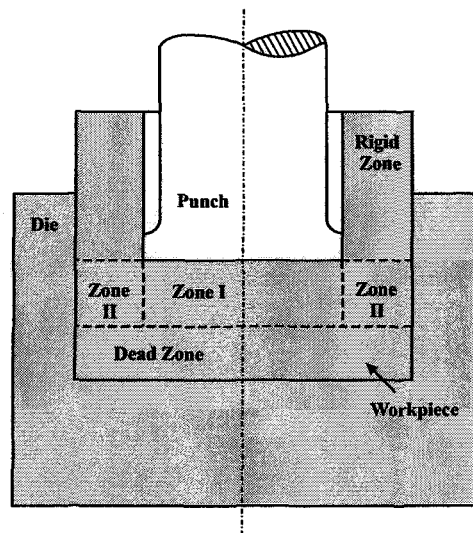
### 3.3.2 Early Stage

The early stage of backward can extrusion is characterized by two zones that lie under the punch, one of which is a deforming zone and the other is a dead-zone. The velocity fields that are used for late stage solution are no longer valid. This results in a different formulation than the late stage solution. The two possible velocity fields that can be used in this case can be seen in Figure 3.7. The three-zone velocity field which is proposed by Kudo (1960) is modified by Hoogenboom (2002) with an addition of a dead zone to the die bottom. This is due to the fact the in the early stage only some portion of the material deforms and there exists a dead zone which is between the deforming zone and the die bottom. The spherical velocity field which is proposed by Avitzur (1972) for early stage divides the material into four zones, with only one deforming zone and two dead zones and a rigid zone. In Avitzur's (1972) model, the deformation zone lies between two dead zones. The material right under the punch and the material between the deforming zone and the die bottom are considered to be undeformed.





Spherical Velocity Field  
(Avitzur)



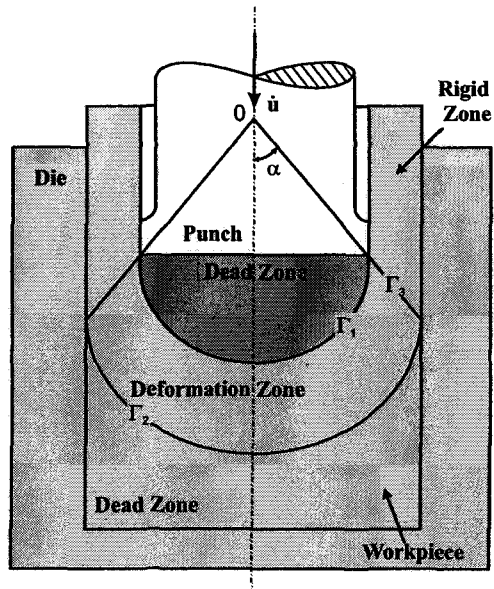
Three-Zone Velocity Field  
with a Dead-Zone (Hoogenboom)

Figure 3.7 Velocity Field for Early Stage

### 3.3.2.1 Spherical Velocity Field

In Avitzur's (1972) solution a spherical velocity field has been used for the early stage solution of backward can extrusion. This velocity field was proposed by Kudo on the basis of the solution by Avitzur (1964) of the problem of flow-through conical converging dies.

In this model, the velocity field is divided into four zones as show in Figure 3.8. The one and only deforming zone is located between two dead zones. The first dead zone is at the die bottom and the other lies under the punch and does not go through any deformation till the bottom thickness of the can drops to a certain value. The rigid zone lies in the annular gap between the punch and the die.



**Figure 3.8** Spherical Velocity Field

The surfaces of velocity discontinuity are  $\Gamma_1$ ,  $\Gamma_2$ ,  $\Gamma_3$  as shown in Figure 3.9. Along these surfaces the possibility for drastic velocity changes are very probable. The velocity in deforming zone is radial only. The velocity decreases from the shear

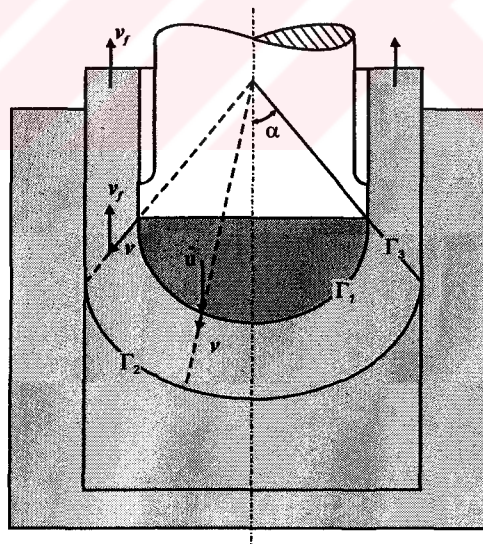


**Figure 3.9** Velocity Discontinuities

surface  $\Gamma_1$  to  $\Gamma_2$ . The radial downward velocity field results in the upward motion of the tube produced (Figure 3.10).



The velocity components for the spherical model is found by volume constancy for the spherical velocity field. The velocity  $v_f$  which is defined in Figure 3.9, can be written in terms of process parameters as:

$$\dot{u}\pi r_i^2 = v_f \pi (r_0^2 - r_i^2) \quad (3.209)$$

which will result in

$$v_f = -\dot{u} \frac{1}{\left(\left(r_0/r_i\right)^2 - 1\right)} \quad (3.210)$$

The velocity  $v_f$  can be subtracted from the all velocity components of the system. This will result in a model similar to the flow of converging dies which is proposed by Avitzur (1964 ). The dead zone at the bottom of the die will have a velocity equal to  $v_f$  but in opposite direction where as zone III will be stationary.

The flow being symmetric about the  $z$ -axis the velocity components in  $\theta$  and  $\phi$  directions in the spherical coordinate system will be equal to zero. The remaining non-zero velocity component  $\dot{u}_r$  will be determined by volume constancy.

The volumetric flow rate of the material in rigid zone is equal to:

$$\dot{V}_{IV} = 2\pi r i d r \frac{1}{\left(1 - (r_i/r_0)^2\right)} \quad (3.211)$$

The flow rate for deforming zone is equal to

$$\dot{V}_{II} = 2\pi r \sin \theta r d\theta \dot{u}_r \quad (3.212)$$

In order to find the radial velocity component the volumetric flow rates for the neighboring zones are equalized and the result will be equal to:

$$\dot{u}_r = \left(\frac{r_1}{r}\right)^2 \frac{1}{(1-(r_i/r_0)^2)} \dot{u} \cos \theta \quad (3.213)$$

The strain rates for deforming zone can be calculated by using the equations of volume constancy.

$$\dot{\epsilon}_{rr} + \dot{\epsilon}_{\theta\theta} + \dot{\epsilon}_{\phi\phi} = 0 \quad (3.214)$$

Strain in radial direction

$$\dot{\epsilon}_{rr} = \frac{\partial \dot{u}_r}{\partial r} = -\frac{2}{r} \left(\frac{r_1}{r}\right)^2 \frac{1}{(1-(r_i/r_0)^2)} \dot{u} \cos \theta \quad (3.215)$$

Strain in  $\theta$ -direction

$$\dot{\epsilon}_{\theta\theta} = \frac{1}{r} \frac{\partial \dot{u}_\theta}{\partial \theta} + \frac{\dot{u}_r}{r} = -\frac{1}{r} \left(\frac{r_1}{r}\right)^2 \frac{1}{(1-(r_i/r_0)^2)} \dot{u} \cos \theta \quad (3.216)$$

Strain in  $\phi$ -direction

$$\dot{\epsilon}_{\phi\phi} = \frac{1}{r \sin \theta} \frac{\partial \dot{u}_\phi}{\partial \phi} + \frac{\dot{u}_r}{r} + \frac{\dot{u}_\theta \cot \theta}{r} = \frac{1}{r} \left(\frac{r_1}{r}\right)^2 \frac{1}{(1-(r_i/r_0)^2)} \dot{u} \cos \theta \quad (3.217)$$

Shear strain on  $r\theta$ -plane

$$\dot{\epsilon}_{r\theta} = \frac{1}{2} \left( \frac{\partial \dot{u}_\theta}{\partial r} - \frac{\dot{u}_\theta}{r} + \frac{1}{r} \frac{\partial \dot{u}_r}{\partial \theta} \right) = -\frac{1}{2r} \left(\frac{r_1}{r}\right)^2 \frac{1}{(1-(r_i/r_0)^2)} \dot{u} \sin \theta \quad (3.218)$$

Shear strain on  $\phi\theta$ -plane

$$\dot{\epsilon}_{\phi\theta} = \frac{1}{2} \left( \frac{1}{r \sin \theta} \frac{\partial \dot{u}_\theta}{\partial \phi} + \frac{1}{r} \frac{\partial \dot{u}_\phi}{\partial \theta} - \frac{\dot{u}_\phi \cot \theta}{r} \right) = 0 \quad (3.219)$$

Shear strain on  $\phi r$ -plane

$$\dot{\epsilon}_{\phi r} = \frac{1}{2} \left( \frac{\partial \dot{u}_\phi}{\partial r} - \frac{\dot{u}_\phi}{r} + \frac{1}{r \sin \theta} \frac{\partial \dot{u}_r}{\partial \phi} \right) = 0 \quad (3.220)$$

The power terms can be calculated as follows:

$$\dot{W}_i = \frac{2\sigma_{f0}}{\sqrt{3}} \int_V \sqrt{\frac{1}{2} \dot{\epsilon}_{ij}^* \dot{\epsilon}_{ij}^*} dV \quad (3.221)$$

$$\dot{W}_i = \frac{2\sigma_{f0}}{\sqrt{3}} \int_V \sqrt{\frac{1}{2} (\dot{\epsilon}_{rr}^2 + \dot{\epsilon}_{\theta\theta}^2 + \dot{\epsilon}_{\phi\phi}^2 + 2\dot{\epsilon}_{r\theta}^2 + 2\dot{\epsilon}_{r\phi}^2 + 2\dot{\epsilon}_{\theta\phi}^2)} dV \quad (3.222)$$

The volume is expressed as

$$dV = 2\pi r \sin \theta r d\theta dr \quad (3.223)$$

The double derivative in the Eq. (3.223) results in a double integral for the calculation of the total power. When the volume and the related strain rates are insterted to the Eq. (3.222), the result will be:

$$\dot{W}_i = 4\pi\sigma_{f0} |\dot{u}| r_i^2 \frac{1}{(1 - (r_i/r_0)^2)} \int_{\theta=0}^{\alpha} \int_{r=r_1}^{r_2} \sin \theta \sqrt{1 - \frac{11}{12} \sin^2 \theta} \frac{dr}{r} d\theta \quad (3.224)$$



$$\dot{W}_i = 2\pi\sigma_{f_0} |\dot{u}| r_i^2 \frac{1}{(1 - (r_i/r_0)^2)} f(\alpha) \ln(r_0/r_i) \quad (3.225)$$

Where

$$f(\alpha) = \frac{1}{\sin^2 \alpha} \left[ 1 - \cos \alpha \sqrt{1 - 11/12 \sin^2 \alpha} + \frac{1}{\sqrt{11/12}} \ln \frac{1 + \sqrt{11/12}}{\sqrt{11/12} \cos \alpha + \sqrt{1 - 11/12 \sin^2 \alpha}} \right] \quad (3.226)$$

The friction losses can be calculated as

$$\dot{W}_f = \frac{m\sigma_{f_0}}{\sqrt{3}} \int_S |\Delta v| dS \quad (3.227)$$

Along the friction surface  $\Gamma_5$  the velocity is equal to  $v_f$

$$|\Delta v| = -\dot{u} \frac{1}{((r_0/r_i)^2 - 1)} \quad (3.228)$$

The surface element assumed to be equal to

$$dS = 2\pi r_i dz \quad (3.229)$$

This will result

$$\dot{W}_{f5} = \frac{m\sigma_{f_0}}{\sqrt{3}} \int_S -\dot{u} \frac{1}{((r_0/r_i)^2 - 1)} 2\pi r_i dz \quad (3.230)$$

$$\dot{W}_{f5} = \frac{-2\pi}{\sqrt{3}} m\sigma_{f_0} \dot{u} r_i h \frac{1}{((r_0/r_i)^2 - 1)} \quad (3.231)$$

The other friction plane is  $\Gamma_4$  which has the same relative velocity as  $\Gamma_5$

$$|\Delta v| = -\dot{u} \frac{1}{\left(\left(\frac{r_0}{r_i}\right)^2 - 1\right)} \quad (3.232)$$

The surface element assumed to be equal to

$$dS = 2\pi r_0 dz \quad (3.233)$$

which result in

$$\dot{W}_{f4} = \frac{-2\pi}{\sqrt{3}} m \sigma_{f0} \dot{u} r_0 h \left[ b_0 + (r_0 - r_i) \cot \alpha \right] \left( \frac{\left(\frac{r_i}{r_0}\right)^2}{1 - \left(\frac{r_i}{r_0}\right)^2} \right) \quad (3.234)$$

The shear losses for the planes  $\Gamma_1, \Gamma_2, \Gamma_3$  can be determined by

$$\dot{W}_s = \frac{\sigma_{f0}}{\sqrt{3}} \int_s |\Delta v| dS \quad (3.235)$$

For  $\Gamma_1$  surface:

The discontinuity velocity is

$$|\Delta v| = -\dot{u} \frac{1}{\left(\left(\frac{r_0}{r_i}\right)^2 - 1\right)} \sin \theta \quad (3.236)$$

The volume is

$$dV = 2\pi r_1 \sin \theta r_1 d\theta \quad (3.237)$$



This will result in

$$\dot{W}_{s1} = \frac{-\pi}{\sqrt{3}} \sigma_{f0} \dot{u} r_i^2 \frac{1}{(1 - (r_i/r_0)^2)} \left( \frac{\alpha}{\sin^2 \alpha} - \cot \alpha \right) \quad (3.238)$$

For  $\Gamma_2$  surface:

The discontinuity velocity is

$$|\Delta v| = -\dot{u} \frac{1}{((r_0/r_i)^2 - 1)} \sin \theta \quad (3.239)$$

The surface of velocity discontinuity is

$$dS = 2\pi r_2 \sin \theta r_2 d\theta \quad (3.240)$$

This will result in

$$\dot{W}_{s1} = \frac{-\pi}{\sqrt{3}} \sigma_{f0} \dot{u} r_i^2 \frac{1}{(1 - (r_i/r_0)^2)} \left( \frac{\alpha}{\sin^2 \alpha} - \cot \alpha \right) \quad (3.241)$$

For  $\Gamma_3$  surface:

The discontinuity velocity is

$$|\Delta v| = \left( \frac{r_1}{r} \right)^2 \frac{1}{(1 - (r_i/r_0)^2)} \dot{u} \cos \alpha \quad (3.242)$$

The surface of velocity discontinuity is

$$dS = 2\pi r \sin \alpha dr \quad (3.243)$$

Inserting into Eq. (3.235)

$$\dot{W}_{s3} = \frac{-2\pi}{\sqrt{3}} \sigma_{f0} \dot{u} r_i^2 \frac{1}{(1 - (r_i/r_0)^2)} (\cot \alpha \ln(r_0/r_i)) \quad (3.244)$$

The high ambient pressure should also be taken into consideration in the power calculations. The pressure in backward can extrusion is assumed to be applied from the annular cross section of the system to overcome the defect formation. This power can be calculated as:

$$\dot{W}_e = \pi(r_0^2 - r_i^2) v_f p \quad (3.245)$$

When the value of  $v_f$  is replaced the external power will be

$$\dot{W}_e = \pi r_i^2 \dot{u} p \quad (3.246)$$

The power to overcome the inertia is equal to

$$\dot{W}_k = \frac{1}{2} \frac{\rho}{g} \dot{V} v^2 \quad (3.247)$$

Where

$$v = -\dot{u} \frac{1}{1 - (r_0/r_i)^2} \quad (3.248)$$

$$\dot{V} = \pi(r_0^2 - r_i^2) v \quad (3.249)$$

The inertia term will be equal to

$$\dot{W}_k = \frac{\pi \rho \dot{u}^3 r_i^2}{2g(1 - (r_0/r_i)^2)^2} \quad (3.250)$$

The total power term will be equal to

$$P_T = \dot{W}_i + \dot{W}_s + \dot{W}_f + \dot{W}_e + \dot{W}_k \quad (3.251)$$

The ram power will be equal to

$$\dot{W}_e = \pi r_i^2 \dot{u} p_R \quad (3.252)$$

When the power terms are added and normalized with  $\pi r_i^2 \dot{u} \sigma_{f0}$  the result will be equal to:

$$p_r = \frac{2}{\sqrt{3}} \frac{1}{1 - (r_i/r_0)^2} \left\{ \sqrt{3} f(\alpha) \ln(r_0/r_i) + \frac{\alpha}{\sin^2 \alpha} - \cot \alpha + \right. \\ \left. + (\cot \alpha) \ln(r_0/r_i) + m \left[ \frac{h}{r_i} + \frac{r_i}{r_0} \left[ \frac{b_0}{r_i} + \left( \frac{r_0}{r_i} - 1 \right) \cot \alpha \right] \right] \right\} \quad (3.253)$$

### 3.3.2.2 Three Zone Velocity Field with Thick-Walled Solution

In the early stage of the process, a zone which does not experience any deformation is present. This result in a new velocity field definition, which is proposed by, Hoogenboom (2002), a dead zone, has to be introduced in addition to the previous three zones (Figure 3.14).

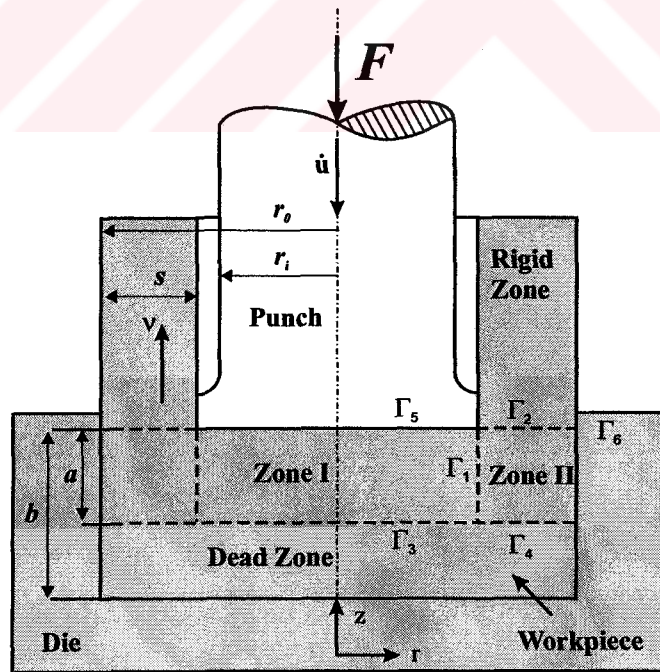


Figure 3.12 Three-Zone Velocity Field For Early Stage

In the late stage (end of stroke) of the process (Figure 3.6), the region that lies under the punch is assumed to be upsetted axially between the punch and the die bottom (Zone I), and the region that is between the first zone and the die is assumed to be upsetted radially between the punch and the die wall (Zone II). Finally the third zone is assumed to go through rigid body motion. These three zones are separated by two shear planes (surface velocity discontinuities),  $\Gamma_1$  and  $\Gamma_2$ . There also exist four friction planes which are denoted as  $\Gamma_3$ ,  $\Gamma_4$ ,  $\Gamma_5$ , and  $\Gamma_6$ .

In the early stage of the process, there exists an additional zone which is assumed to be undeformed. Zone I and zone II are deforming and the third zone experiences rigid body motion as in the late stage. The addition of dead zone to the model, adds new shear planes to the system. There are two new shear planes between zone I and the dead zone ( $\Gamma_3$ ) and zone II and the dead zone ( $\Gamma_4$ ). The friction planes are denoted as  $\Gamma_5$ ,  $\Gamma_6$ , and  $\Gamma_7$ . The upper bound solution for this kind of velocity field will be examined in the remaining parts of this section.

The necessary modification for the shear power components which are due to the new discontinuity surfaces are calculated as

$$P_{\Gamma_{dead-zone}} = \int_0^{r_i} \frac{\sigma_{f0}}{\sqrt{3}} |\dot{u}_{rI}| 2\pi r dr + \int_{r_i}^{r_i+s} \frac{\sigma_{f0}}{\sqrt{3}} |\dot{u}_{rII}| 2\pi r_i dr \quad (3.254)$$

$$P_{\Gamma_{dead-zone}} = \frac{\sigma_{f0}}{\sqrt{3}} \int_0^{r_i} \frac{r}{2b} \dot{u} 2\pi r dr + \frac{\sigma_{f0}}{\sqrt{3}} \int_{r_i}^{r_i+s} \frac{r_i^2}{2s(2r_i+s)} \frac{\dot{u}}{b} \left( -r + \frac{(r_i+s)^2}{r} \right) 2\pi r dr \quad (3.255)$$

$$P_{\Gamma_{dead-zone}} = \frac{\sigma_{f0} \dot{u} \pi}{\sqrt{3} b} \int_0^{r_i} r^2 dr + \frac{\sigma_{f0} \pi r_i^2}{s(2r_i+s)} \frac{\dot{u}}{b} \int_{r_i}^{r_i+s} \left( -r^2 + (r_i+s)^2 \right) dr \quad (3.256)$$

When we integrate the terms

$$P_{\Gamma dead-zone} = \frac{\sigma_{f0} \dot{u} \pi}{\sqrt{3} b} \left[ \frac{r^3}{3} \right]_0^{r_i} + \frac{\sigma_{f0} \pi r_i^2}{s(2r_i + s) b} \dot{u} \left[ \left( \frac{-r^3}{3} + r(r_i + s)^2 \right) \right]_{r_i}^{r_i+s} \quad (3.257)$$

When we insert the limits of the integral

$$P_{\Gamma dead-zone} = \frac{\sigma_{f0} \dot{u} \pi r_i^2}{3\sqrt{3} b} + \frac{\sigma_{f0} \pi r_i^2}{s(2r_i + s) b} \dot{u} \left[ \left( \frac{2(r_i + s)^2}{3} \right) + \left( \frac{r_i^2}{3} \right) - (r_i + s)^2 r_i \right] \quad (3.258)$$

Simplifying Eq. (3.258)

$$P_{\Gamma dead-zone} = \frac{\sigma_{f0} \dot{u} \pi r_i^2}{3\sqrt{3} b} + \frac{\sigma_{f0} \pi r_i^2}{s(2r_i + s) b} \dot{u} \left[ \frac{s^2(2s + 3r_i)}{3} \right] \quad (3.259)$$

The friction term for the late solution also has to be modified, since the factor two in the friction term for zone I, is now unnecessary. The friction plane is converted into a shear plane for the early solution.

$$P_{\Gamma 5} = \int_0^{r_i} \frac{m\sigma_{f0}}{\sqrt{3}} |\dot{u}_r| 2\pi r dr \quad (3.260)$$

$$P_{\Gamma 5} = \frac{m\sigma_{f0}}{\sqrt{3}} \int_0^{r_i} \frac{r}{2b} \dot{u} 2\pi r dr \quad (3.261)$$

Factoring out the constant terms

$$P_{\Gamma 5} = \frac{m\sigma_{f0} \dot{u} \pi}{\sqrt{3} b} \int_0^{r_i} r^2 dr \quad (3.262)$$

Integrating with respect to  $r$

$$P_{\Gamma 5} = \frac{m\sigma_{f0} \dot{u} \pi r_i^2}{3\sqrt{3} b} \quad (3.263)$$

The total power term will be:

$$\begin{aligned}
P_{T(early)} = & \sigma_{f0} \dot{\mu} \pi r_i^2 + \sqrt{\frac{2}{3}} \sigma_{f0} \dot{\mu} \pi r_i^2 \left\{ \left[ \left( \frac{(r_i + s)^2}{s r_i^2 (2r_i + s)} \zeta_3 \right) - \frac{(r_i + s)^2}{s(2r_i + s)} \operatorname{atanh} \left( \frac{r_i^2}{\zeta_3} \right) \right] \right. \\
& - \left[ \left( \frac{1}{s(2r_i + s)} \zeta_4 \right) - \frac{(r_i + s)^2}{s(2r_i + s)} \operatorname{atanh} \left( \frac{(r_i + s)^2}{\zeta_4} \right) \right] + \frac{1}{\sqrt{3}} \frac{b}{s} \sigma_{f0} \dot{\mu} \pi r_i \left[ \frac{r_i^2}{s(2r_i + s)} + 1 \right] \\
& + \frac{m \sigma_{f0} \dot{\mu} \pi r_i}{\sqrt{3}} \frac{b}{s} \left[ \frac{r_i^2}{s(2r_i + s)} + 1 \right] + \frac{\sigma_{f0}}{\sqrt{3}} \frac{\dot{\mu} \pi r_i^2}{s b (2r_i + s)} \left[ \frac{s^2 (2s + 3r_i)}{3} \right] \\
& + \frac{m \sigma_{f0} \dot{\mu} \pi r_i^2}{3\sqrt{3}} \frac{r_i}{b} + \frac{\sigma_{f0} \dot{\mu} \pi r_i^2}{3\sqrt{3}} \frac{r_i}{b} + \frac{\sigma_{f0} \dot{\mu} \pi r_i^2}{s b (2r_i + s)} \left[ \frac{s^2 (2s + 3r_i)}{3} \right]
\end{aligned} \tag{3.264}$$

The total power can be expressed non-dimensional simply by dividing the term into

$$P_{T(early)} = \frac{P_{T(early)}}{\sigma_{f0} \dot{\mu} \pi r_i^2} \tag{3.265}$$

$$\begin{aligned}
P_{T(early)} = & 1 + \sqrt{\frac{2}{3}} \left\{ \left[ \left( \frac{(r_i + s)^2}{s r_i^2 (2r_i + s)} \zeta_3 \right) - \frac{(r_i + s)^2}{s(2r_i + s)} \operatorname{atanh} \left( \frac{r_i^2}{\zeta_3} \right) \right] \right. \\
& - \left[ \left( \frac{1}{s(2r_i + s)} \zeta_4 \right) - \frac{(r_i + s)^2}{s(2r_i + s)} \operatorname{atanh} \left( \frac{(r_i + s)^2}{\zeta_4} \right) \right] \left. \right\} \\
& + \frac{m+1}{\sqrt{3}} \frac{b}{s} \left[ \frac{(r_i + s)^2}{r_i (2r_i + s)} \right] + \frac{1}{\sqrt{3}} \frac{1}{s b (2r_i + s)} \left[ \frac{s^2 (2s + 3r_i)}{3} \right] \\
& + \frac{m+1}{3\sqrt{3}} \frac{r_i}{b} + \frac{1}{\sqrt{3}} \frac{1}{s b (2r_i + s)} \left[ \frac{s^2 (2s + 3r_i)}{3} \right]
\end{aligned} \tag{3.266}$$

The non deformed zone that lies under the punch can be divided into two sections. The height of these two sections can be denoted as  $b$  and  $a$  which can be seen in the Figure 3.14. The parameter  $b$  is replaced by  $a$  and the total power term will be found by the author as:

$$p_{T(early)} = 1 + \sqrt{\frac{2}{3}} \left\{ \left[ \left( \frac{(r_i + s)^2}{sr_i^2(2r_i + s)} \zeta_3 \right) - \frac{(r_i + s)^2}{s(2r_i + s)} \operatorname{atanh} \left( \frac{r_i^2}{\zeta_3} \right) \right] - \left[ \left( \frac{1}{s(2r_i + s)} \zeta_4 \right) - \frac{(r_i + s)^2}{s(2r_i + s)} \operatorname{atanh} \left( \frac{(r_i + s)^2}{\zeta_4} \right) \right] \right\} \quad (3.267)$$

$$+ \frac{m+1}{\sqrt{3}} \gamma \left[ \frac{(r_i + s)^2}{r_i(2r_i + s)} \right] + \frac{m+1}{3\sqrt{3}} \frac{r_i}{s} \frac{1}{\gamma} + \frac{2}{\sqrt{3}} \frac{1}{s^2(2r_i + s)} \left[ \frac{s^2(2s + 3r_i)}{3} \right] \frac{1}{\gamma}$$

where  $\gamma$  is a free parameter and equal to  $a/s$ .

In order to optimize the total power term with respect to  $\gamma$

$$\frac{\partial p_{T(early)}}{\partial \gamma} = 0 \quad (3.268)$$

$$\frac{\partial p_{T(early)}}{\partial \gamma} = \frac{m+1}{\sqrt{3}} \left[ \frac{(r_i + s)^2}{r_i(2r_i + s)} \right] \frac{m+1}{3\sqrt{3}} \frac{r_i}{s} \frac{1}{\gamma^2} - \frac{2}{\sqrt{3}} \frac{1}{s^2(2r_i + s)} \left[ \frac{s^2(2s + 3r_i)}{3} \right] \frac{1}{\gamma^2}$$

From the Eq. (3.268), the optimum value for  $\gamma$  is found by the author as:

$$\gamma = \sqrt{\frac{r_i^2(2r_i + s)}{3s(r_i + s)^2} + \frac{2r_i(2s + 3r_i)}{3(r_i + s)^2} \frac{1}{m+1}} \quad (3.269)$$

### 3.3.2.3 Three Zone Velocity Field with Thin-Walled Solution

The early solution differs from the late solution with the presence of new shear planes due to the presence of dead-zone (Figure 3.14). The modification of the friction and shear loss terms will make the equation applicable to early stage of backward can extrusion.

The additional shear term is formulated in Eq. (3.254)

$$P_{\Gamma dead-zone} = \int_0^{r_i} \frac{\sigma_{f0}}{\sqrt{3}} |\dot{u}_{rI}| 2\pi r dr + \int_{r_i}^{r_i+s} \frac{\sigma_{f0}}{\sqrt{3}} |\dot{u}_{rII}| 2\pi r_i dr \quad (3.270)$$

$$P_{\Gamma dead-zone} = \frac{\sigma_{f0}}{\sqrt{3}} \int_0^{r_i} \frac{r}{2b} \dot{u} 2\pi r dr + \frac{\sigma_{f0}}{\sqrt{3}} \int_{r_i}^{r_i+s} \frac{r_i}{2sb} (r_i + s - r) \dot{u} 2\pi r_i dr \quad (3.271)$$

Factoring out the constant terms

$$P_{\Gamma dead-zone} = \frac{\sigma_{f0} \dot{u} \pi}{\sqrt{3} b} \int_0^{r_i} r^2 dr + \frac{\sigma_{f0} \dot{u} \pi r_i^2}{\sqrt{3} sb} \int_{r_i}^{r_i+s} (r_i + s - r) dr \quad (3.272)$$

Integrating with respect to  $r$

$$P_{\Gamma dead-zone} = \frac{\sigma_{f0} \dot{u} \pi r_i^2}{3\sqrt{3}} \frac{r_i}{b} + \frac{\sigma_{f0} \dot{u} \pi r_i^2}{\sqrt{3}} \frac{s}{b} \quad (3.273)$$

The multiplication factor in the late solution in Eq. (3.125) is unnecessary for the early solution. Since the friction plane is converted into a shear plane for the early solution.



$$P_{\Gamma 5} = \int_0^{r_i} \frac{m\sigma_{f0}}{\sqrt{3}} |\dot{u}_{r1}| 2\pi r dr \quad (3.274)$$

$$P_{\Gamma 5} = \frac{m\sigma_{f0}}{\sqrt{3}} \int_0^{r_i} \frac{r}{2b} \dot{u} 2\pi r dr \quad (3.275)$$

Factoring out the constant terms

$$P_{\Gamma 5} = \frac{m\sigma_{f0}\dot{u}\pi}{\sqrt{3}b} \int_0^{r_i} r^2 dr \quad (3.276)$$

Integrating with respect to  $r$

$$P_{\Gamma 5} = \frac{m\sigma_{f0}\dot{u}\pi r_i^2}{3\sqrt{3}} \frac{r_i}{b} \quad (3.277)$$

As a result the total power term will turn out to be:

$$\begin{aligned} P_{T(early)} &= \sigma_{f0}\dot{u}\pi r_i^2 + \frac{2}{\sqrt{3}}\sigma_{f0}\dot{u}\pi r_i^2 + \frac{1}{\sqrt{3}}\sigma_{f0}\dot{u}\pi r_i^2 \frac{b}{s} \\ &+ \frac{1}{2\sqrt{3}}\sigma_{f0}\dot{u}\pi r_i^2 \frac{s}{b} + \frac{1}{\sqrt{3}}m\sigma_{f0}\dot{u}\pi r_i^2 \frac{s}{b} + \frac{1}{\sqrt{3}}m\sigma_{f0}\dot{u}\pi r_i^2 \frac{b}{s} \\ &+ \frac{1}{3\sqrt{3}}m\sigma_{f0}\dot{u}\pi r_i^2 \frac{r_i}{b} + \frac{1}{2\sqrt{3}}\sigma_{f0}\dot{u}\pi r_i^2 \frac{s}{b} + \frac{1}{3\sqrt{3}}\sigma_{f0}\dot{u}\pi r_i^2 \frac{r_i}{b} \end{aligned} \quad (3.278)$$

The total power can be expressed non-dimensional simply by dividing the term into

$$p_{T(early)} = \frac{P_{T(early)}}{\sigma_{f0} \dot{\epsilon} \pi r_i^2} \quad (3.279)$$

$$p_{T(early)} = 1 + \frac{2}{\sqrt{3}} + \frac{1}{\sqrt{3}} \frac{s}{b} + \frac{m+1}{2\sqrt{3}} \frac{b}{s} + \frac{m+1}{3\sqrt{3}} \frac{r_i}{b}$$

The non deformed zone that lies under the punch can be divided into two sections. The height of these two sections can be denoted as  $b$  and  $a$  which can be seen in the Figure 3.14. The parameter  $b$  is replaced by  $a$  and the total power term will be expressed as:

$$p_{T(early)} = 1 + \frac{2}{\sqrt{3}} + \frac{1}{\sqrt{3}} \frac{1}{\gamma} + \frac{m+1}{2\sqrt{3}} \gamma + \frac{m+1}{3\sqrt{3}} \frac{1}{\gamma} \frac{r_i}{s} \quad (3.280)$$

This solution can be optimized by taking a free-parameter  $\gamma$  which is equal to  $a/s$ . The optimization is done by taking the derivative of the total power term with respect to  $\gamma$

$$\frac{\partial p_{T(early)}}{\partial \gamma} = 0 \quad (3.281)$$

$$\frac{\partial p_{T(early)}}{\partial \gamma} = -\frac{1}{\sqrt{3}} \frac{1}{\gamma^2} + \frac{m+1}{2\sqrt{3}} - \frac{m+1}{3\sqrt{3}} \frac{1}{\gamma^2} \frac{r_i}{s} = 0$$

From the Eq. (3.281), the optimum value for  $\gamma$  will be

$$\gamma = \sqrt{\frac{2}{m+1} + \frac{2}{3} \frac{r_i}{s}} \quad (3.282)$$

The term  $\gamma$  result the minimum power for the solution proposed.

## CHAPTER 4

### FINITE ELEMENT METHOD

#### 4.1 Introduction

In this study for assessment and modification of results, a commercial finite element program MARC / Auto Forge is used to calculate the forming force. In this chapter, the theory of finite element and some parameters of the program will be explained. Later in the chapter, the finite element analysis results will be compared with experimental results available in the literature.

#### 4.2 Theoretical Background of the Finite Element Method

Regardless of the geometry, material and boundary conditions and type of the problem, finite element method follows a general well-defined step-by-step procedure (Tekkaya, 1999).

- The continuum is divided into a “finite number of ideal elements”. This is done by engineering judgment (Idealization).
- The numbers of infinite unknowns are reduced to a finite number. This is done by using shape functions (Discretization).
- After the first two steps, the relationship between the unknown displacements and known forces at the nodes are determined with the relationship (Determination of Element Properties). This relationship can be either a linear relationship as in Eq. (4.1) or a non-linear relationship as in Eq. (4.2).

$$\{F\} = [k]\{u\} \quad (4.1)$$

$$\{F\} = [k(u)]\{u\} \quad (4.2)$$

where  $F$  is force,  $k$  is the stiffness and  $u$  is the displacement field.

- Assembly of element stiffnesses to discretize the whole continuum
- Introduction of boundary conditions
- Solution of the system of equations
- Computation of strains and stresses

#### 4.2.1 Finite Element Approach for Large Plastic Deformation

The most important characteristic of metal forming processes is large strains and displacements. This makes metal forming processes highly non-linear. The sources of nonlinearity in finite element analysis that result in Eq. (4.2) are (Tekkaya, 2001(a)):

- Material nonlinearity (flow of material in plastic region, large strains, which is very common for metal forming processes)
- Geometric nonlinearity (large rotation and displacement of the system with small strains, which is very common for metal forming processes)
- Contact nonlinearity (contact of workpiece with other workpieces or tools, due to friction)

There are two procedures for solving such problems (MARC/Auto Forge, 1998)

- Elastic-plastic approach
- Rigid-plastic approach

The finite element analysis of metal forming processes using the rigid-plastic material model is very popular due to the following properties of this method (Tekkaya, 2001(a)):

- The material does not require the consideration of the non-linear kinematics of the finite deformation. Hence it is less time consuming.
- Rigid-plastic formulations are numerically rather robust and reliable.
- In three-dimensional analysis it is possible to formulate linear mixed tetrahedral elements, which allow easy automatic meshing.
- The computer implementation of rigid-plastic finite element code is simple.

Beside these advantages of rigid-plastic formulations there are some serious drawbacks.

- Any elastic based property such as residual stresses and spring-back cannot be analyzed by means of the rigid-plastic material law, which neglects elastic strains.
- A more serious drawback is the fact that rigid-plastic models utilize a pseudo-elastic description of material regions, which are assumed to be rigid. This leads to the fact that, especially in cold forming processes, friction which is always present between the tools and the workpiece in elastic regions of the workpiece is not modeled correctly.
- Another drawback is that rigid-plastic materials cannot detect stress peaks, which occur at the transition between elastic and elasto-plastic material zones.
- Finally, if net shape forming processes are analyzed, the accuracy requirements of the analysis cannot be fulfilled usually.

Due to the disadvantages of the rigid-plastic model stated above, for this study elastic-plastic model is used. This is especially due to the better friction modeling of elastic-plastic model for cold forming processes. Elastic-plastic model increases the accuracy of the formation in cold regions.

#### 4.2.2 Elastic-Plastic Solution by Updated Lagrangian Approach

In elastic-plastic method, the equations of equilibrium are formulated by using updated Lagrangian method, while in the rigid-plastic procedure; the updated Eulerian method is used. The procedures are based upon the conventional Lagrangian and Eulerian methods, but the reference frame is updated at the end of each increment.

In order to obtain the formulations for updated Lagrangian Method, some formulations of total Lagrangian approach has to be used:

The equation of equilibrium is (Belytschko, 2000),

$$\frac{\partial \sigma_{ij}}{\partial x_j} + b_i = 0 \quad (4.3)$$

which is true for the body in the current or deformed configuration where  $\sigma$  is the Cauchy or true stress tensor and  $b$  will be described as body forces. Small letters ( $x, v, s$ ) refer to the deformed configuration where capital letters ( $X, V, S$ ) will refer to the undeformed configuration. The equilibrium equations are the strong form of the principle of virtual work. The integration is done with respect to deformed configuration.

$$\int_V \sigma_{ij} \cdot \frac{\partial \delta u}{\partial x_j} \cdot dv = \int_V b_i \cdot \delta u \cdot dv + \int_S t_i \cdot \delta u \cdot ds \quad (4.4)$$

The Jacobian of the deformation can be defined as:

$$J = \frac{dv}{dV} = \det \left( \frac{\partial x}{\partial X} \right) = \det(F) \quad (4.5)$$

Introducing the symmetric second Piola-Kirchoff stress tensor,  $S_{ij}$

$$J \cdot \sigma_{ij} = F_{ij}^T \cdot S_{ij} \cdot F_{ij} \quad (4.6)$$

The Green-Lagrangian strain tensor is the work conjugate to the second Piola-Kirchoff stress tensor

$$E_{ij} = \frac{1}{2} \left( F_{ij}^T \cdot F_{ij} - I \right) \quad \text{or} \quad (4.7)$$

The variation in the Green-Lagrangian strain tensor comes

$$\delta E_{ij} = \frac{1}{2} \left( F_{mi} \frac{\partial \delta u_m}{\partial X_j} + \frac{\partial \delta u_m}{\partial X_i} F_{mj} \right) \quad (4.8)$$

This result in a principle of virtual work integrated over the undeformed volume

$$\int_V S^T \cdot \delta E_{ij} \cdot dV = \int_V B_i \cdot \delta u \cdot dV + \int_S T_i \cdot \delta u \cdot dS \quad (4.9)$$

When Eq. (4.9) is differentiated with respect to time, the rate of virtual work will be found as:

$$\int_V \left[ \dot{S}_{ij} \cdot \delta E_{ij} + S_{ij} \cdot \frac{\partial v_k}{\partial X_i} \cdot \frac{\partial \delta u_k}{\partial X_j} \right] dV = \int_V \dot{B}_i \cdot \delta u_i \cdot dV + \int_S \dot{T}_i \cdot \delta u_i \cdot dS \quad (4.10)$$

In the updated Lagrangian approach, the element stiffness is assembled in the current configuration of the body. The updated Lagrangian approach can be used to analyze structures where inelastic behavior causes the large deformations such as those encountered in metal forming. The Lagrangian coordinate frame has little physical significance in these analyses since the inelastic deformations are, by definition, permanent in the body. For these analyses, the Lagrangian frame of reference is redefined at the beginning of each increment (MARC/Auto Forge, 1998).

Although it is possible to derive theoretical constitutive equations of the type given in Eq. (4.10) for most materials, it is often more suitable to specify the equations with reference to the current state. The desired formulation can be obtained by taking Eq. (4.10) to the reference state as current state. It follows that momentarily

$$F_{ij} = \delta_{ij} \quad , \quad \delta E_{ij} = \delta D_{ij} \quad , \quad \frac{\partial}{\partial X_i} = \frac{\partial}{\partial x_i} \quad , \quad S_{ij} = \sigma_{ij} \quad (4.11)$$

where  $F$  is the deformation gradient tensor and  $D$  is the rate of deformation tensor, and therefore, Eq. (4.10) transforms into

$$\int_V \left[ \dot{\sigma}_{ij}^T \cdot \delta D_{ij} + \sigma_{ij} \cdot \frac{\partial v_k}{\partial x_i} \cdot \frac{\partial \delta u_k}{\partial x_j} \right] dv = \int_V \dot{b}_i \cdot \delta u_i \cdot dv + \int_S \dot{t}_i \cdot \delta u_i \cdot ds \quad (4.12)$$

In this equation,  $\dot{\sigma}_{ij}^T$  is the Truesdell rate of Cauchy stress tensor which can be obtained from the usual material rate of Cauchy stress tensor by differentiation as

$$\dot{\sigma}_{ij} = J^{-1} F_{ik} \dot{S}_{kl} F_{jl} + J^{-1} \dot{F}_{ik} S_{kl} F_{jl} + J^{-1} F_{ik} S_{kl} \dot{F}_{jl} - j J^{-2} F_{ik} S_{kl} F_{jl} \quad (4.13)$$



If one converts the state to current and reference state, it follows that

$$\dot{\sigma}_{ij} = \dot{\sigma}_{ij}^T + \frac{\partial v_i}{\partial x_k} \cdot \sigma_{kj} + \sigma_{ik} \cdot \frac{\partial v_j}{\partial x_k} - \sigma_{ij} \cdot \frac{\partial v_k}{\partial x_k} \quad (4.14)$$

The Truesdell rate of Cauchy stress is materially objective. That is, if rigid rotation is imposed on the material, the Truesdell rate vanishes, whereas the usual material rate does not vanish. The constitutive equations may well be formulated in terms of the Truesdell rate of Cauchy stress tensor. It may be written as

$$\dot{\sigma}_{ij}^T = L_{ijkl} (\sigma_{mn}) D_{kl} \quad (4.15)$$

The moduli  $L_{ijkl}$  are not equal to classical elastic-plastic moduli

$$L_{ijkl}^{e-p} = 2G \cdot \left[ \delta_{ik} \cdot \delta_{jl} + \frac{\lambda}{2G} \cdot \delta_{ij} \cdot \delta_{kl} - \frac{3}{2} \cdot \frac{\sigma'_{ij} \cdot \sigma'_{kl}}{\sigma_o^2} \right] \quad (4.16)$$

These moduli supply the relation between the Jaumann rate of Cauchy stress tensor and the deformation rate

$$\dot{\sigma}_{ij}^J = L_{ijkl}^{e-p} D_{kl} \quad (4.17)$$

The Jaumann rate of Cauchy stress tensor is related to the material rate of Cauchy stress tensor with the equation

$$\dot{\sigma}_{ij}^J = \dot{\sigma}_{ij} - \omega_{ik} \cdot \sigma_{kj} - \sigma_{ik} \cdot \omega_{jk} \quad (4.18)$$

where the spin tensor  $\omega_{ij}$  is defined by

$$\omega_{ij} = \frac{1}{2} \left( \frac{\partial v_i}{\partial x_j} - \frac{\partial v_j}{\partial x_i} \right) \quad (4.19)$$

The Jaumann rate of Cauchy stress is the rate of change of the Cauchy stress in a corotational system. The material rate of Cauchy stress can be eliminated from Eq. (4.18) with the use of Eq. (4.19), which yields the relation

$$\dot{\sigma}_{ij}^T = \dot{\sigma}_{ij}^J - D_{ik} \cdot \sigma_{kj} - \sigma_{ik} \cdot D_{kj} + \sigma_{ij} \cdot D_{kk} \quad (4.20)$$

Thus the relation between the large strain moduli and the classical elastic-plastic moduli is

$$L_{ijkl} = L_{ijkl}^{e-p} - \delta_{il} \cdot \sigma_{kj} - \sigma_{il} \cdot \delta_{kj} + \sigma_{ij} \cdot \delta_{kl} \quad (4.21)$$

Note that the last term in Eq. (4.21) does not satisfy the usual symmetry relation. This is not relevant for material plasticity problems since the deformations are approximately incompressible. Hence, Eq. (4.21) may be approximated by

$$L_{ijkl} = L_{ijkl}^{e-p} - \delta_{il} \cdot \sigma_{kj} - \sigma_{il} \cdot \delta_{kj} \quad (4.22)$$

Spatial discretization leads to the overall non-linear stiffness equations of the form

$$[K\{U\}] \cdot \{\Delta U\} = \{\Delta F\} \quad (4.48)$$

### 4.2.3 Numerical Solution of Equations

Metal forming equations are severely nonlinear due to geometric, contact and material nonlinearities. The numerical methods are used for the solution of these equations. The numerical methods that are used for solving these equations are Euler method, self correcting Euler method, direct iteration method, the Newton-Raphson method, modified Newton-Raphson method, quasi Newton-Raphson method and

BFGS. In MARC/Auto Forge, Newton-Raphson method is used as the numerical solver. (Figure (4.4))

#### 4.2.3.1 Newton-Raphson Method

The nonlinear force equation Eq. (4.2) can be reduced to Eq. (4.24) by Taylor series expansion for Newton-Raphson method. (Tekkaya, 2001(a))

$$[k_i \{U^{i-1}\}] \cdot \{\Delta U^i\} = \{R \{U^{i-1}\}\} \quad (4.24)$$

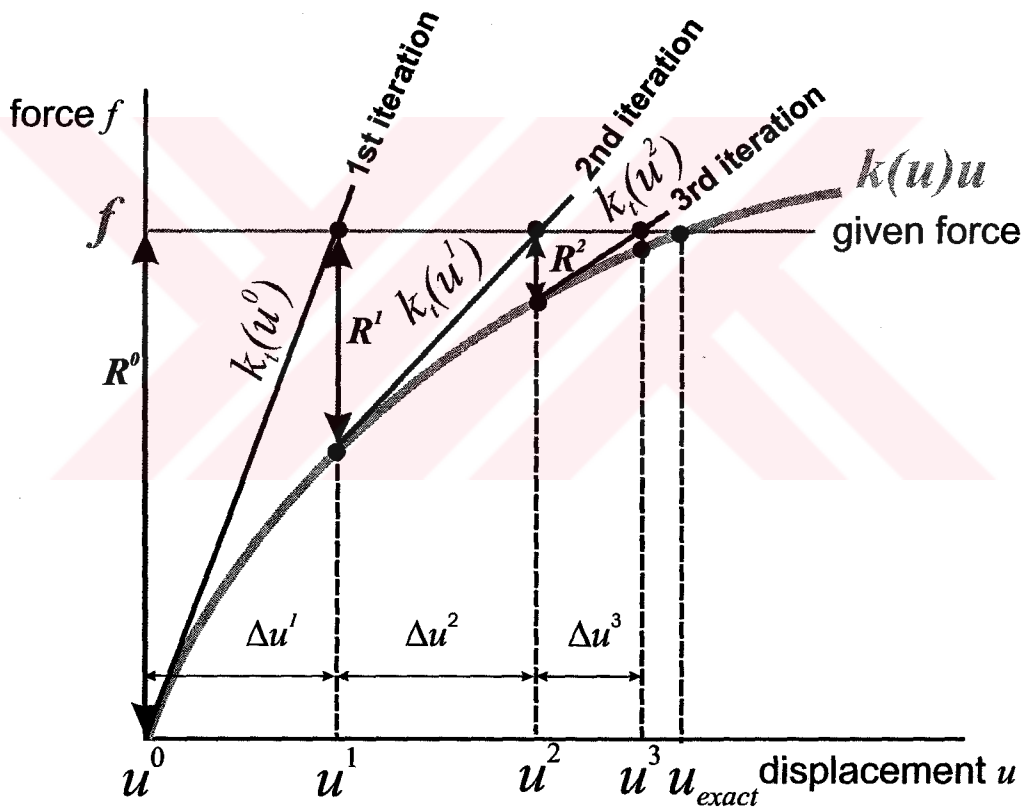


Figure 4.1 Newton-Raphson Method (Tekkaya, 2001(a))

The full Newton-Raphson method has quadratic convergence properties. This means that, in subsequent iteration, the relative error decreases quadratically. The Newton-Raphson method provides good results for nonlinear system. Stability of the numerical solution with Newton-Raphson method is dependent on the initial guess. If initial guess is not good there exists a possibility of divergence of the solution (MARC/Auto Forge, 1998).

#### 4.2.3.2 Convergence Limits

The default procedure for convergence criterion in the finite element program MARC-Autoforge is based on the magnitude of the maximum residual load to the maximum reaction force (MARC/Auto Forge, 1998). This method is appropriate since the residuals measure the out-of-equilibrium force, which should be minimized. This technique is also appropriate for Newton-Raphson method, where zero load iterations reduce residual load. The method is:

$$\frac{\|F_{residual}\|_{\infty}}{\|F_{resident}\|_{\infty}} < TOL_1 \quad (4.25)$$

$$\|F_{residual}\|_{\infty} < TOL_1 \quad (4.26)$$

$F$  is the force vector, and  $TOL_1$  is the control tolerances.  $\|F\|_{\infty}$  shows the component of  $F$  with the highest absolute value. The two procedures are absolute and relative residual checking procedures are available in MARC/AutoForge. The relative residual checking is formulated in Eq. (4.25), where  $F_{residual}$  corresponds to R value shown in Figure 4.1. The absolute residual checking is formulated in Eq. (4.26), where  $F_{resident}$  is the total force applied:

$$\frac{\|\delta u\|_{\infty}}{\|du\|_{\infty}} < TOL_1 \quad (4.27)$$

$$\|\delta u\|_{\infty} < TOL_1 \quad (4.28)$$

where  $d_u$  is the displacement increment vector,  $\delta_u$  is the displacement iteration vector. Convergence is satisfied if the maximum displacement of the last iteration compared to the actual displacement change of the increment is small than tolerance value for relative convergence check Eq. (4.27), and for absolute check Eq. (4.28) is valid.

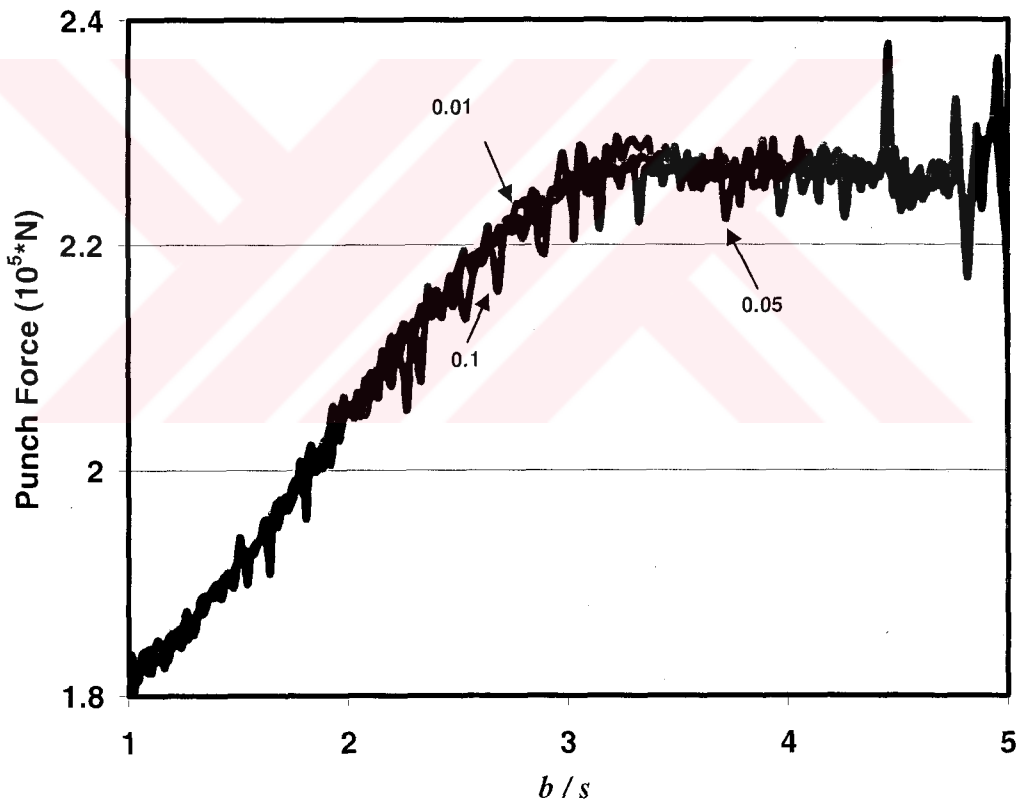


**Figure 4.2** Convergence Study

The value of the convergence criterion has an effect on the quality of the solution. When the convergence criterion is tighter, the solution maybe improved. The

problem with convergence criteria is that as the amount of allowable error decreases the time for simulations increase. The user has to make a clear assessment whether the result obtained from the simulation worth the time spend. In figure 4.2, the results are for no friction and 60% area reduction is shown for different residual force convergence criteria. As seen in Figure 4.5, all the results are similar for different convergence values. The curve for 0.1 has more deviations compared to other two solutions. The results for 0.05 and 0.01 are nearly the same whereas the time spend for 0.01 is double the time necessary for 0.05. Therefore for this process 0.05 seems to be a reasonable value for convergence.

### **4.3 Finite Element Model of Backward Can Extrusion**

The modeling of the process is very critical in FEA. The assumptions, the geometry and boundary conditions have to be set properly and clearly, otherwise the solution that is obtained can be irrelevant to the real case.

The backward can extrusion is an axis-symmetric process, which eases modeling and finite element solution. The independence of the process from the third coordinate axis  $\theta$ , allows the two-dimensional axis-symmetric solution of the problem.

#### **4.3.1 Geometry**

The process parameters and geometry has to be clarified before creating the model. As seen in Figure 4.3, the backward can extrusion process is symmetric with respect to z-axis, due this fact half of the geometry can be modeled for FEA instead of the full geometry.

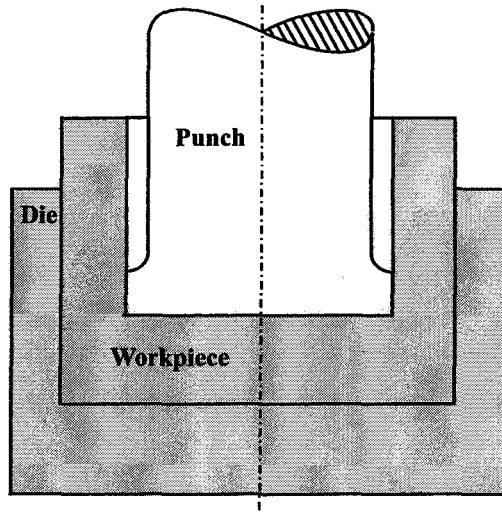


**Figure 4.3** Backward Can Extrusion 2-D Model

This will help to save time and computer space. As seen in Figure 4.4, the half of the geometry is modeled for FEA.

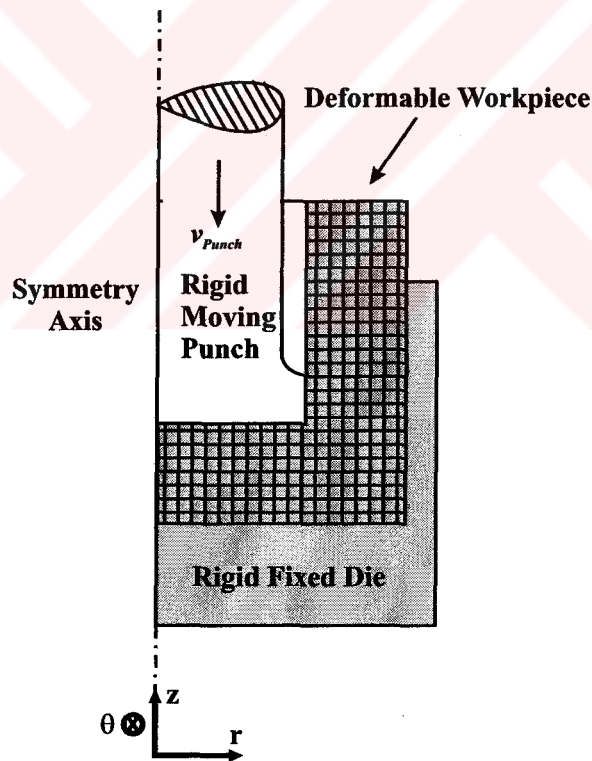


**Figure 4.4** Finite Element Model for Backward Can Extrusion

The punch for backward can extrusion process as it can be seen from Figure 4.4 has a punch land. This part of the punch prevents the deformed workpiece being in contact with the rest of the punch, hence reducing the friction power.

### 4.3.2 Boundary Conditions

The definition of boundary conditions is very critical for the construction of the finite element model. The misinterpretation of the boundary conditions can lead the faulty results. The boundary conditions for backward can extrusion are fairly simple. There are four main geometries that are created for the model. The two rigid bodies, the punch and the die are non-deformable bodies. The workpiece is meshed and defined as a deformable body (Figure 4.5). For surfaces  $A_1$ ,  $A_2$ ,  $A_3$  and  $A_4$  friction boundary condition is defined. The die is fixed and the punch moves with a certain velocity

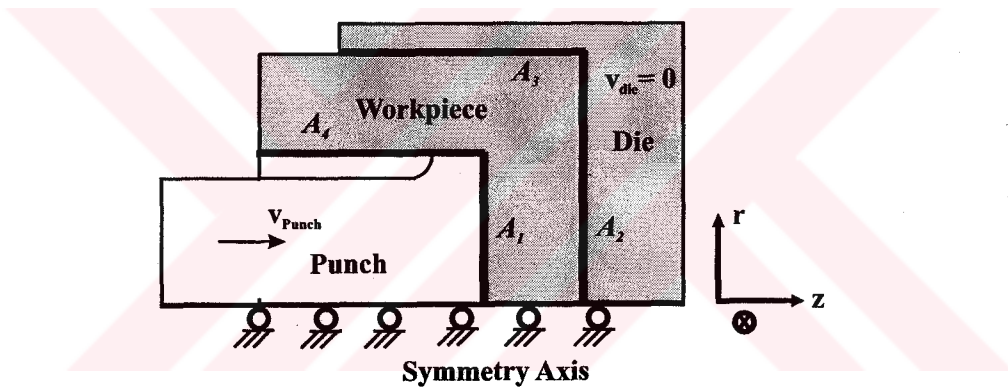


**Figure 4.5** Boundary Conditions for Finite Element Model

### 4.3.3 Material Properties

The analyses for backward can extrusion for comparison of the analytical models were done for two types of materials. The first type was non-hardening material with a constant flow curve (Figure 4.6). The value  $\sigma_{f0}$  is the initial flow stress of the material and does not change during the deformation. This approach is used in upper



bound formulations, as a results this model was necessary for the verification of the assumptions for the equations that are available in the literature.

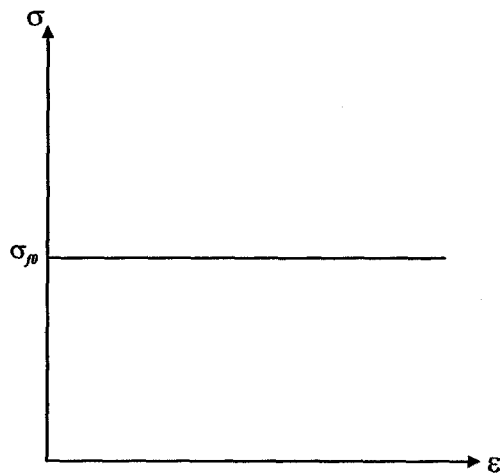


**Figure 4.6** Flow Curve for Non-Hardening Material

The second type of material was strain-hardening material, which are used in real life applications. Three kinds of elements were used for the simulations. The materials were chosen with respect to their hardening properties. The materials that were used in the simulations are assumed to be in harmony with the Ludwik's Power Law which is defined as:

$$\sigma_f = C\bar{\epsilon}^n \quad (4.29)$$

For Eq. (4.29), the value of  $n$  is critical since it determines the behavior of the curve. The flow curve for the materials used in the simulations is tabulated in Appendix B.

## 4.4 Convergence Study

### 4.4.1 Element Size

As the workpiece deforms, some of the elements in the mesh are highly distorted, due to this fact the geometry has to be remeshed. The dimensions of the elements in

the remeshed body are controlled by a parameter called as “maximum element edge length” which defines the average length of one side of the element. Smaller element size results in smoother curves and easy convergence but the time required for the solution increases.

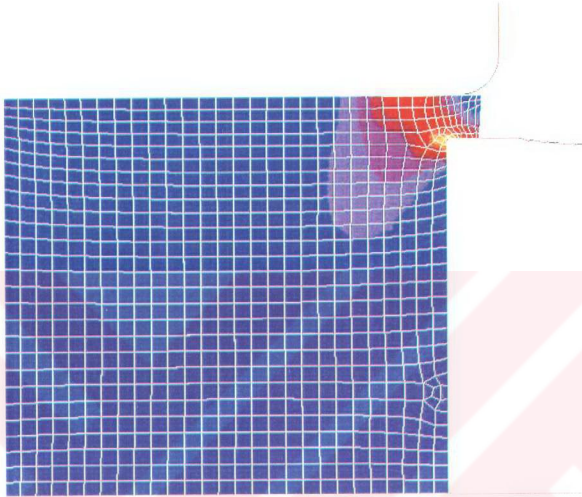


**Figure 4.7** Convergence Problems

If the element edge length is kept too large then problems as show in Figure 4.7 can be faced for the case of backward can extrusion, as the area reduction increases, annular gap between the die and punch decreases. This results in the necessity of very small element edge lengths for the model

In Figure 4.7, the solution for 80% is reduction without friction, the solution failed to converge for element edge length of 0.4 mm. Since the most drastic deformation takes place in 80% area reduction. For a realistic comparison of finite element results, simulation have to be done for parameters that makes the solution for 80%

area reduction possible. Even though for lower area reductions, such as 40%, the solution can converge for 0.4 maximum element edge lengths, they also have to be simulated with the parameters for 80% area reduction.

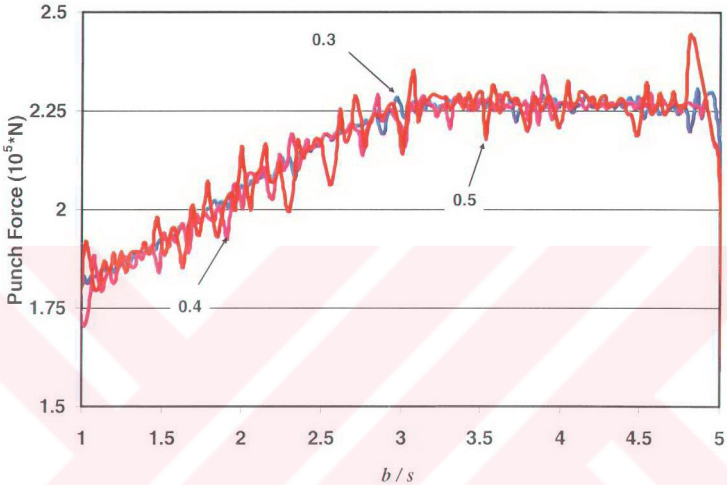


Figure 4.8 Effect of Maximum Element Edge Length

Finite element is a numerical solution, so its quality highly depends on the number of elements in the model, which also affects the number of nodes. As the number of elements increase, the quality of the results improves. This improvement has a certain limit. The number of elements varies due to the maximum element edge length and the severity of the deformation. After a certain value of maximum element edge length, no matter how minimal the edge length is, the results are hardly affected. This specific value of element edge length has to be determined for a limiting case for the available geometries. As it can be seen in Figure 4.8, for 60% area reduction, the punch force displacement curve is affected by the size of the maximum element edge length. When the number of elements is not sufficient or the

shape of the elements is too much distorted, the geometry has to be remeshed for convergence. These continuous remeshing results in such an oscillating curve. This becomes a more serious problem as the area reduction increases. In order to obtain converging solution and a smooth curve, the maximum element edge length for remeshing has to be set to a reasonable value.

#### 4.4.2 Friction Model

In contact problems, often neutral lines develop which means that along a contact surface, the material flows in one direction in a part of the surface, and in the other direction in another part (Figure 4.9). The discontinuous behavior of  $\sigma_{fr}$  curve can cause numerical difficulties. This discontinuous curve has to be smoothed to overcome these problems that may arise during simulations.

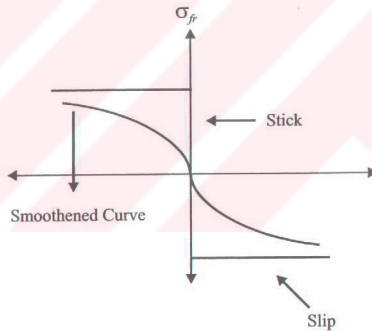


Figure 4.9 Smoothing of the curve

The shear model obeys the formulation

$$\sigma_{fr} \leq -m \frac{\sigma_f}{\sqrt{3}} \quad (4.55)$$

The friction model for the backward can extrusion proves is selected as shear model due to the fact that all most of the analytical models are upper bound solutions and they use shear friction model.

#### 4.5 Verification of Finite Element Model with Experimental Results

The finite element analysis results are considered to be the real values throughout this study. Although it has been accepted in literature that FEA results supply correct results, this assumption should be verified. The only mean to verify these solutions is to check the results with experimental data. The experimental data used in this study are from Schmitt (1968). Schmitt has performed a wide range of experiments with backward can extrusion in his Ph.D. thesis.

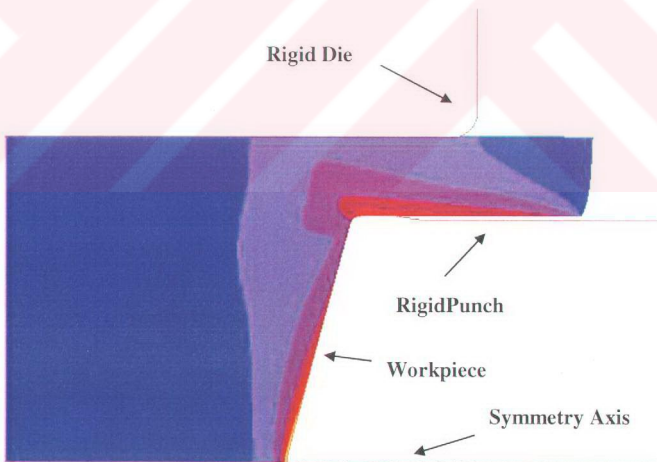


Figure 4.10 Finite Element Model of the punch used by Schmitt (1968)

The punch geometry that is used by Schmitt is different than the punch geometry used in this study. For comparison of FEA data with experimental data a new punch is created according to the geometry given in his work. The geometry of the punch is given in Appendix D. The finite element model of the punch used by Schmitt can be seen in Figure 4.10.

The finite element model has been compared with the experimental results that are obtained by Schmitt for Mbk6. The flow curve for Mbk6 can be found in Appendix B.

The most important problem in the comparison of finite element and experimental data is the friction. According to Schmitt, the friction factor between the contacting bodies in backward can extrusion is about 0.04 for Coulomb model. As a rough estimate, this value corresponds to 0.08 for shear model for friction. The geometry of the punch that is used for the simulations can be seen in Table 4.1

**Table 4.1** Dimensions of the Initial Billet

$b_0/d_0$	$b_0$ (mm)
0.37	11.1
0.67	20.1
1.07	32.1

The problem with these kinds of comparisons is that the friction factor is never definitely known. Only a rough estimate can be done according to theoretical and practical knowledge.

The results that are obtained from finite element analysis are similar to the experimental results. The general behavior of the punch force-displacement curve is obtained in the simulations. The initial billet diameter is 30 mm and the comparison for 16% area reduction can be seen in Figure 4.11-4.13 for different initial billet lengths.

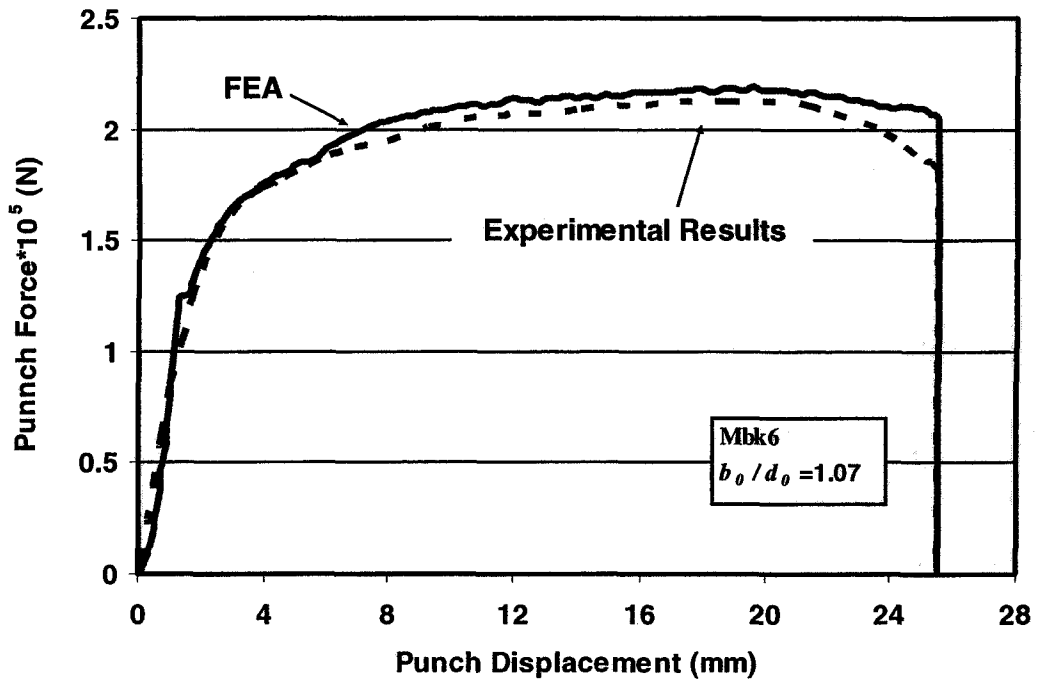


Figure 4.11 Comparison of Experimental Data with FEA for 16% Area Reduction ( $b_0/d_0=1.07$ )

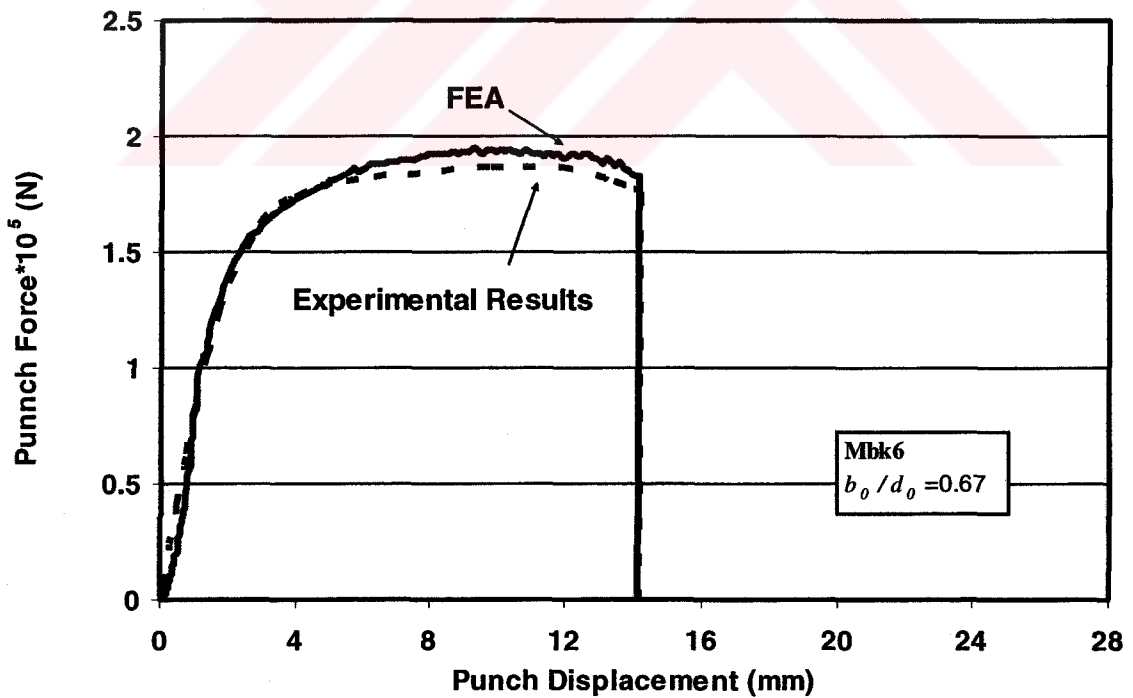
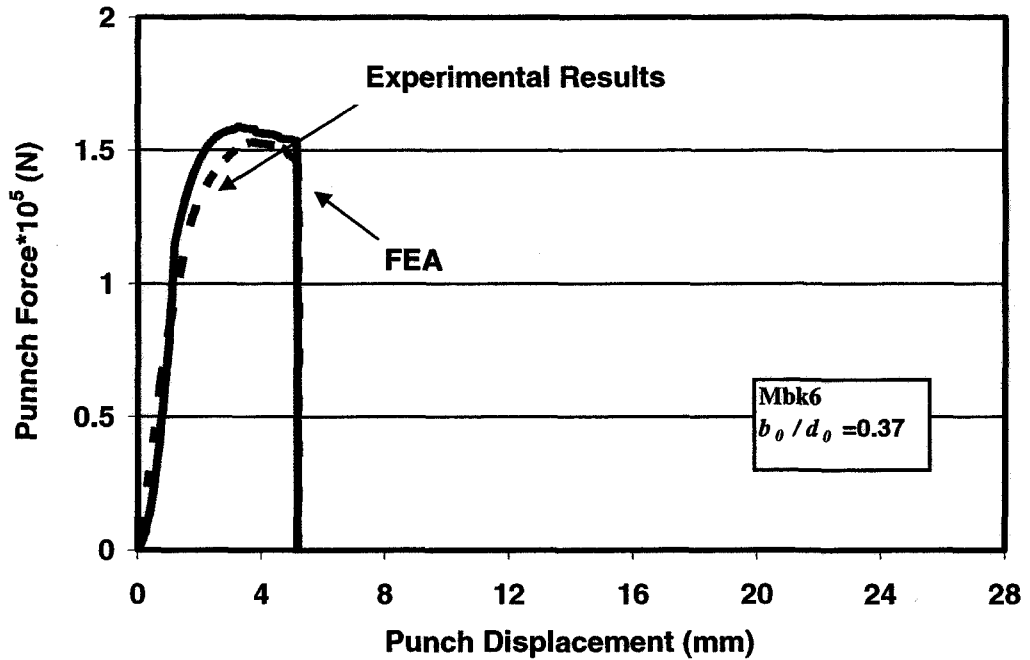


Figure 4.12 Comparison of Experimental Data with FEA for 16% Area Reduction ( $b_0/d_0=0.67$ )



**Figure 4.13** Comparison of Experimental Data with FEA for 16% Area Reduction ( $b_0/d_0=0.37$ )

The comparison for 57% area reduction can be seen in Figure 4.14-4.16 for different initial billet lengths. In Figure 4.14, there is an increase in the punch force in the experimental results which cannot be obtained by FEA. This can be due to increase of friction due to lack of lubrication to the end of the process.



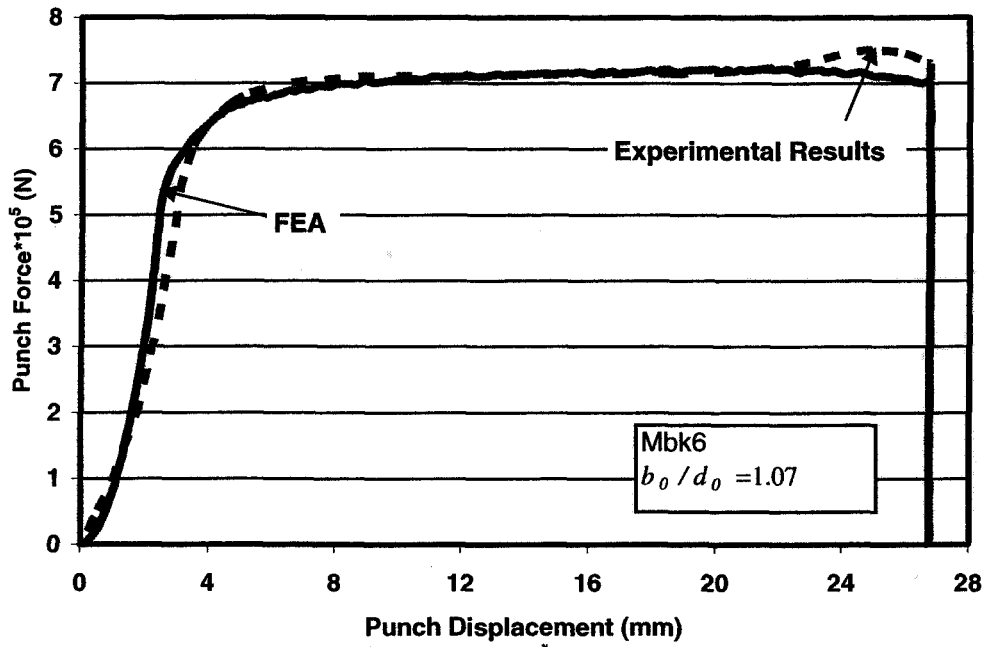


Figure 4.14 Comparison of Experimental Data with FEA for 57% Area Reduction ( $b_0/d_0=1.07$ )

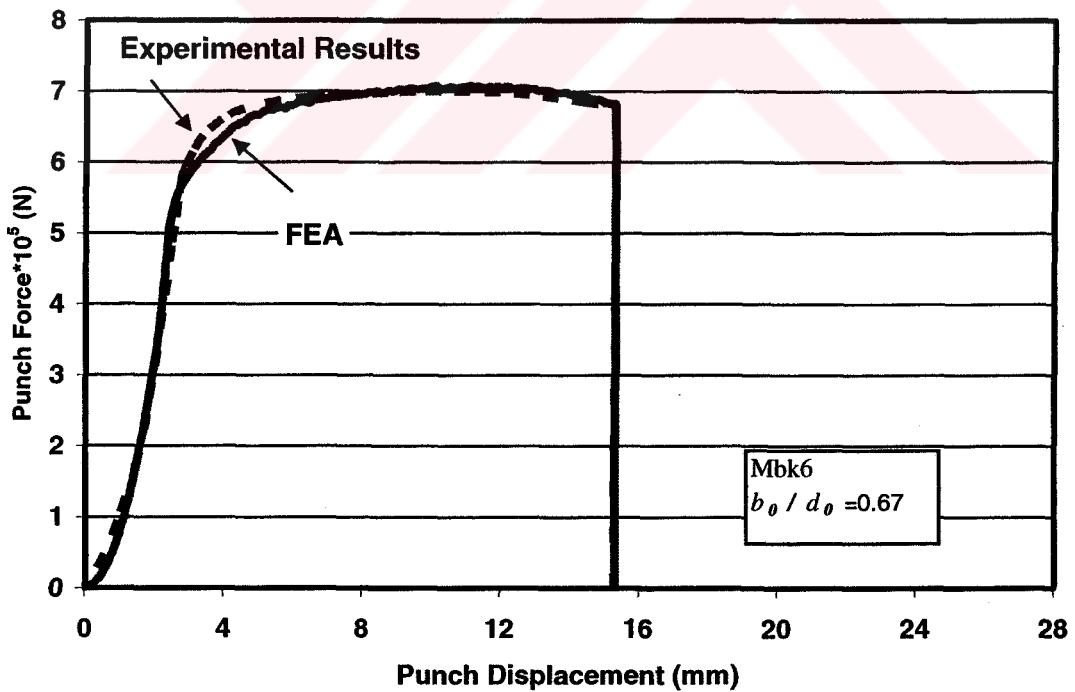
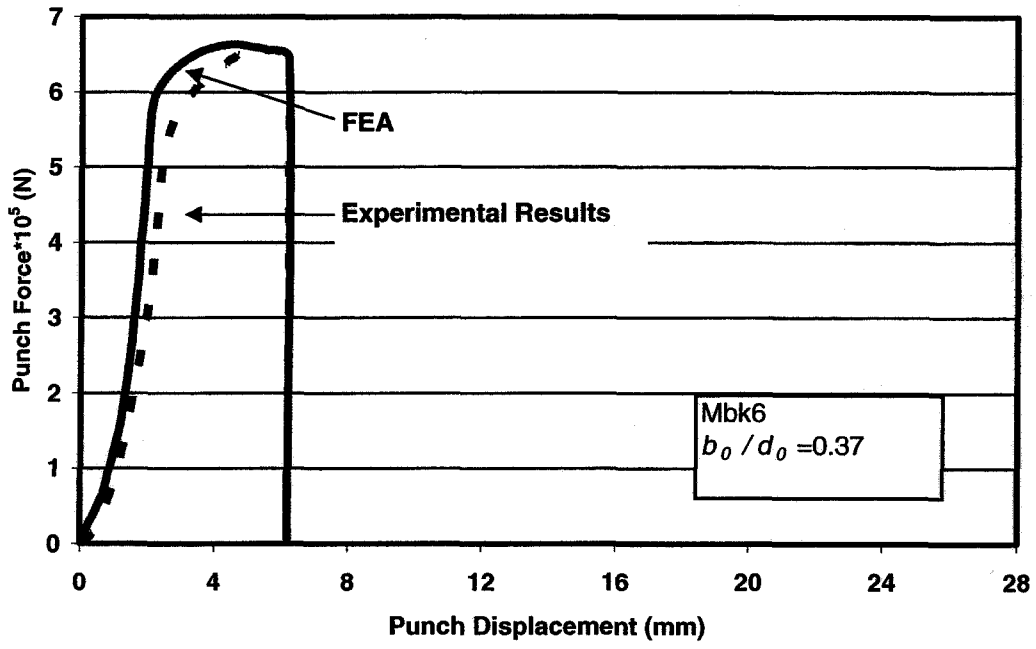


Figure 4.15 Comparison of Experimental Data with FEA for 57% Area Reduction ( $b_0/d_0=0.67$ )



**Figure 4.16** Comparison of Experimental Data with FEA for 57% Area Reduction ( $b_0/d_0=0.37$ )

## **CHAPTER 5**

### **ASSESSMENT OF ANALYTICAL EQUATIONS FOR NON-HARDENING MATERIALS**

#### **5.1 Introduction**

The formulations that have been analyzed in Chapter 3 have advantages and drawbacks due to the assumptions they introduce. The quality of these results has to be examined and compared with the real life values.

In this chapter, the results of the elementary solutions and upper bound solutions are assessed with the aid of finite element results since the results obtained from finite element are very close to the real life values. The assessment will be done by non-hardening materials, and later in Chapter 6 this study will be extended to hardening materials. The effect of friction factor, punch geometry, and initial billet shape will also be examined in this chapter.

#### **5.2 Modification of Dipper's Solution**

In the formulation of the upper bound solutions, it is assumed that the material is non-hardening and that the shear model for friction is valid. Due to this fact, as stated in Chapter 4, the finite element simulations are performed applying the shear model. On the contrary Dipper's solution includes the effect of hardening and uses Coulomb's model for friction. This is due to the fact that Dipper used the elementary

plasticity method for the formulation of the punch force. As a result of this, Dipper's solution has to be modified in order to compare it with finite element results. Coulomb's friction model states that the friction coefficient between zone I and zone II is 0.5 according to Tresca, due to the fact that the material experiences shear on surface of velocity discontinuity  $\Gamma_1$ .

$$\mu = \frac{1}{2}(\mu_1 + 0.5) \quad (5.1)$$

The friction factor is equal to 1 for shear model. When the friction model is changed from Coulomb model to shear model, Eq. (5.1) can be modified as:

$$m = \frac{1}{2}(m_1 + 1) \quad (5.2)$$

In order to find the relationship between the two friction models, the shear stresses for friction can be equated.

$$\tau_{friction} = mk \quad (5.3)$$

$$\tau_{friction} = \mu\sigma_n \quad (5.4)$$

Dipper, as an assumption, equated the normal stress to flow stress, which results in:

$$\tau_{friction} = \mu\sigma_f \quad (5.5)$$

The relationship between the flow stress and the maximum possible shear stress for friction (yield stress) is defined by Tresca as:

$$k = \frac{\sigma_f}{2} \quad (5.6)$$

Inserting Eq. (5.6) to Eq. (5.3) and equating Eq. (5.3) and Eq. (5.5) will give the relationship between  $m$  and  $\mu$ .

$$\mu\sigma_f = m\frac{\sigma_f}{2} \quad (5.7)$$

$$\mu = \frac{m}{2} \quad (5.8)$$

The equilibrium equations, Eq. (3.3) in Chapter 3, should be modified by replacing the friction coefficient with the friction factor.

$$[-\sigma_{z,2} + (\sigma_{z,2} + d\sigma_{z,2})]\pi(r_0^2 - r_i^2) = m\sigma_{f2}(r_i + s/2)2\pi dz \quad (5.9)$$

$$s d\sigma_{z,2} = m\sigma_{f2} dz \quad (5.10)$$

Integrating the terms with the boundary condition  $\sigma_{z,2} = 0$  at  $z = b$  will result

$$\sigma_{z,2} = \frac{m\sigma_{f2}}{s}(b - z) \quad (5.11)$$

The average normal stress can be calculated for zone II with the average area  $A_2$

$$A_2 = 2r_{av}\pi b = 2\left(r_i + \frac{s}{2}\right)\pi b \quad (5.12)$$

The mean stress in  $z$ -direction for zone II can be found as

$$\sigma_{z,2,m} = \frac{\int_0^b \sigma_{z,2} dA}{A_2} = \frac{\int_0^b \frac{m\sigma_{f2}}{s}(b - z)2\left(r_i + \frac{s}{2}\right)\pi dz}{2\left(r_i + \frac{s}{2}\right)\pi b} \quad (5.13)$$

$$\sigma_{z,2,m} = \frac{\frac{2m\sigma_{f2}}{s} \left( r_i + \frac{s}{2} \right) \pi \int_0^b (b-z) dz}{2 \left( r_i + \frac{s}{2} \right) \pi b} = \frac{m\sigma_{f2}}{sb} \int_0^b (b-z) dz \quad (5.14)$$

$$\sigma_{z,2,m} = \frac{m\sigma_{f2}}{2sb} \left[ (2bz - z^2) \right]_0^b = \frac{m\sigma_{f2}}{2sb} (2b^2 - b^2) = \frac{m}{2} \sigma_{f2} \frac{b}{s} \quad (5.15)$$

According to the Tresca flow condition

$$\sigma_{r,2,m} = \sigma_{z,2,m} - \sigma_{f2} = -\sigma_{f2} \left( 1 + \frac{m b}{2 s} \right) \quad (5.16)$$

For Zone I, which goes through axial upsetting, the force equilibrium equation, Eq. (3.11) in Chapter 3 should be modified for shear friction,

$$\left[ -\sigma_{r,1} + (\sigma_{r,1} + d\sigma_{r,1}) \right] \pi r b = m_1 \sigma_{f,1} \pi r dz \quad (5.17)$$

$$d\sigma_{r,1} b = m_1 \sigma_{f,1} dr \quad (5.18)$$

Integrating the terms with the boundary condition  $\sigma_{r,1} = \sigma_{r,2,m}$  at  $r = r_i$ , the result will be

$$\sigma_{r,1} = \frac{m_1 \sigma_{f,1}}{2b} (r_i - r) + \sigma_{r,2,m} \quad (5.19)$$

The average radial stress over the area  $\pi r_i^2$  is given by

$$\sigma_{r,1,m} = -\frac{1}{6} m_1 \sigma_{f,1} \frac{2r_i}{b} + \sigma_{r,2,m} \quad (5.20)$$

When  $\sigma_{r,2,m}$  is substituted from the Eq. (3.9), the average radial stress will be

$$\sigma_{r,m} = \sigma_{r,1,m} + \sigma_{r,2,m} = -\frac{1}{6}m_1\sigma_{f1}\frac{r_i}{b} - \sigma_{f2}\left(1 + \frac{m}{2}\frac{b}{s}\right) \quad (5.21)$$

Applying the Tresca Flow condition, the axial stress on the punch is

$$\sigma_{z,m} = \sigma_{r,m} - \sigma_{f1} = -\sigma_{f1}\left(1 + \frac{1}{6}m_1\frac{r_i}{b}\right) - \sigma_{f2}\left(1 + \frac{m}{2}\frac{b}{s}\right) \quad (5.22)$$

Since the flow stress for non-hardening materials is constant and equal to  $\sigma_{f0}$ , Eq. (5.22) becomes

$$\sigma_{z,m} = \sigma_{r,m} - \sigma_{f1} = -\sigma_{f0}\left(1 + \frac{1}{6}m_1\frac{r_i}{b}\right) - \sigma_{f0}\left(1 + \frac{m}{2}\frac{b}{s}\right) \quad (5.23)$$

This modified formulation can be used to compare the solution by Dipper with other analytical formulations for non-hardening materials and shear model for friction.

### 5.3 The Comparison of Thick and Thin Walled Solutions for Three Zone Velocity Field

As analyzed in Chapter 3, there are two types of solution for three-zone velocity field. The general solution is named as thick-walled solution, where the wall thickness of the can is considered to be comparable with respect to the punch radius. In the simplified solution, which is named as the thin-walled solution, the wall thickness over punch radius ratio is much smaller than one and can be simplified when necessary. This manipulation result in a much simplified and compact formulation of the punch force. All assumptions result in some deviations from the real solution, due to this fact, the effect of thin-walled assumption should be examined.

In this section, the procedure of application of thin-walled assumption will be explained and the differences between the two solutions will be assessed.

The thin-walled assumption for three-zone velocity field modifies the strain rate definition for zone II. The internal deformation power and shear and friction loss terms are also effected by this change in strain definition.

As seen below the velocity in z-axis for zone II is calculated as:

$$\dot{u}_{zII} \pi \left[ (r_i + s)^2 - (r_i)^2 \right] = \dot{u}_{r(r=r_i)} 2\pi r_i z \quad (5.24)$$

$$\dot{u}_{zII} \pi \left[ (2r_i + s) s \right] = \dot{u}_{r(r=r_i)} 2\pi r_i z \quad (5.25)$$

When the value for the radial velocity in zone I is inserted to the Eq. (5.25), the velocity in z-direction for zone II will be equal to:

$$\dot{u}_{zII} = \frac{r_i^2}{s(2r_i + s)} \frac{\dot{u}}{b} z \quad (5.26)$$

But for thin-walled solution, since  $s/r_i \ll 1$

$$\dot{u}_{zII} \pi \left[ (2r_i + s) s \right] = \dot{u}_{r(r=r_i)} 2\pi r_i z \quad (5.27)$$

$$\dot{u}_{zII} 2\pi r_i s = \dot{u}_{r(r=r_i)} 2\pi r_i z \quad (5.28)$$

When the value for the radial velocity in zone I is inserted to the Eq. (5.28), the velocity in z-direction for zone II will be equal to:

$$\dot{u}_{zII} = \frac{r_i z}{2sb} \dot{u} \quad (5.29)$$



As it was explained in Chapter 3, this assumption is also applied to the solution after the calculation of the power terms by integration. Further simplification for thin-walled assumption is introduced after integration.

The calculation of deformation power for zone II is as follows:

$$P_{II} = \int_{r_i}^{r_i+s} \sigma_{f0} \dot{\epsilon}_{II} dV \quad (5.30)$$

When we insert the equivalent strain rate for zone II

$$P_{II} = \int_{r_i}^{r_i+s} \sigma_{f0} \frac{1}{\sqrt{3}} \frac{r_i}{sb} \dot{u} 2\pi r b dr \quad (5.31)$$

When we factor out the constant terms

$$P_{II} = \frac{2\pi r_i}{\sqrt{3}} \frac{\dot{u} \sigma_{f0}}{s} \int_{r_i}^{r_i+s} r dr \quad (5.32)$$

Integrating Eq. (5.32)

$$P_{II} = \frac{2\pi r_i}{\sqrt{3}} \frac{\dot{u} \sigma_{f0}}{s} \frac{(r_i + s)^2 - r_i^2}{2} \quad (5.33)$$

Simplifying Eq. (5.33)

$$P_{II} = \frac{2\pi r_i}{\sqrt{3}} \frac{\dot{u} \sigma_{f0}}{s} \frac{s(2r_i + s)}{2} \quad (5.34)$$

Due to the thin-walled assumption the wall thickness  $s$  is negligible

$$P_{II} = \frac{2\pi r_i}{\sqrt{3}} \dot{\sigma}_{f0} \frac{(2r_i + s^0)s}{2} \quad (5.35)$$

When simplified

$$P_{Ithin} = \frac{2\pi}{\sqrt{3}} r_i^2 \dot{\sigma}_{f0} \quad (5.36)$$

Where as the deformation power for zone II for thick walled solution calculated in Chapter 3 is:

$$P_{Ithick} = \sqrt{\frac{2}{3}} \pi r_i^2 \dot{\sigma}_{f0} \left\{ \left[ \left( \frac{(r_i + s)^2}{s r_i^2 (2r_i + s)} \zeta_3 \right) - \frac{(r_i + s)^2}{s(2r_i + s)} \operatorname{atanh} \left( \frac{r_i^2}{\zeta_3} \right) \right] \right. \\ \left. - \left[ \left( \frac{1}{s(2r_i + s)} \zeta_4 \right) - \frac{(r_i + s)^2}{s(2r_i + s)} \operatorname{atanh} \left( \frac{(r_i + s)^2}{\zeta_4} \right) \right] \right\} \quad (5.37)$$

Both of those terms should be non-dimensionalised by dividing them into  $\pi r_i^2 \dot{\sigma}_{f0}$ , which will result in,

$$P_{Ithin} = \frac{2}{\sqrt{3}} \quad (5.38)$$

Where as the deformation power for zone II for thick walled solution calculated in Chapter 3 is:

$$P_{IIthick} = \sqrt{\frac{2}{3}} \left\{ \left[ \left( \frac{(r_i + s)^2}{sr_i^2(2r_i + s)} \zeta_3 \right) - \frac{(r_i + s)^2}{s(2r_i + s)} \operatorname{atanh} \left( \frac{r_i^2}{\zeta_3} \right) \right] \right. \\ \left. - \left[ \left( \frac{1}{s(2r_i + s)} \zeta_4 \right) - \frac{(r_i + s)^2}{s(2r_i + s)} \operatorname{atanh} \left( \frac{(r_i + s)^2}{\zeta_4} \right) \right] \right\} \quad (5.39)$$

The comparison of these two solutions for different area reductions can be seen in Figure 5.1.

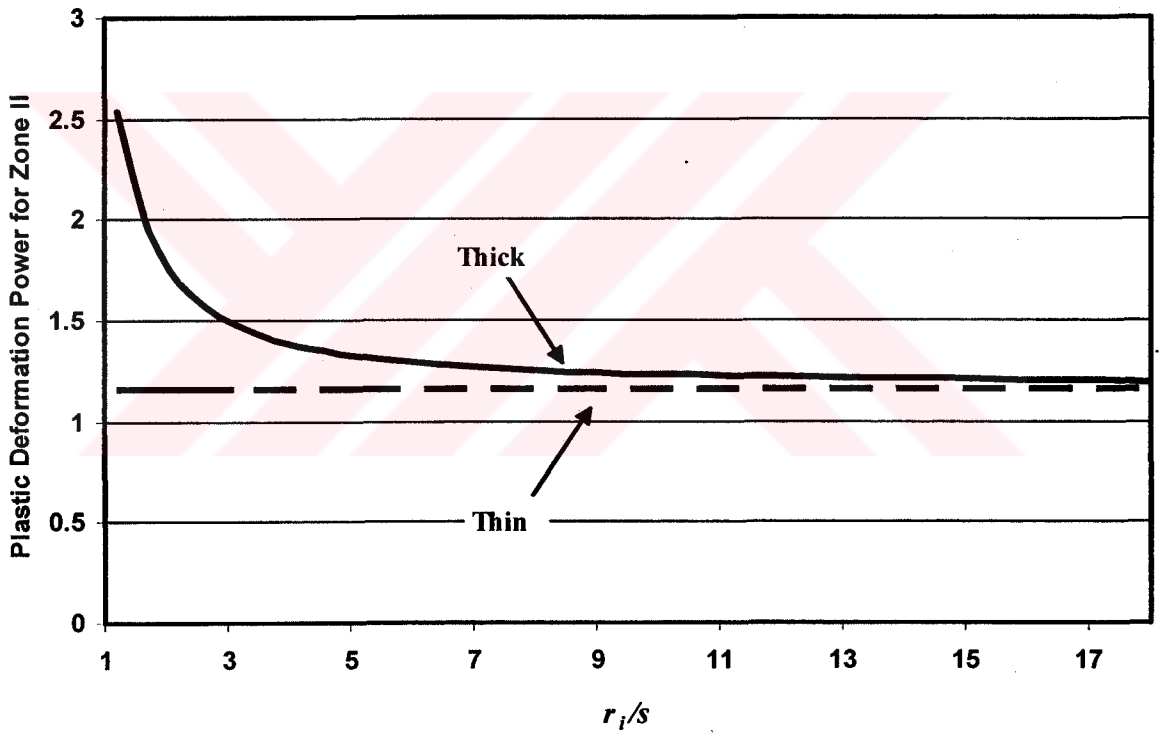


**Figure 5.1** Comparison of Deformation Power for Zone II

As it can be seen in Figure 5.1, as the  $r_i/s$  ratio increases (corresponds to increase in area reduction), the difference between the thin-walled and thick-walled solutions decrease.

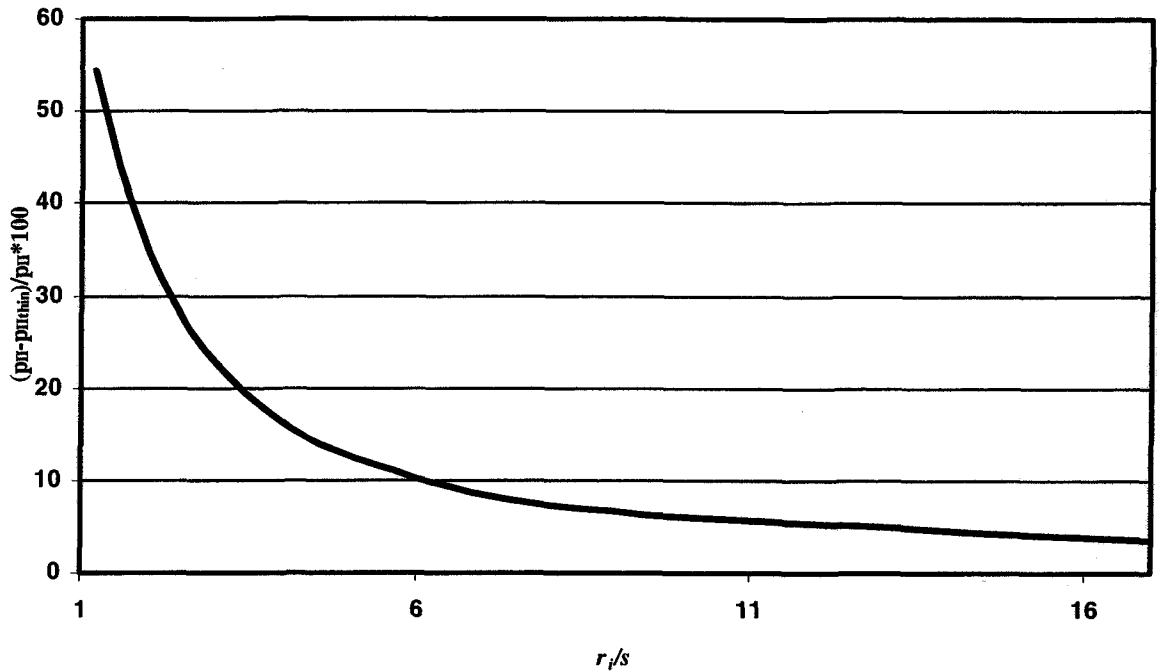


**Figure 5.2** Comparison of Deformation Power for Zone II

For very thin walled cans, the results are nearly equal. The difference between the solutions drops to less than 3% for high  $r_i/s$  values, as seen in Figure 5.2. As it can be seen in Figures 5.3-5.5, thin-walled solution has lower total power compared to thick-walled solution. Due to this fact, thin-walled three-zone velocity field solution is used in the comparison of the models available. The difference between the solutions decreases as the area reduction increases. This is due to the fact that as area reduction increases the thin-walled assumption is fulfilled.

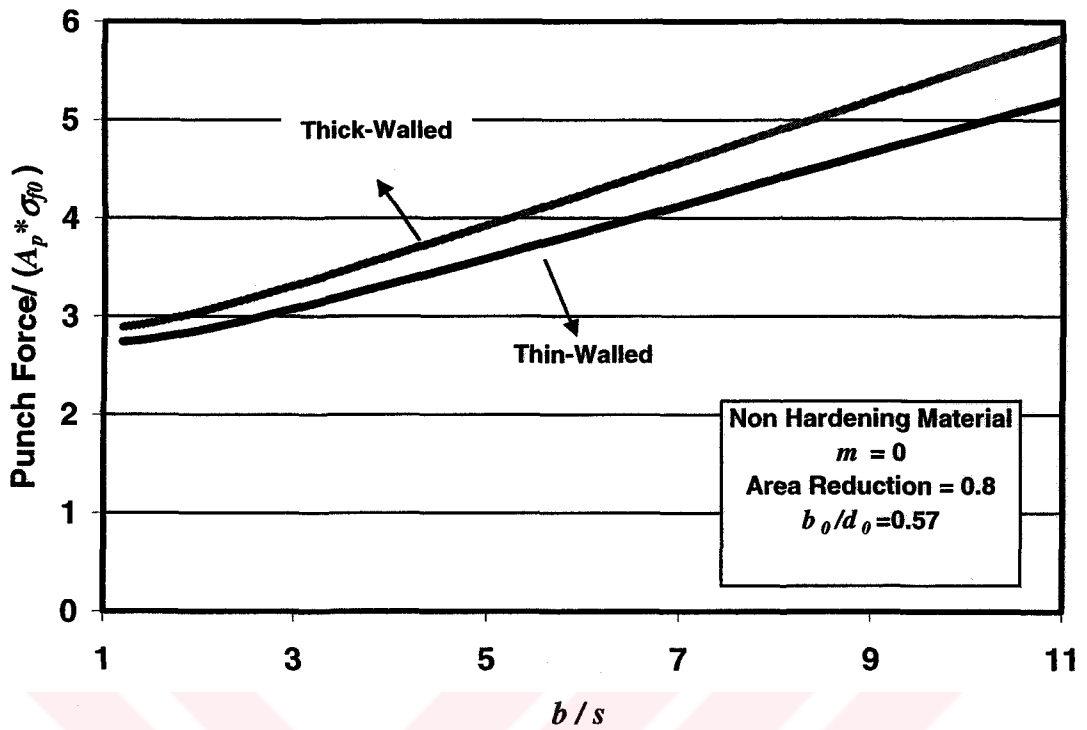


Figure 5.3 Comparison of Thin and Thick Walled Solutions for Three-Zone Velocity Field (80% Area Reduction)

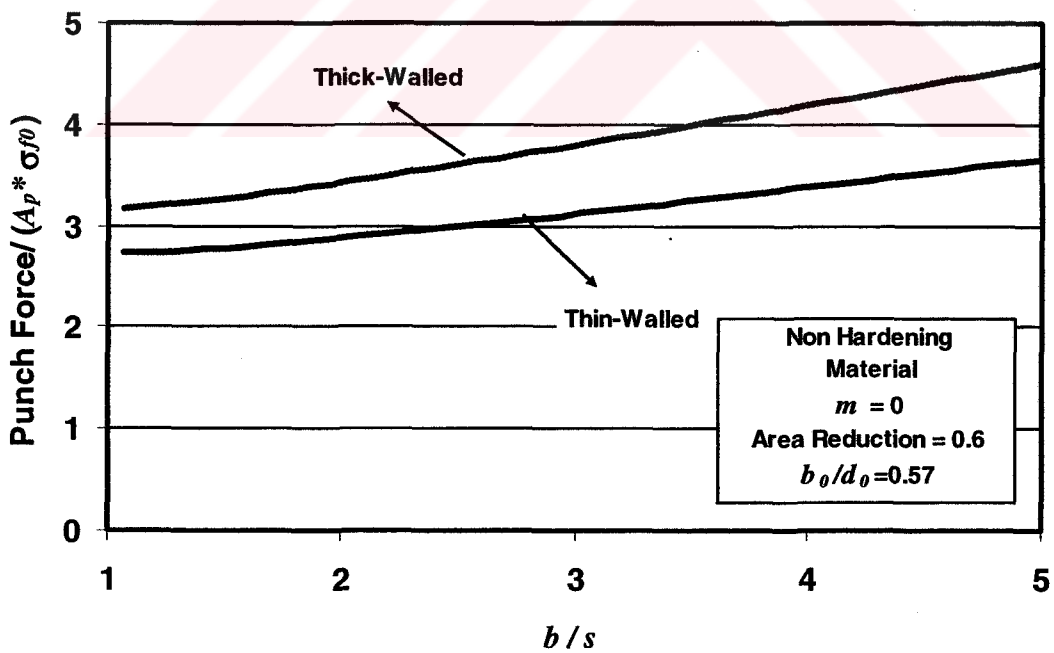
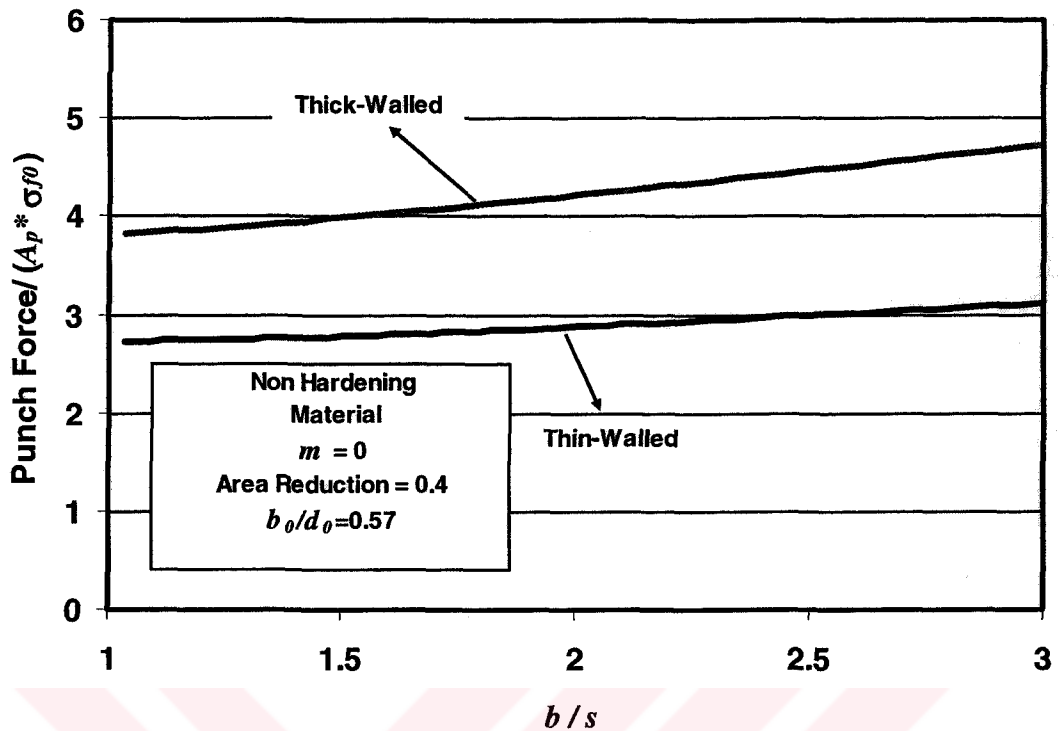


Figure 5.4 Comparison of Thin and Thick Walled Solutions for Three-Zone Velocity Field (60% Area Reduction)



**Figure 5.5** Comparison of Thin and Thick Walled Solutions for Three-Zone Velocity Field (40% Area Reduction)

For the results shown in Figures 5.3, 5.4 and 5.5, the friction factor is zero and the diameter is 20 mm and the initial billet length is equal to 11.4 mm which results in  $b_0/d_0$  ratio of 0.57. The three-zone velocity field solution is independent of the initial length of the billet, so a change in initial geometry of the billet will not affect the results for this formulation.

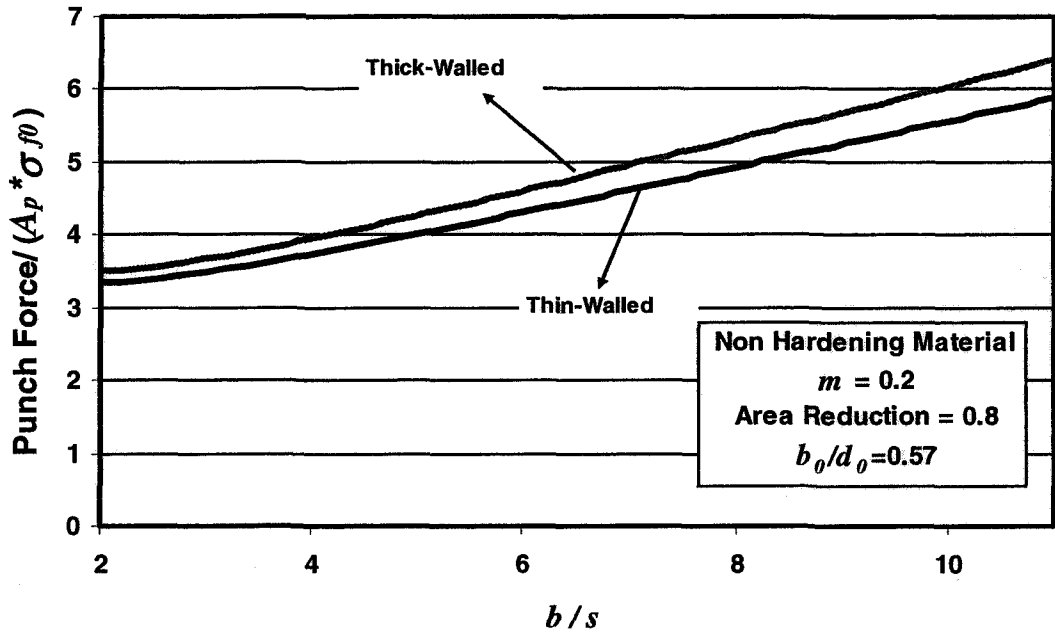


Figure 5.6 Comparison of Thin and Thick Walled Solutions for Three-Zone Velocity Field (80% Area Reduction)

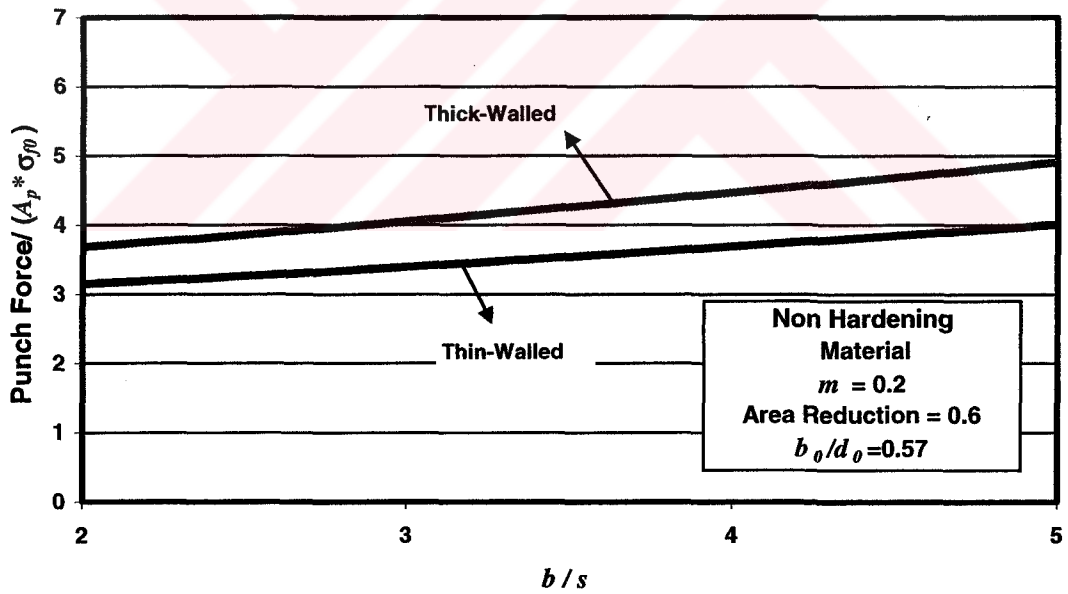
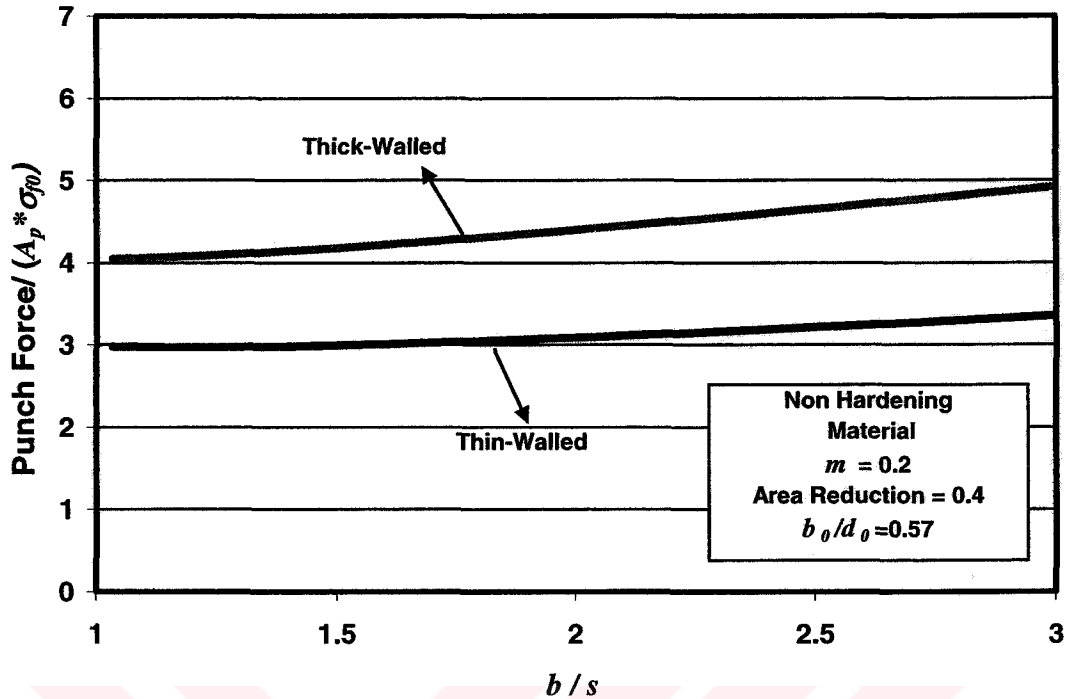


Figure 5.7 Comparison of Thin and Thick Walled Solutions for Three-Zone Velocity Field (60% Area Reduction)



**Figure 5.8** Comparison of Thin and Thick Walled Solutions for Three-Zone Velocity Field (40% Area Reduction)

#### 5.4 The Comparison of Analytical Equations with Finite Element Results

The total power terms that are analyzed in Chapter 3 are based on different assumptions and definitions. The quality of the results obtained from these formulations depends on the correctness of the assumptions, the amount of error introduced by these assumptions and the selection of the velocity field. In order to compare these analytical results, finite element analysis results are used. As explained in Chapter 4, the results supplied by finite element analysis are very close to real values for backward can extrusion.

In this chapter, the results for non-hardening materials will be examined. There are two main reasons for utilizing non-hardening materials. Firstly as stated in Chapter 2,



in upper bound method, it is assumed that the material is independent of strain hardening and strain rate. The flow stress for a non-hardening material is constant and independent of strain.

A parameter study to understand the effect of friction, punch shape, workpiece geometry has been done. In the first part of the analysis, the friction factor ( $m$ ) was set to zero in order to study the effect of internal deformation and shear terms for different area reductions. Later, the results are compared for friction factors of 0.1, 0.2 and 0.3.

The range of area reduction is from 40-80%, which covers the commonly used values in real life applications. The geometry of the workpiece is kept constant with  $b_0/d_0$  ratio being equal to 0.57. The effect of change of initial geometry is analyzed later in the chapter. The dimensions of the punch and the initial billet are given in Appendix D.

The process is divided into two stages due to the definitions of velocity fields as stated before. The data that is used to compare the solutions available in the literature are obtained from FEA. The material used for the simulations have a constant flow stress value, which is the characteristics of a non-hardening material.

#### **5.4.1 Comparison of Analytical Equations with FEA Results without Friction**

In the figures below, the results for the formulations that are analyzed in Chapter 3 can be seen along with finite element simulation data. The solutions that are named as “Hoogenboom Late” and “Hoogenboom Early” are the results for three-zone velocity field with thin-walled assumption. “Avitzur Early” is the spherical velocity field and “Avitzur Late” is the two-zone velocity field. The result for Dipper’s solution is obtained from the Eq. (5.23).

The finite element model that is used in this section is for a non-hardening material with  $b_0/d_0$  ratio of 0.57 and friction factor being equal to zero. In Figure 5.10, the total power for 40% area reduction can be seen as a function of can bottom thickness ( $b$ ) divided by can wall thickness ( $s$ ).

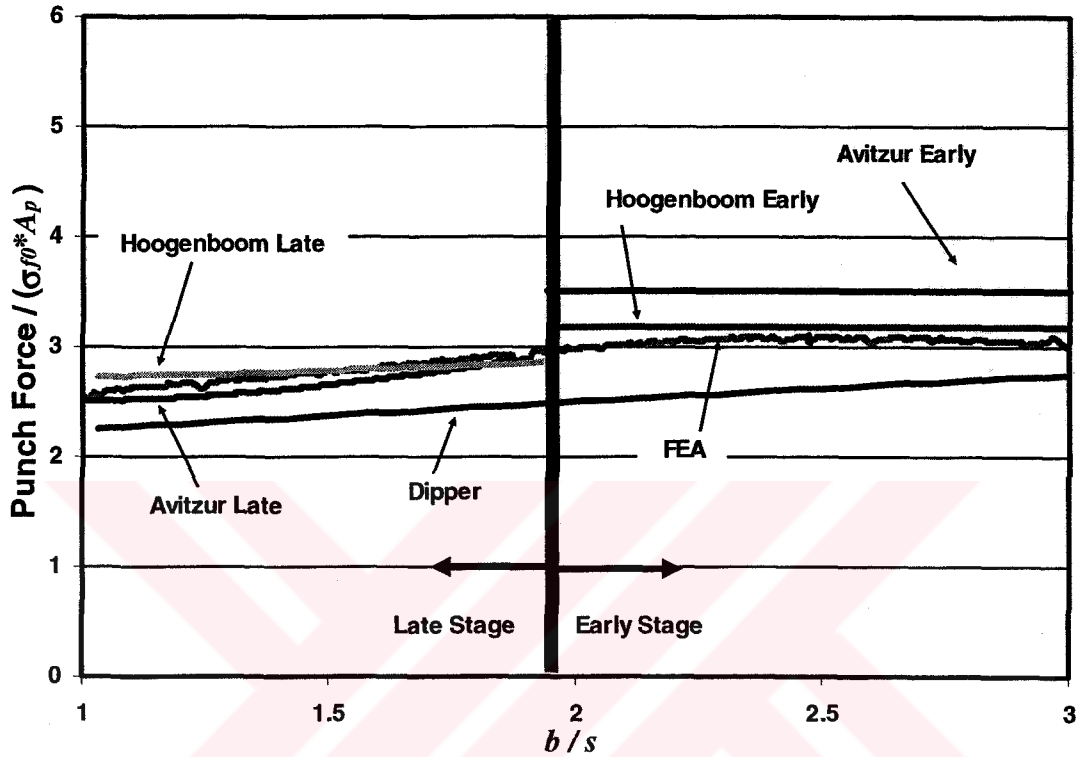


**Figure 5.9** Total Power Comparison for 40% Area Reduction

In Figure 5.9, the early solution by Hoogenboom gives very good results for the early stage of the process. The total forming force predicted by Hoogenboom's early stage solution is less than Avitzur's Early Stage solution. The reason for this can be based on the optimization done for this solution by Hoogenboom, as explained in 3.3.2.3. On the contrary in the late stage Avitzur's model supplies more consistent results. The solution by Avitzur, nearly gives exact result, matching the decreasing behavior of the punch force. Hoogenboom's late stage solution gives good results for low area reductions but the solution diverges from FEA results as the area reduction increases.

Dipper's solution is far below the finite element solutions. This is due to the fact that Dipper's solution is applicable to area reductions over 50% and hardening materials.

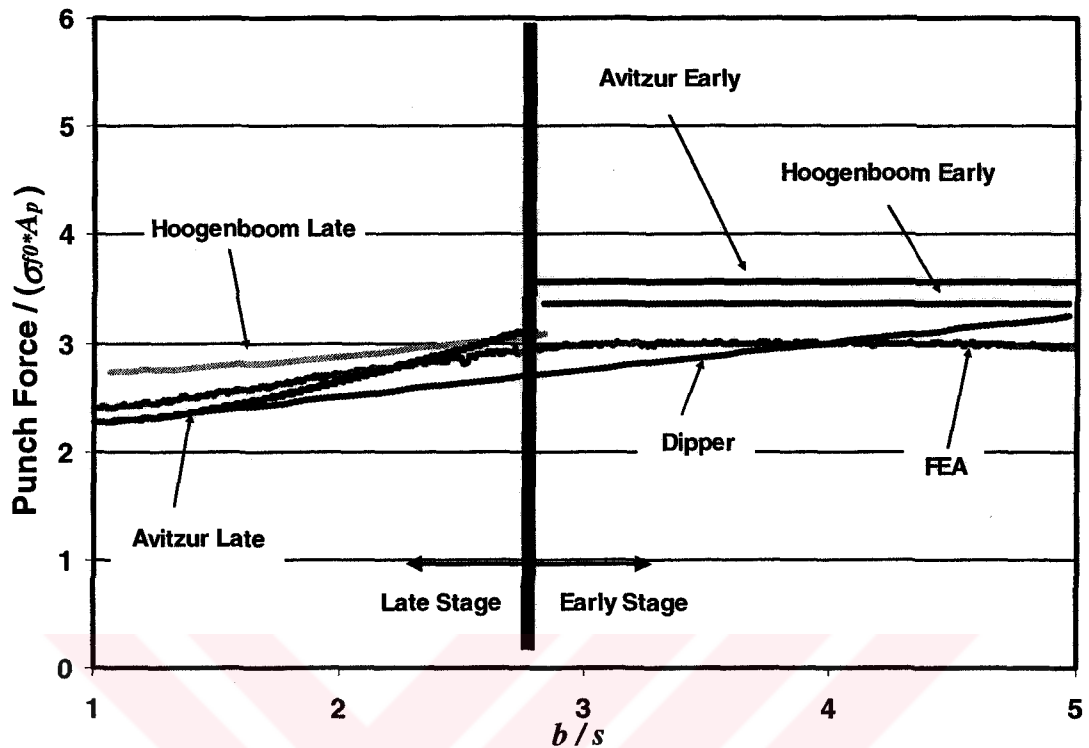


**Figure 5.10** Total Power Comparison for 60% Area Reduction

In Figure 5.10, the results for 60% area reduction can be seen. The results are similar to the results of 40% reduction. In the early stage of the process the solution by Hoogenboom, supplies better results and in the late stage of the process solution by Avitzur is superior. The late solution by Hoogenboom predicts much higher forming forces compared to FEA results for 60 %.

Modified Dipper's solution seems to give good results for non-hardening and no friction case, although it has been formulated for hardening materials. Another important observation that can be done is the improvement of Dipper's solution due to the increase in area reduction. Dipper's solution supply reasonable values at the end of stroke of the process in area reductions over 50%.

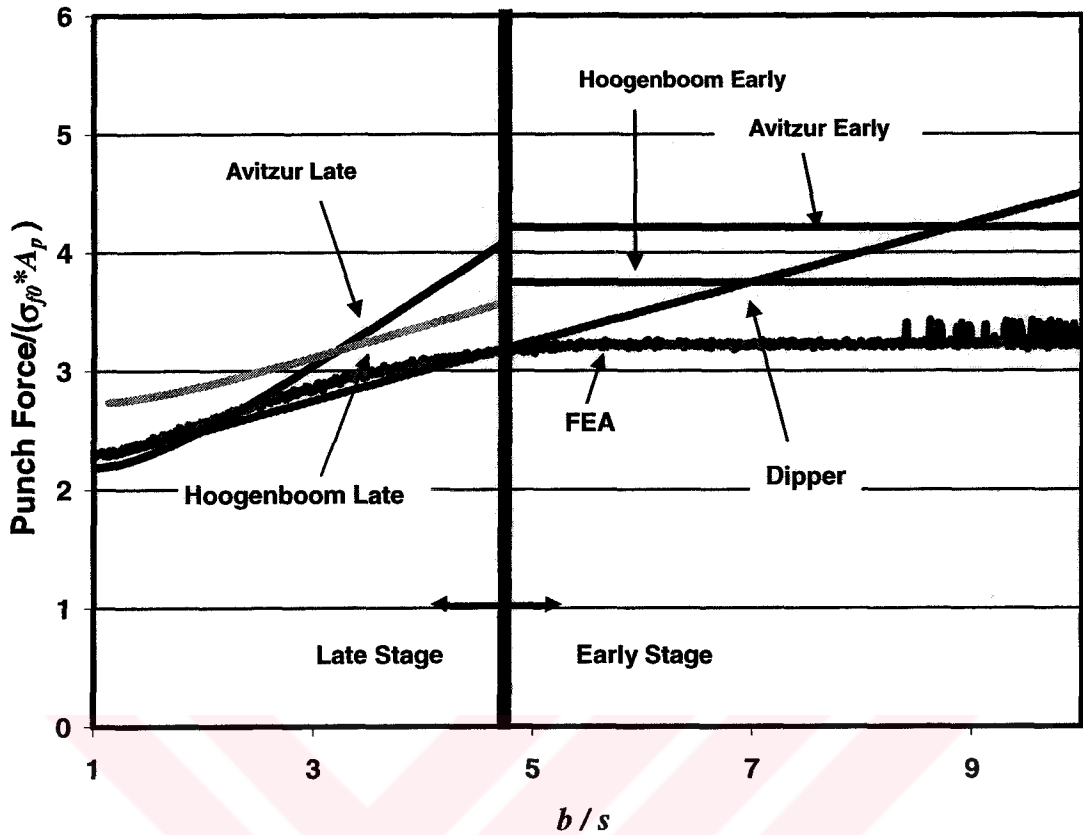


**Figure 5.11** Total Power Comparison for 80% Area Reduction

For 80% area reduction, Dipper's solution is nearly exact for late stage of the process. The Avitzur's solution provides better results for late stage of the process and Hoogenboom's solution is better for the early stage

As it can be clearly seen from the Figures 5.9, 5.10 and 5.11, the late solution by Avitzur has improved results as the area reduction increases. For the early stage, Both Hoogenboom's and Avitzur's solution tend to increase the gap between their results and FEA results.

The process is divided into two stages due to the definitions of velocity fields as stated before. The force-displacement curve obtained from FEA; clearly show the

decrease in the total force after certain amount of penetration. This location where the decrease in the punch force starts can be considered as the transition from early stage to late stage.

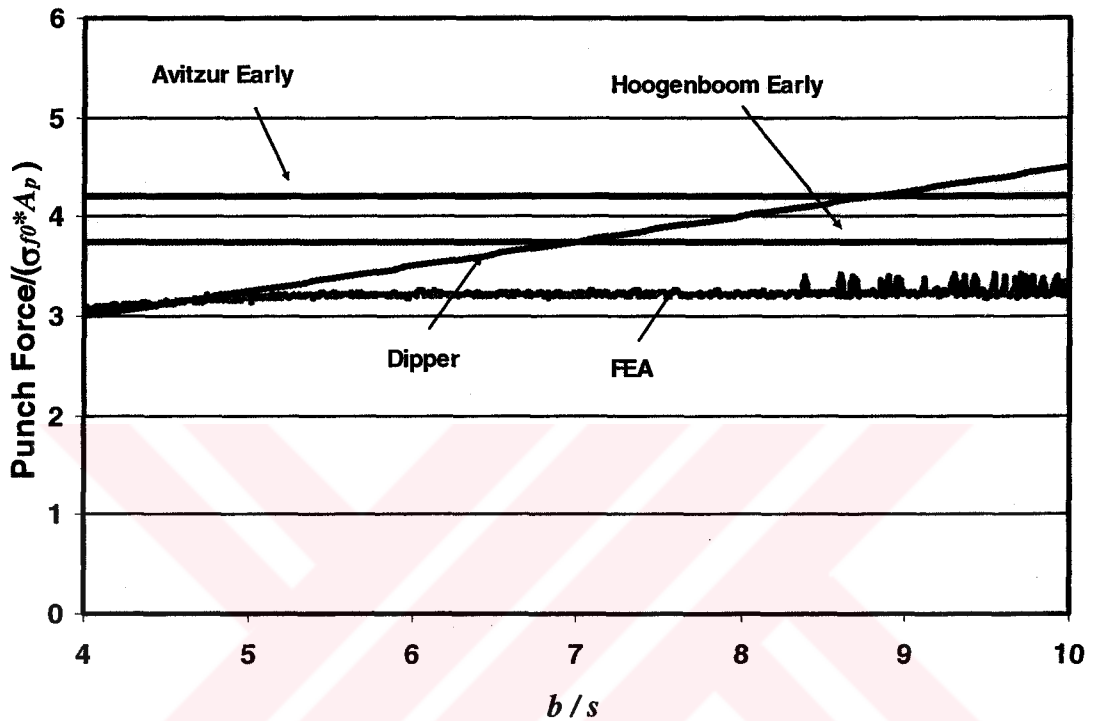


**Figure 5.12** Total Power Comparison for 80% Area Reduction (Early Stage)

The characteristic of the early stage is the presence of a dead zone at the die bottom. This section of the material considered to be undeformed during the initial deformation. The resistance of this dead zone during the early stages of the deformation results in a higher punch force value. As the punch penetrates into the material, after a certain bottom thickness value, the dead zone disappears. As soon as the dead zone diminishes the punch force starts to drop. This decrease in the punch force is due to the decrease in the amount of material, which results in decrease of resistance to forming.

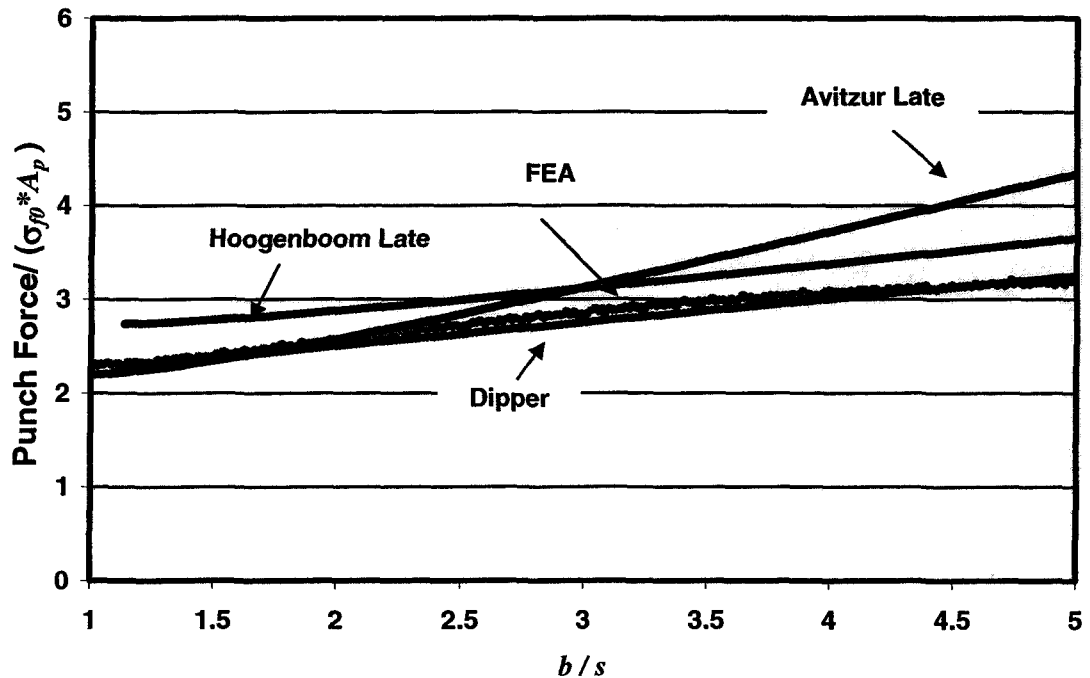


**Figure 5.13** Total Power Comparison for 80% Area Reduction (Late Stage)

#### 5.4.2 Comparison of Analytical Equations with FEA Results with Friction

In the previous section the comparison of internal deformation and shear terms were taken into account. In real life friction is always present, so it is important to examine the contribution of friction to the total power term for backward can extrusion.

In upper bound solutions, shear model is used for friction definition. This value, as stated in Chapter 2, can vary between zero and one, depending on the process.

In the presence of friction, the early solution by Hoogenboom is still better compared to one of Avitzur. It nearly gives the same force for 40% area reduction. The success of Hoogenboom's solution is the result of the optimization for early stage. In the late stage, both Hoogenboom's and Avitzur's solutions, are very close to FEA results.

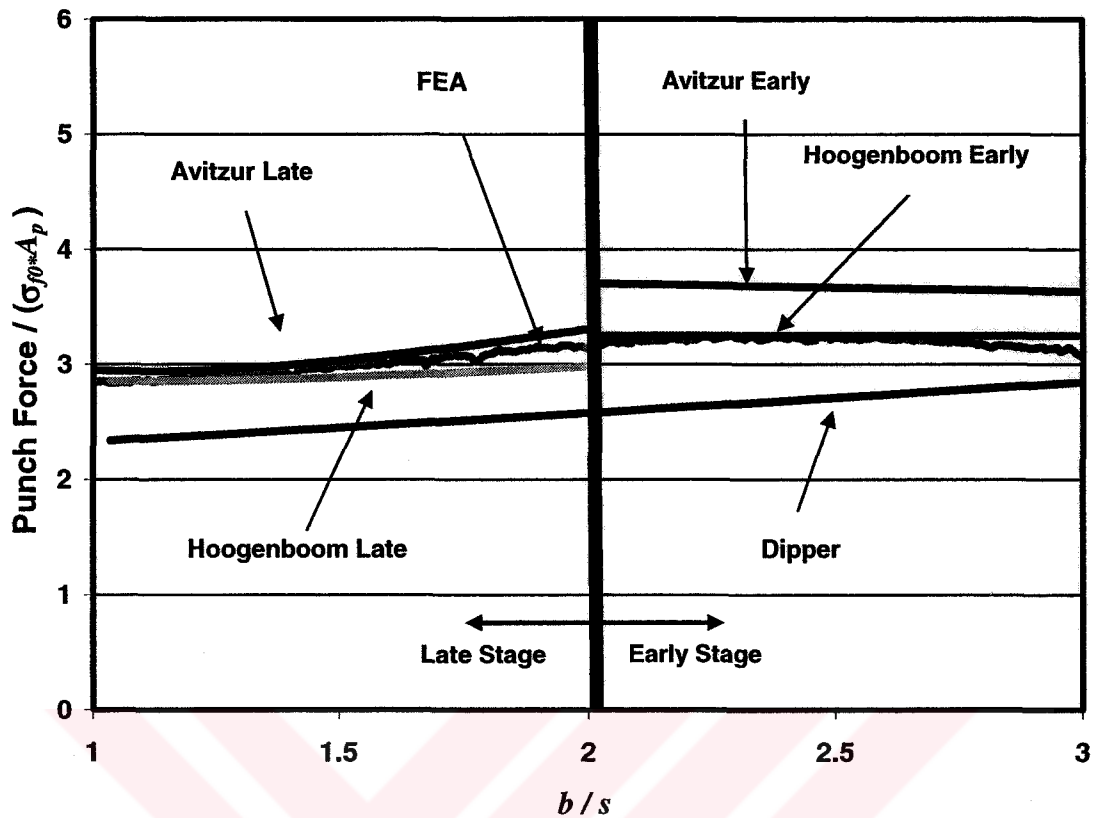


**Figure 5.14** Total Power Comparison for 40% Area Reduction ( $m=0.1$ )

As the area reduction increases, for early stage both of the solution diverge from the FEA results. Whereas Hoogenbooms's solution still supply better results compared to Avitzur's solution.

For late stage, increase in area reduction, results in divergence of Avitzur's solution, on the contrary, Hoogenboom's solution still supplies nearly exact power values. The friction modeling of Hoogenboom seems to be superior compared to Avitzur's modeling since Avitzur's model can maintain its stability for high area reductions. The solution by Dipper is valid for area reductions more than 50-60 % so for 40% are reduction, the results are far away from the FEA results. These results are not sufficient to judge the success of the solution by Dipper. Dipper's formulation provides poor results for non-hardening materials with friction due to the modifications that has been done on the model in section 5.2.

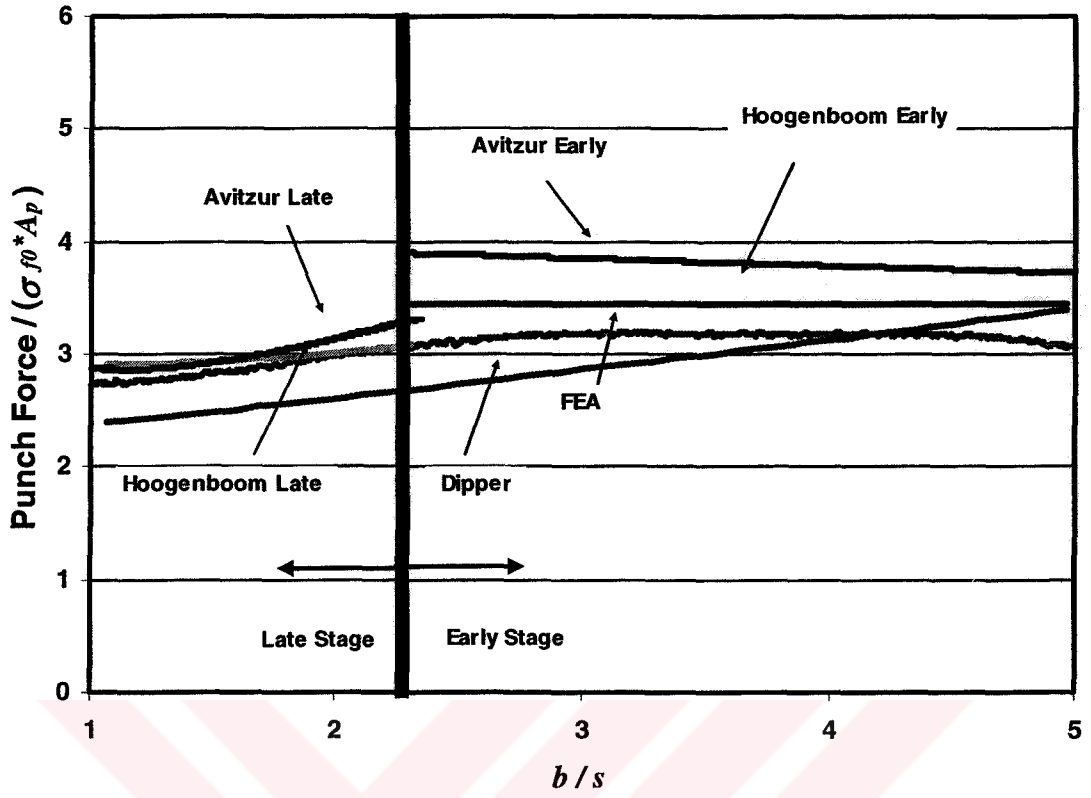


Figure 5.15 Total Power Comparison for 60% Area Reduction ( $m=0.1$ )

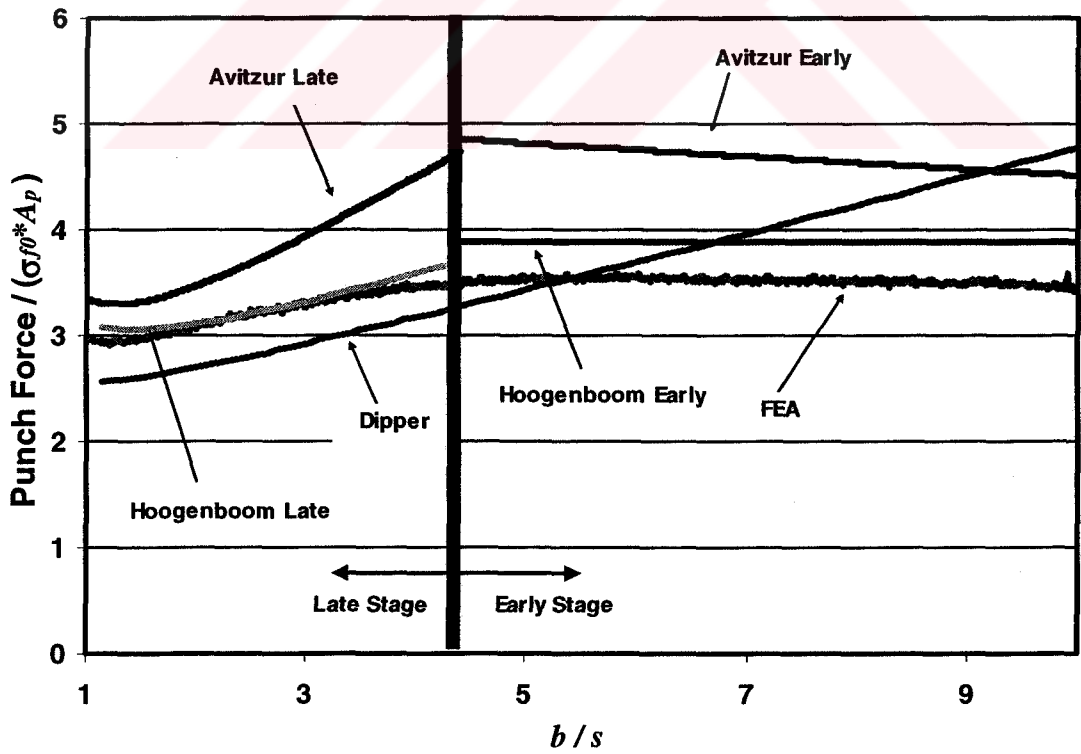


Figure 5.16 Total Power Comparison for 80% Area Reduction ( $m=0.1$ )



For 80% area reduction, Dipper's solution is nearly exact for late stage of the process. The Avitzur's solution provides better results for late stage of the process and Hoogenboom's solution is better for the early stage (Figure 5.16)

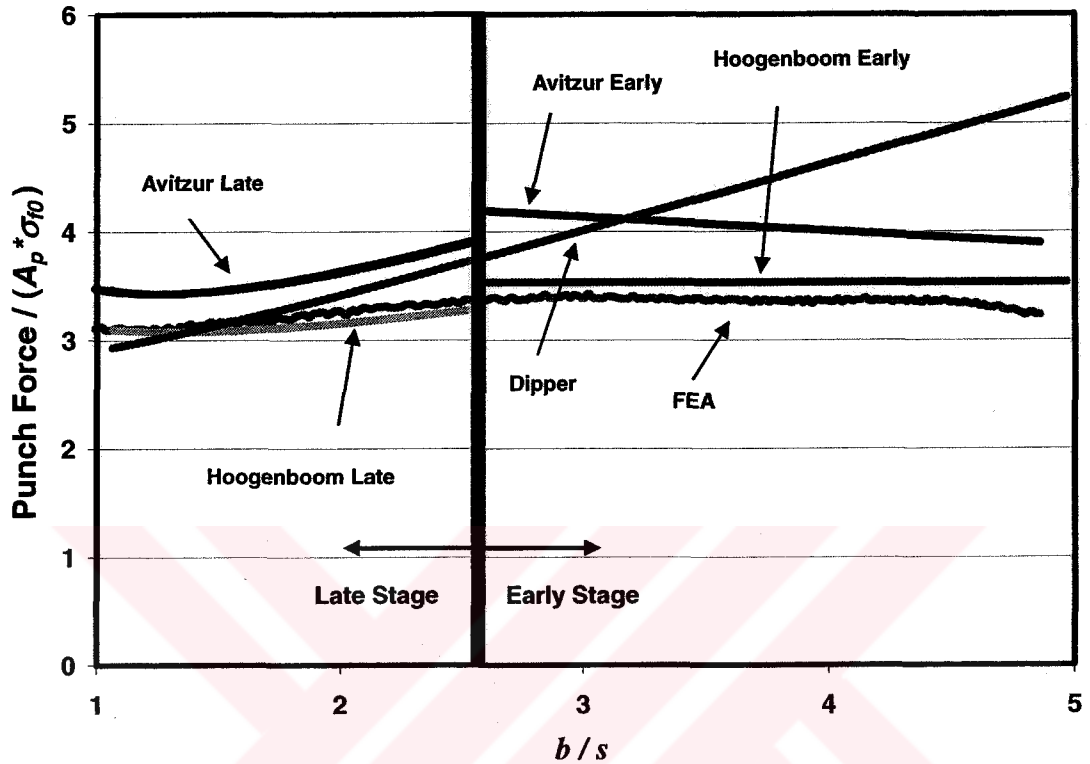
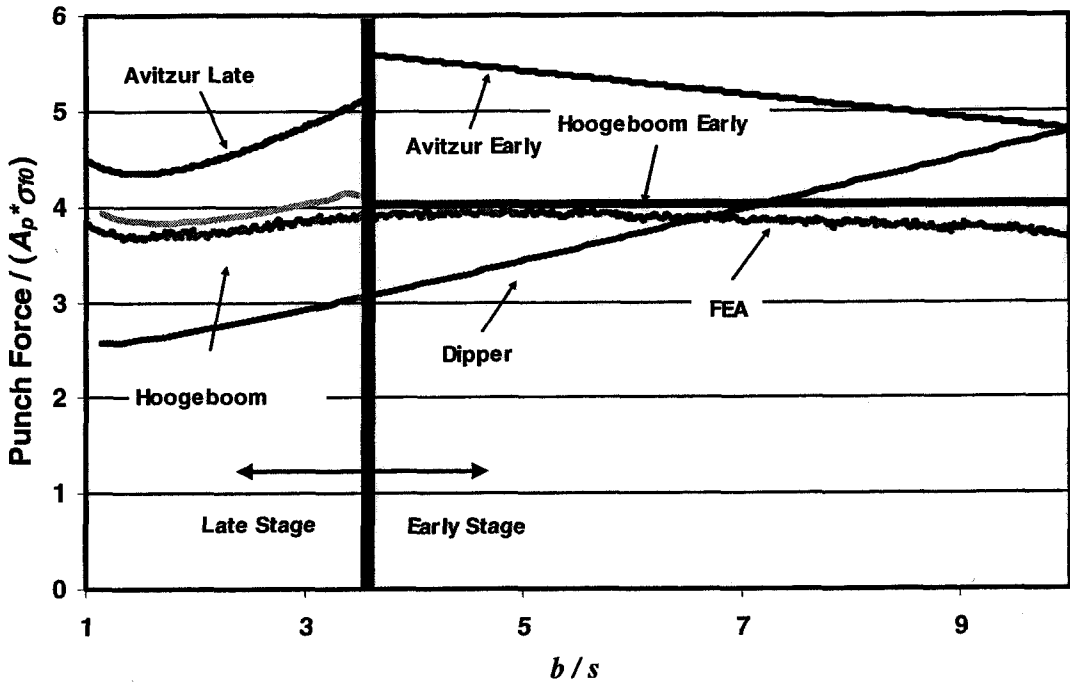


Figure 5.17 Total Power Comparison for 60% Area Reduction ( $m=0.2$ )



**Figure 5.18** Total Power Comparison for 80% Area Reduction ( $m=0.2$ )

For a different friction factor ( $m$ ), the formulations have similar behaviors. Avitzur's late stage solution diverges as the area reduction increases and his early solution is far away from the FEA results. The solutions that are proposed by Hoogenboom's solution are much better for late and early stages of the process.

### 5.4.3 The Transition from "Early Stage" to "Late Stage"

As it can be seen in Figure 5.19, the punch force-displacement curve for backward can extrusion has a certain behavior; the first part of the curve is a constant line which describes the early stage of the process. The presence of the dead zone under the punch results in a higher punch force compared to the late stage. After a certain punch displacement, the force start to decrease since the dead zone vanishes and all the material under the punch starts deforming. As the punch advances, the amount of material that resists to the punch decreases and the punch force drops. The location where the punch force starts to decrease can be named as the location of transformation from early to late stage.

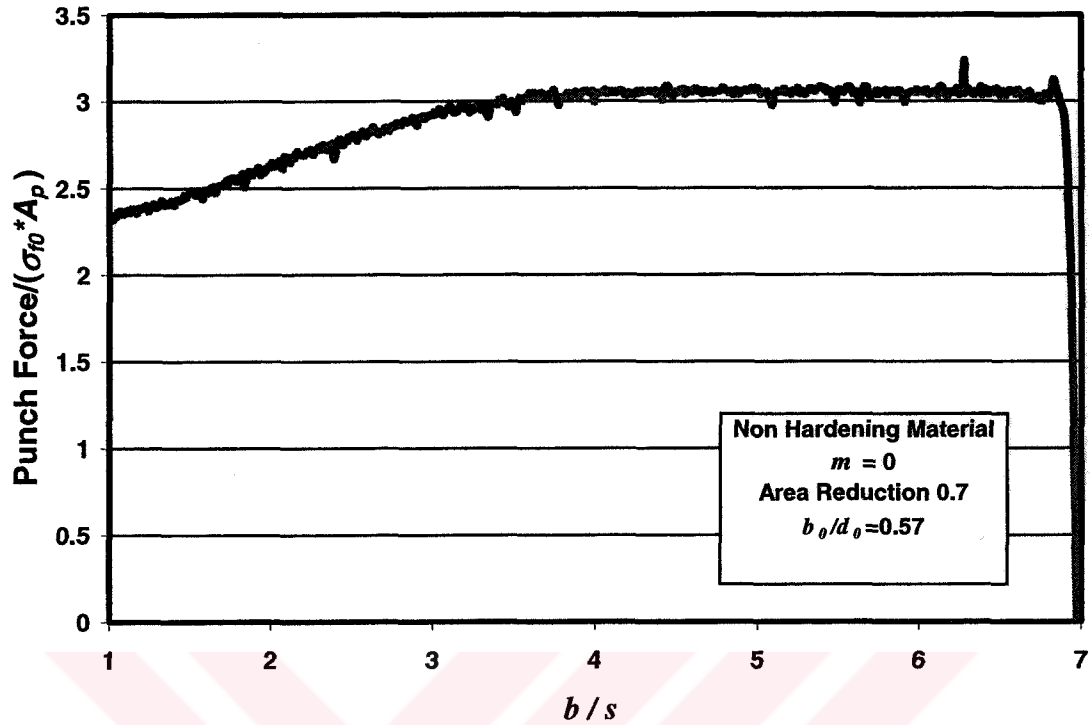


**Figure 5.19** Normalized Punch Force-Displacement Curve for a non-hardening material

As it can be seen in Figure 5.20, the location of the transformation can be expressed as a linear function of the area reduction. This eases the prediction of the force for forming and prevents the misuse of the formulations.

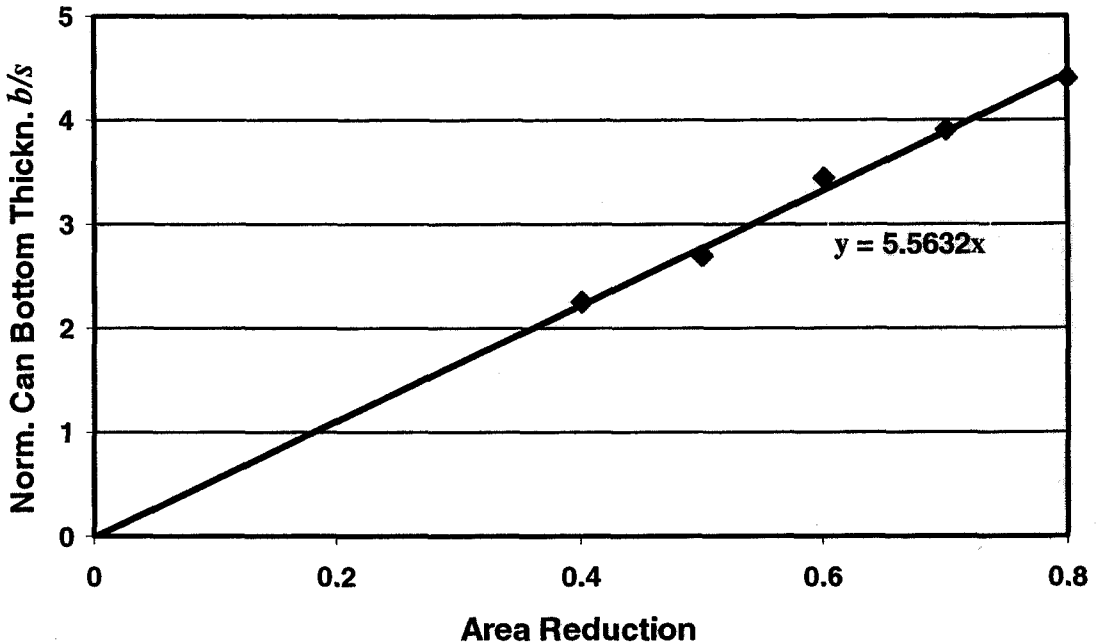


**Figure 5.20** Transformation from Early to Late Stage

### 5.5 The Effect of Initial Geometry

The geometry of the workpiece has an effect on the total power. The outcome of the variation of the initial geometry of the billet should be examined. For this purpose the initial diameter of the workpiece is kept constant and the initial height ( $b_0$ ) has been varied. The results that are tabulated are for  $b_0$  values of 7.4 mm, 11.4 mm, and 17.4 mm for a billet of 20 mm diameter.

For the case of no-friction, the punch-displacement curve is not affected by the increase in length as it can be seen in Figure 5.21. This is due to the fact that the shear and internal deformation terms are independent of the initial height of the billet. As a result changing the initial height of the billet does not affect the total power.

As it can be seen from Avitzur's formulation both for late and early stages, the friction losses depend on the initial height of the billet denoted as  $b_0$ . This effect diminishes when friction factor is equal to zero.

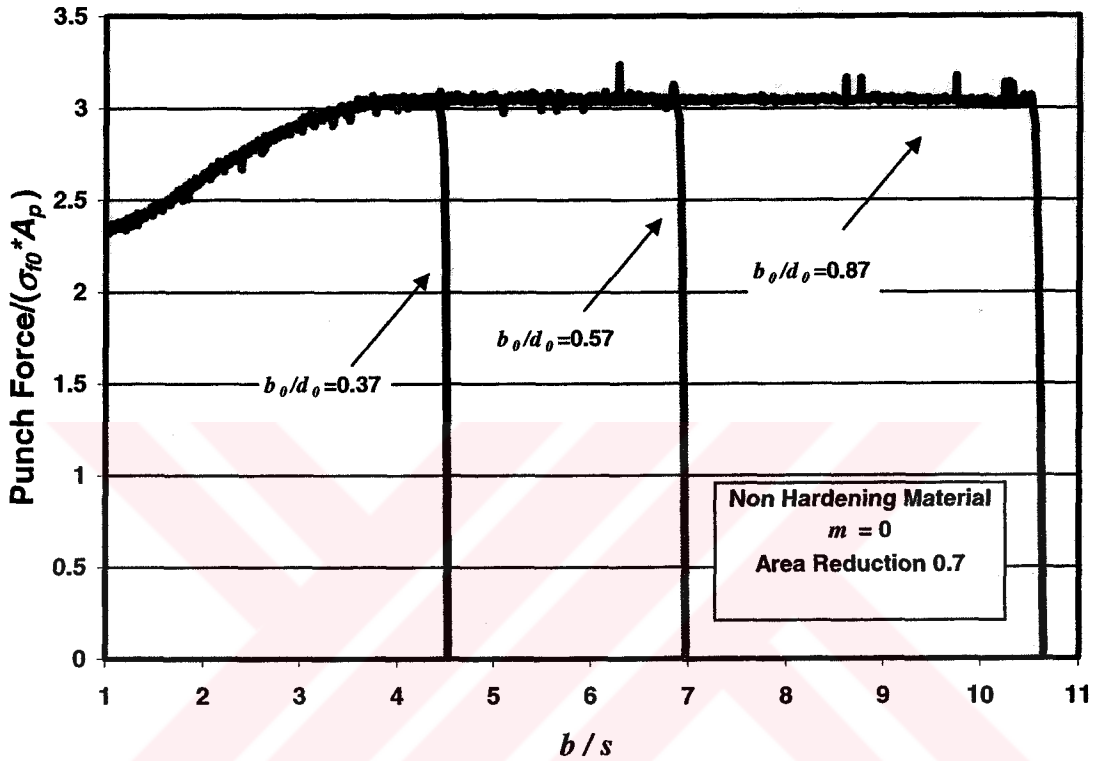


Figure 5.21 Effect of Initial Billet Length ( $m=0$ )

#### Late Stage Solution by Avitzur

$$p_r = \frac{-2}{1-(r_0/r_i)^2} \ln(r_0/r_i) + \frac{1}{\sqrt{3}} \left\{ \frac{1}{3} \frac{(r_0/r_i)^3 + 1}{b/r_i} \left( 1 + \frac{4(r_0/r_i)(b/r_i)^2}{[(r_0/r_i)^2 - 1]^2} \right) \right. \\ \left. + m \left( \frac{1}{3} \frac{(r_0/r_i)^2 + 1}{b/r_i} + \frac{2(r_i/r_0)}{1-(r_i/r_0)^2} \left( \frac{b_0}{r_i} + \frac{r_0}{r_i} \frac{h}{r_i} \right) \right) \right\} \quad (5.40)$$

### Early Stage Solution by Avitzur

$$P_T = \frac{2}{\sqrt{3}} \frac{1}{1 - (r_i/r_0)^2} \left\{ \sqrt{3} f(\alpha) \ln(r_0/r_i) + \frac{\alpha}{\sin^2 \alpha} - \cot \alpha \right. \\ \left. + (\cot \alpha) \ln(r_0/r_i) + m \left[ \frac{h}{r_i} + \frac{r_i}{r_0} \left[ \frac{b_0}{r_i} + \left( \frac{r_0}{r_i} - 1 \right) \cot \alpha \right] \right] \right\} \quad (5.41)$$

The solutions by Tekkaya and Hoogenboom are independent of the initial length due to the formulation of friction power. As a result for these formulations the force-displacement curve is not affected by geometry modification due to an increase in length. The results supplied by finite element analysis prove that when friction is present between the workpiece and the die, the total power is a function of initial height.

Initial length has an effect on the total power only when friction is present between the contact surfaces. As it can be in Figure 5.22, there is a 1-2% increase in the punch force due to the friction (when  $m=0.1$ ). This can easily be explained by the solution of Avitzur, who includes the initial geometry in his solutions (Eq. (5.40) and Eq. (5.41)). The increase for the total power is assumed to be around 5% for Avitzur's formulation, which is sufficient to explain the increase in finite element results.

As the friction factor increases, so does the difference between the total power for different initial billet lengths. The difference between the punch forces increases up to 5% for  $m=0.2$  and 10% for  $m=0.3$  as seen in Figure 5.23 and 5.24.

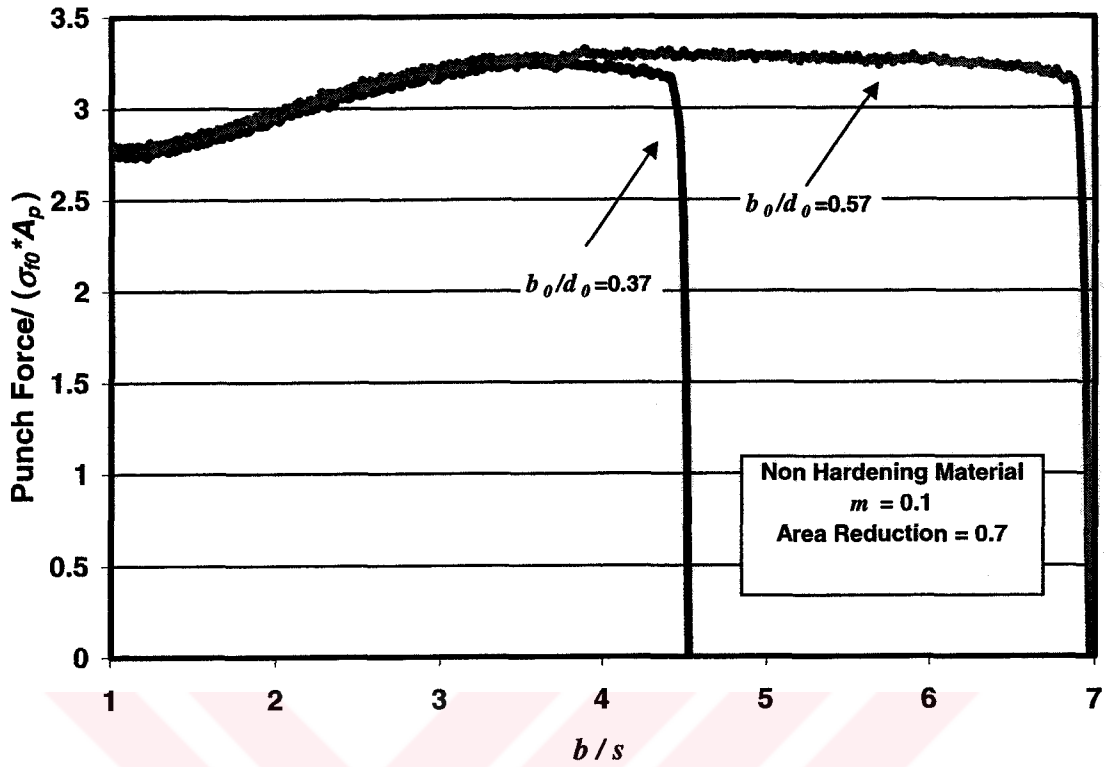


Figure 5.22 Effect of Initial Billet Length ( $m=0.1$ )

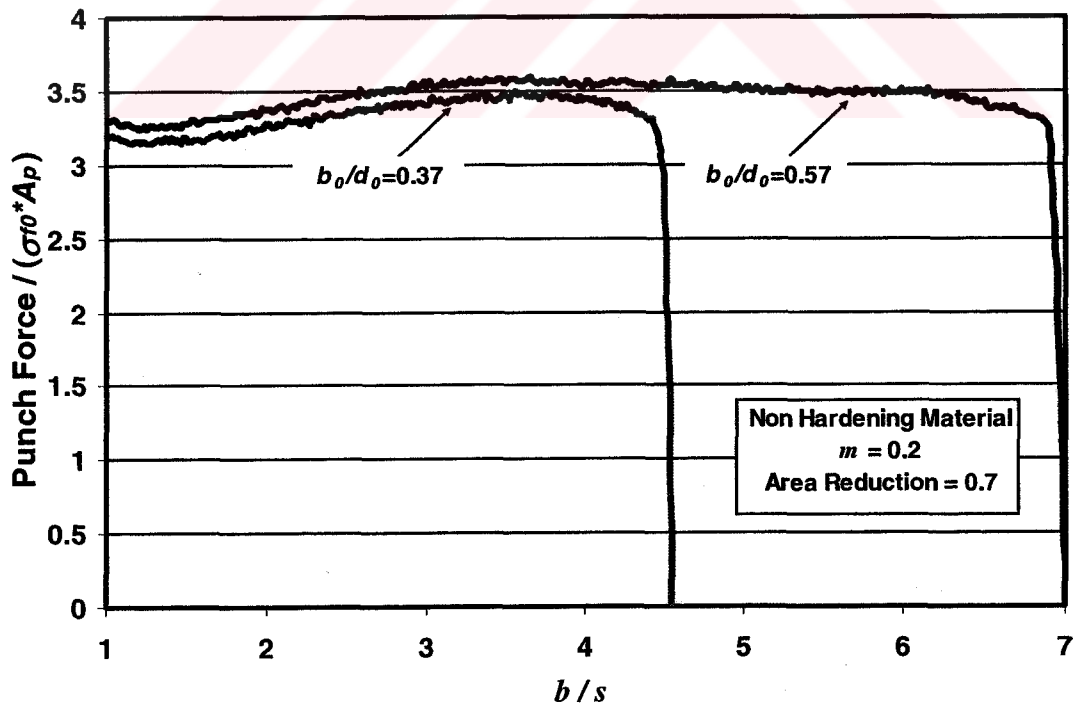


Figure 5.23 Effect of Initial Billet Length ( $m=0.2$ )

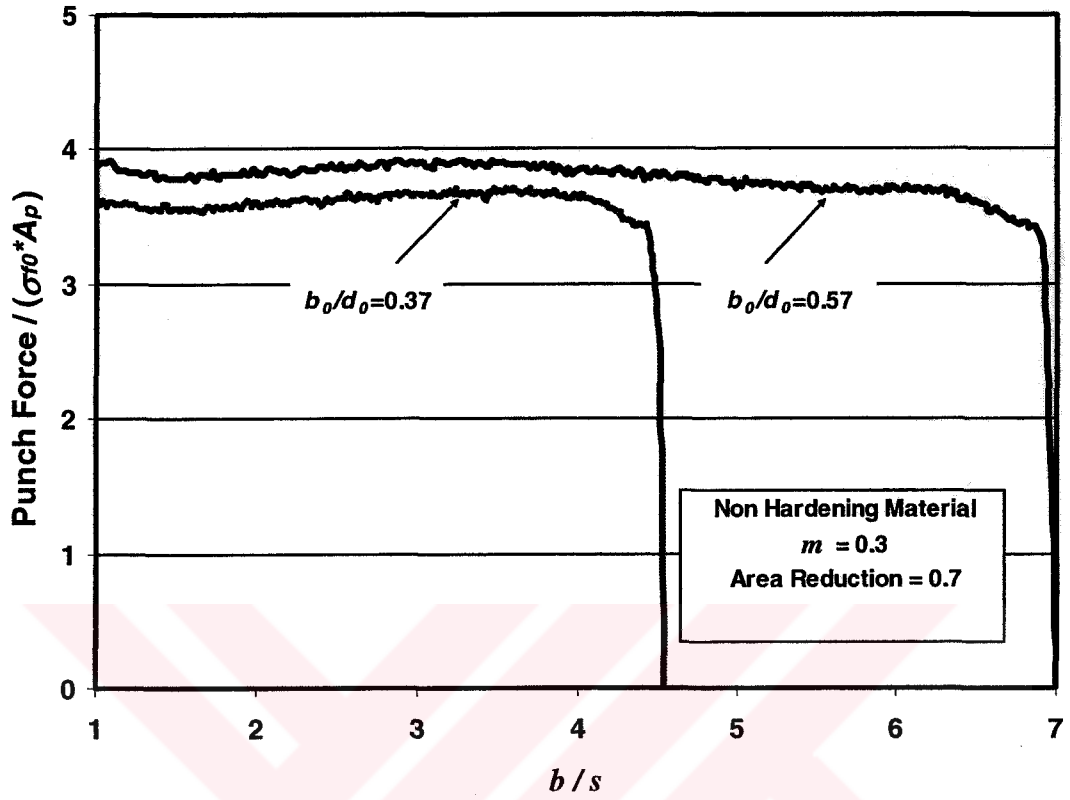


Figure 5.24 Effect of Initial Billet Length ( $m=0.3$ )



## **CHAPTER 6**

### **ASSESSMENT OF ANALYTICAL EQUATIONS FOR HARDENING MATERIALS**

#### **6.1 Introduction**

The upper bound solution is formulated for non-hardening materials which have a constant flow stress throughout the process. In the real processes the material is strain-hardening, which means that the flow stress increases as the material is deformed.

In this chapter, the previously assessed non-hardening formulations will be modified for hardening materials. The definition of strain and flow stress will be formulated for all upper bound solutions explained previously. At the end of the chapter the comparison of these modified solutions with FEA results will be done.

#### **6.2 Definition of Strain and Flow Stress**

In order to make upper bound solutions, which are for non-hardening materials, applicable to hardening solutions, clear definitions of total equivalent plastic strain have to be done. Total equivalent plastic strain values will be used for obtaining the flow stress. For the calculation of total equivalent plastic strain, equivalent strain rates have to be derived from the velocities of the discontinuity surfaces. After the calculation of the strain rate, the total equivalent plastic strain can be calculated as:

$$\bar{\epsilon} = \int_{t_0}^t \dot{\bar{\epsilon}} dt \quad (6.1)$$

As a result each zone requires a definition of flow stress for its specific deformation characteristics. The flow stress is defined by Ludwik's Equation:

$$\sigma_f = C\bar{\epsilon}^n \quad (6.2)$$

### 6.3 The Modifications for Two-Zone Velocity Field

In Avitzur's Late Stage solution, the material is divided into two zones. The deforming zone experiences strain only due to the upsetting of the material. As explained in Appendix A, the strain for axial upsetting is defined as:

$$\bar{\epsilon}_{upsetting} = \ln\left(\frac{b_0}{b}\right) \quad (6.3)$$

where  $b_0$  is the initial billet height and  $b$  is the bottom thickness.

The validity of this strain definition has been checked by finite element analysis results. The strain data has been taken along the symmetry axis and along the vertical path under the corner of the punch as seen in Figure 6.1.

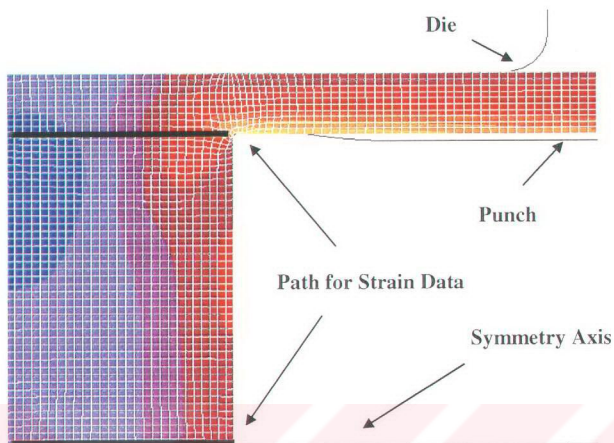


Figure 6.1 Determination of Total Eq. Plastic Strain for Deforming Zone

The data along the axis is taken and the average of those data is assumed to be the strain for the specific bottom thickness.

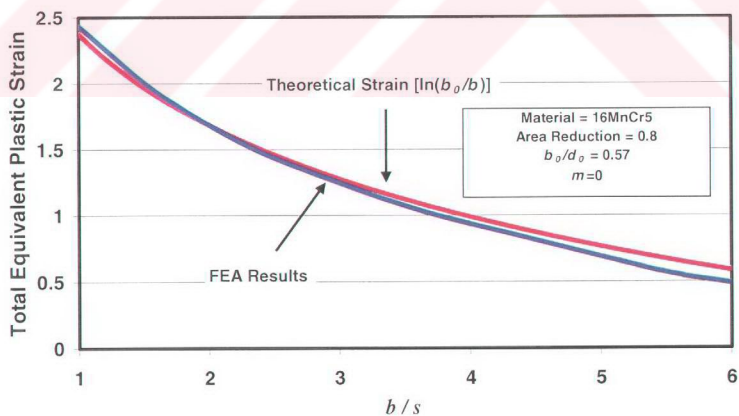


Figure 6.2 Total Eq. Pl. Strain for Late Stage

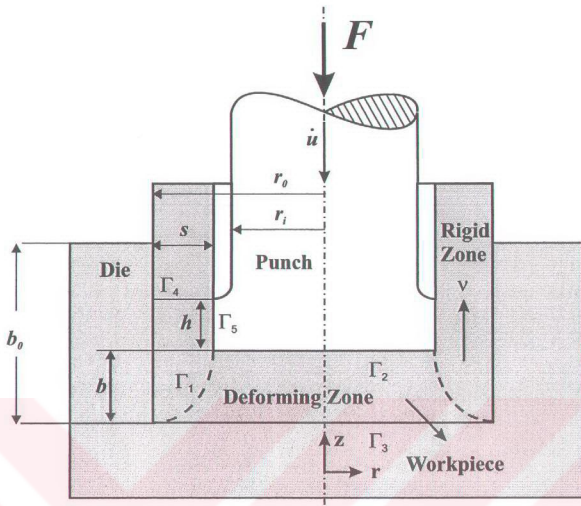


Figure 6.3 Two-Zone Velocity Field

Similar curves were obtained for all of the area reductions that are examined in this study. From the results seen in Figure 6.2, it is proven that for the deforming zone for the late stage solution, the strain defined in Eq. (6.3) is reasonable. This will result in the definition of flow stress for deforming zone as:

$$\sigma_{f1} = C\bar{\epsilon}_1^n = C \left( \ln \left( \frac{b_0}{b} \right) \right)^n \quad (6.4)$$

When the material starts moving to the annular gap between the punch and the die, it has to be further strained by passing through the shear plane  $\Gamma_1$  (Figure 6.3).

The additional strain caused by the shearing of the material can be expressed as a function of the area reduction. The total equivalent plastic strain for area reduction for extrusion process can be defined as:

$$\bar{\epsilon}_{shearing} = \ln\left(\frac{A_0}{A_f}\right) \quad (6.5)$$

where  $A_0$  is the initial billet area and  $A_f$  is the final billet area. The final area for backward can extrusion is defined as the area of the ring that is between the die and the punch:

$$A_f = A_0 - A_p \quad (6.6)$$

where  $A_p$  is the area of the punch.

As a result of this the total equivalent plastic strain for rigid zone will turn out to be

$$\bar{\epsilon} = \bar{\epsilon}_{upsetting} + \bar{\epsilon}_{shearing} = \ln\left(\frac{b_0}{b}\right) + \ln\left(\frac{A_0}{A_0 - A_1}\right) \quad (6.7)$$

The strain definition for the rigid zone is also checked from finite element analysis results with a similar manner. This time the total equivalent strain rate values for the deformed material is check and compared with Eq. (6.7). For this sake the average strain had to be defined for the exit zone of the material. As seen in Figure 6.5, the equivalent plastic strain data was taken along the horizontal axis along various planes. Later, the mean of this data was taken by weighing it with respect to volume.

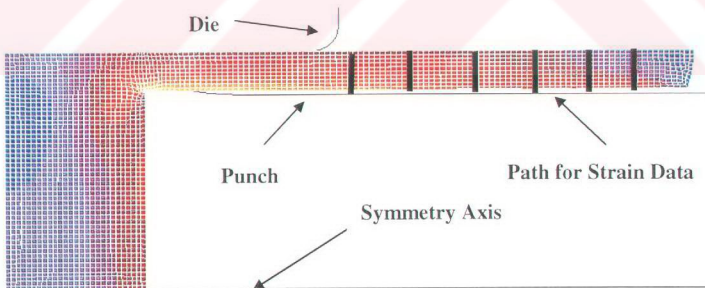


**Figure 6.4** Determination of Total Eq. Plastic Strain for Rigid Zone

As seen in Figure 6.5 which is for 80% area reduction, the theoretical strain and the finite element results are very similar to each other. The strain that is assumed to be dominant in the rigid zone is very realistic.

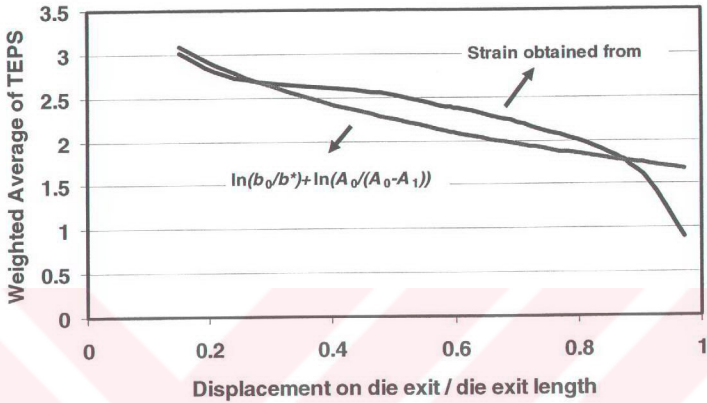


Figure 6.5 Total Eq. Pl. Strain for Early Stage

The flow stress for the rigid zone will be defined by Ludwik's Equation as:

$$\sigma_{f2} = C\bar{\epsilon}_r^n = C \left( \ln \left( \frac{b_0}{b} \right) + \ln \left( \frac{A_0}{A_0 - A_1} \right) \right)^n \quad (6.8)$$

The next step is to convert the non-hardening solution into a hardening solution by multiplying each power term with related flow stress. Referring to Figure 6.3, the power for deformation zone is multiplied by  $\sigma_{f1}$  (Eq. (6.4)), since there is only deformation due to upsetting occurs. Friction power for  $\Gamma_3$  plane also is a function of  $\sigma_{f1}$ , since shearing does not occur for the material on that plane. Whereas friction power for  $\Gamma_4$  and  $\Gamma_5$  planes should be multiplied by  $\sigma_{f2}$  (Eq. (6.8)), since material moving on those planes have sheared through  $\Gamma_1$  plane. The shear power for for  $\Gamma_1$

should also be multiplied by  $\sigma_{f2}$  due to shearing. Hence the total power term for hardening material will turn out to be:

$$P_T = \sigma_{f1} A_p \left\{ \frac{-2}{1-(r_0/r_i)^2} \ln(r_0/r_i) + \frac{m}{\sqrt{3}} \left( \frac{1}{3} \frac{(r_0/r_i)^2 + 1}{b/r_i} \right) \right\} \quad (6.9)$$

$$+ \sigma_{f2} A_p \left\{ \frac{1}{3\sqrt{3}} \frac{(r_0/r_i)^3 + 1}{b/r_i} \left( 1 + \frac{4(r_0/r_i)(b/r_i)^2}{[(r_0/r_i)^2 - 1]^2} \right) + \frac{m}{\sqrt{3}} \frac{2(r_i/r_0)}{1-(r_i/r_0)^2} \left( \frac{b_0}{r_i} + \frac{r_0}{r_i} \frac{h}{r_i} \right) \right\}$$

#### 6.4 The Modification for Spherical Velocity Field Solution

The deforming zone which is located between two dead zones should be used for the definition of the total equivalent plastic strain. The deformation zone, due to its shape includes both effect of shearing and upsetting of the material during deformation. Due to this fact the strain for this zone can be formulated as:

$$\bar{\epsilon} = \ln \left( \frac{A_0}{A_0 - A_p} \right) + \ln \left( \frac{b_0}{b} \right) \quad (6.10)$$

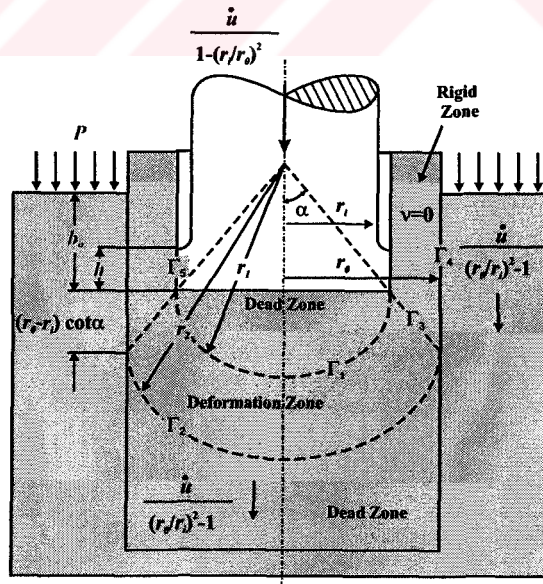


Figure 6.6 Spherical Velocity Field







## 6.5 The Modification for Three Zone Velocity Field Solution

As stated in Chapter 5, the thin-walled solution supplies better results, due to this fact, only the modification for thin-walled solutions is done.

### 6.5.1 Late Stage Solution

The three zone velocity field has two deformation zones as seen in Figure 6.8.

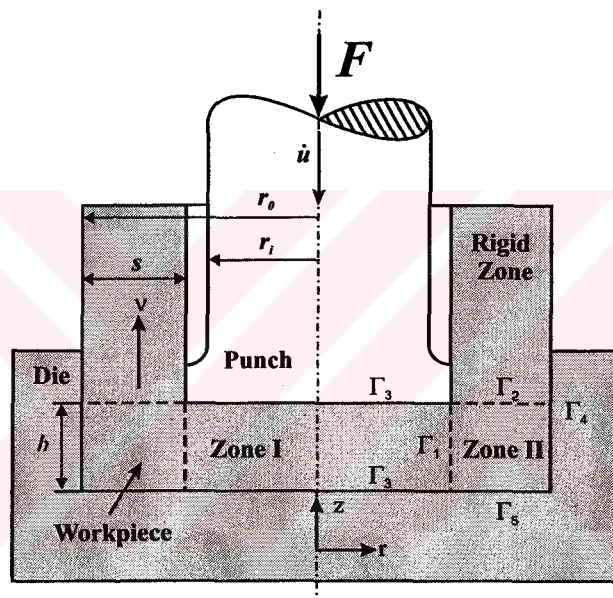


Figure 6.8 Three-Zone Velocity Field

The equivalent strains for these two zones are formulated in 3.3.1.3. The strains for thin-walled solution are:

$$\bar{\varepsilon}_I = \ln\left(\frac{b_0}{b}\right) \quad (6.13)$$

$$\dot{\varepsilon}_{II} = \frac{1}{\sqrt{3}} \frac{r_i}{s} \ln\left(\frac{b_0}{b}\right) \quad (6.14)$$

The flow stresses for these two zones are obtained by inserting the strain equations into Ludwick's Equation. The flow stresses for thin-walled solution are:

$$\sigma_{f1} = C\bar{\epsilon}_1^n = C\left(\ln\left(\frac{b_0}{b}\right)\right)^n \quad (6.15)$$

$$\sigma_{f2} = C\bar{\epsilon}_r^n = C\left\{\frac{1}{\sqrt{3}}\frac{r_i}{s}\ln\left(\frac{b_0}{b}\right)\right\}^n \quad (6.16)$$

According to Figure 6.8, the internal deformation power term for zone I should be multiplied by  $\sigma_{f1}$  and the internal deformation power term for zone II should be multiplied by  $\sigma_{f2}$ . The shear power terms should be  $\Gamma_1$  and  $\Gamma_2$  should be multiplied by  $\sigma_{f2}$ , this is due to the fact that on these planes the material has already experienced the equivalent strain defined in Eq. (6.14). The friction power for  $\Gamma_3$  should be multiplied by  $\sigma_{f1}$  and the friction power for  $\Gamma_4, \Gamma_5$  should be multiplied by  $\sigma_{f2}$ .

At the end of this modification the total power term will turn out to be:

$$P_T = \sigma_{f1}A_p\left(\dot{u}\pi r_i^2 + \frac{2}{3\sqrt{3}}m\sigma_{f1}\dot{u}\pi r_i^2\frac{r_i}{b}\right) \quad (6.17)$$

$$+ \sigma_{f2}A_p\left(\frac{2}{\sqrt{3}}\dot{u}\pi r_i^2 + \frac{1}{2\sqrt{3}}\dot{u}\pi r_i^2\frac{b}{s} + \frac{1}{2\sqrt{3}}\dot{u}\pi r_i^2\frac{s}{b} + \frac{1}{\sqrt{3}}m\dot{u}\pi r_i^2\frac{s}{b} + \frac{1}{\sqrt{3}}m\dot{u}\pi r_i^2\frac{b}{s}\right)$$

### 6.5.2 Early Stage

The three zone velocity field has two deformation zones as seen in Figure 6.9

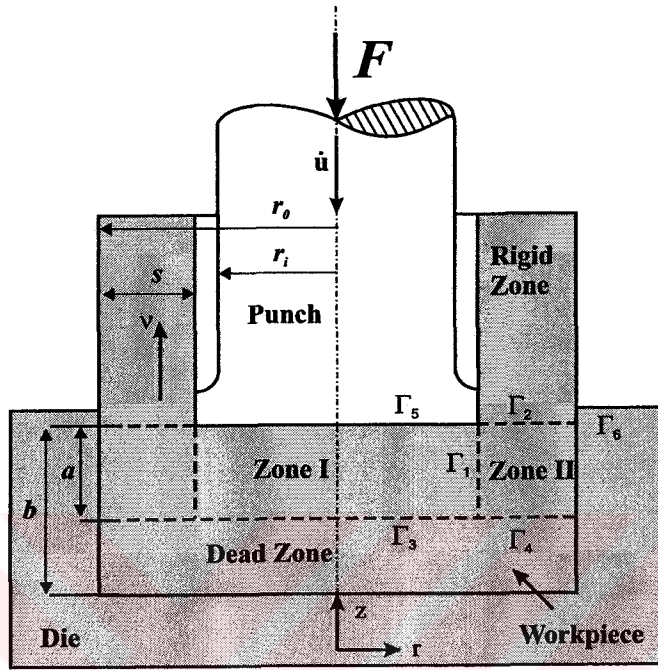


Figure 6.9 Three-Zone Velocity Field with a dead-zone

The strain and flow stress definitions for late stage solution (6.5.1), the only modification is due to presence of the dead-zone in early stage solution. The friction term for  $\Gamma_5$  and shear term  $\Gamma_3$  should be multiplied by  $\sigma_{f1}$ , the other friction terms  $\Gamma_1$ ,  $\Gamma_2$ ,  $\Gamma_4$  and friction term  $\Gamma_6$  should be multiplied by  $\sigma_{f2}$ , as it can be seen from Figure 6.9. The total power term will turn out to be:

$$P_{t(early)} = \sigma_{f1} A_p \left( 1 + \frac{(m+1)}{3\sqrt{3}} \frac{1}{\gamma} \frac{r_i}{s} \right) + \sigma_{f2} A_p \left( \frac{2}{\sqrt{3}} + \frac{1}{\sqrt{3}} \frac{1}{\gamma} + \frac{(m+1)}{2\sqrt{3}} \gamma \right) \quad (6.18)$$

### 6.6 Comparison of Results

In this section, the results of the modification for different materials will be tabulated. The upper bound solution which gives the best results for late and early

stages of the process will be stated. The material that are used for the simulations are 16MnCr5, Ck10, CuZn40. The reason for selection of those materials is due to their range of hardening exponents. The effect of different material can easily be seen with the variation of hardening exponent. The flow curves for the materials used in the finite element simulations can be seen in Figure 6.10.

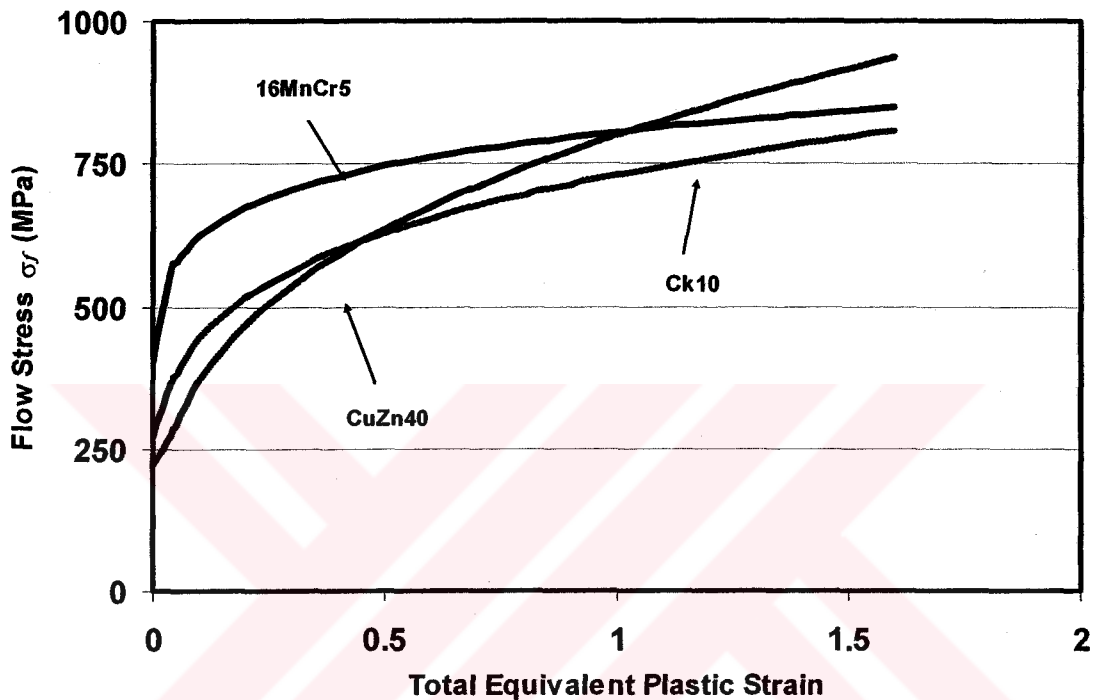


Figure 6.10 Flow Curves for the Materials

The range of area reduction is from 40-80%, which covers the commonly used values in real life applications. The geometry of the workpiece is kept constant with  $b_0/d_0$  ratio being equal to 0.57. The effect of change of initial geometry is analyzed later in the chapter. The dimensions of the punch and the initial billet are given in Appendix D.

### 6.6.1 Comparison of Analytical Equations with FEA Results without Friction

In Figures 6.11-6.13, the late stage results for 16MnCr5 for no-friction case can be seen. For this case, Avitzur's Late Stage solution provides better results with the

hardening modification explained in Section 6.3, The three-zone velocity field solution provides better results for lower area reductions but the solution worsens as the reduction increases. Even for its best performance in 40% area reduction, it is still poor compared to Avitzur's two-zone velocity field.

For 40% area reduction, Dipper's solution provides very poor results. This is due to the fact that this solution is applicable to area reductions over 50-60%.

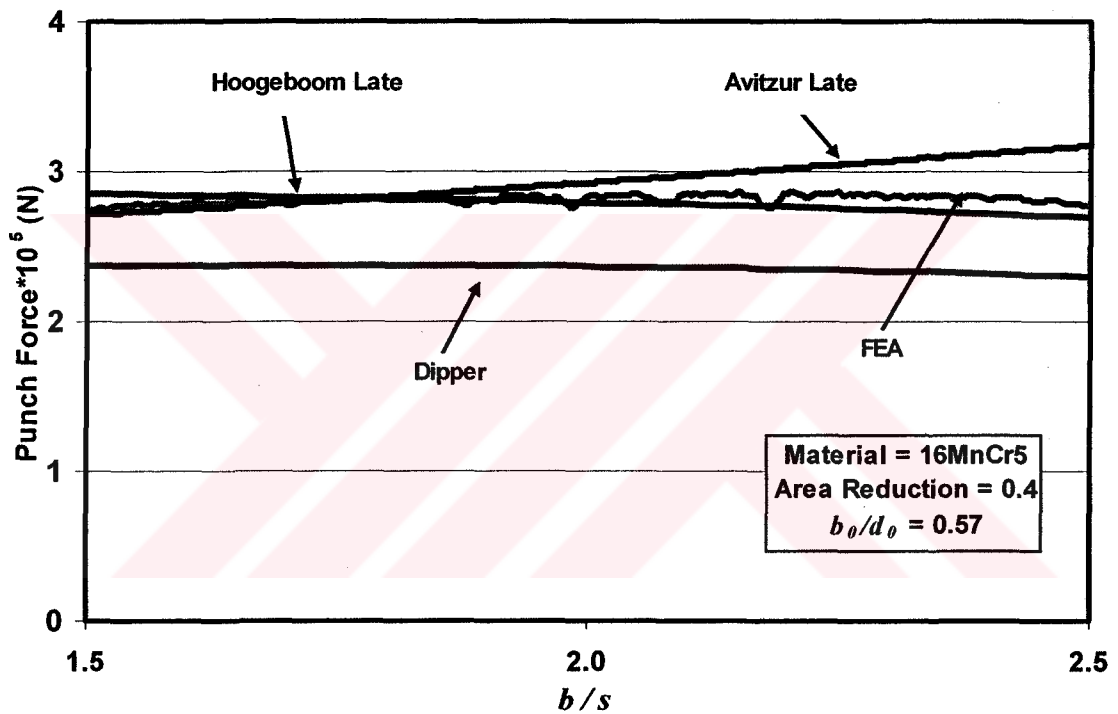


Figure 6.11 Total Power Comparison for 40% Area Reduction (Late Stage)

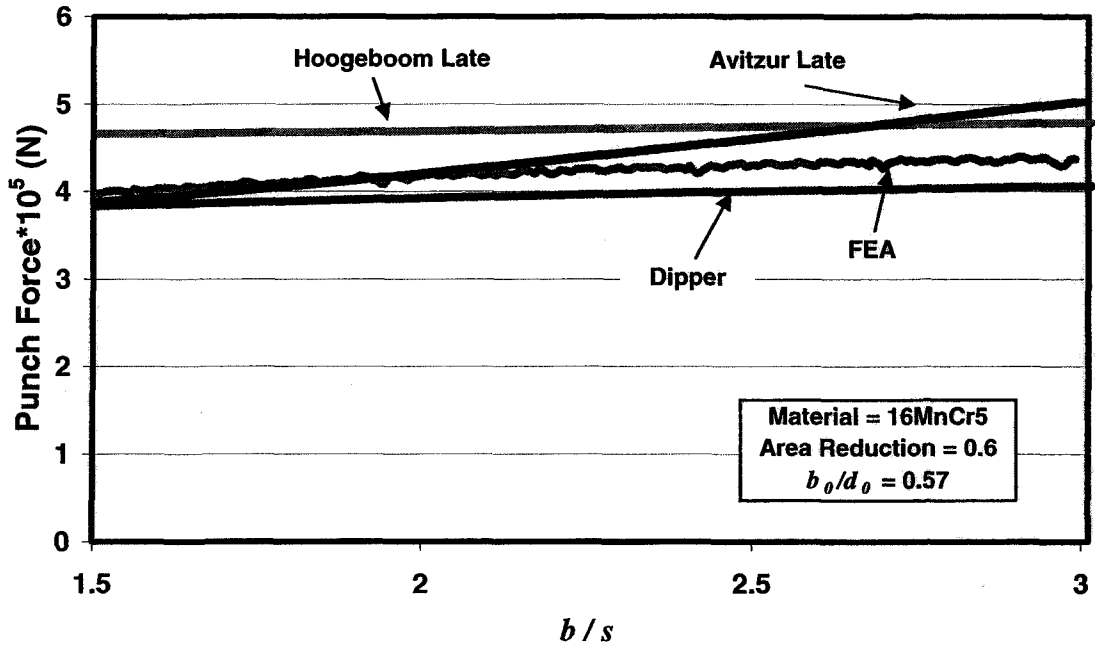


Figure 6.12 Total Power Comparison for 60% Area Reduction (Late Stage)

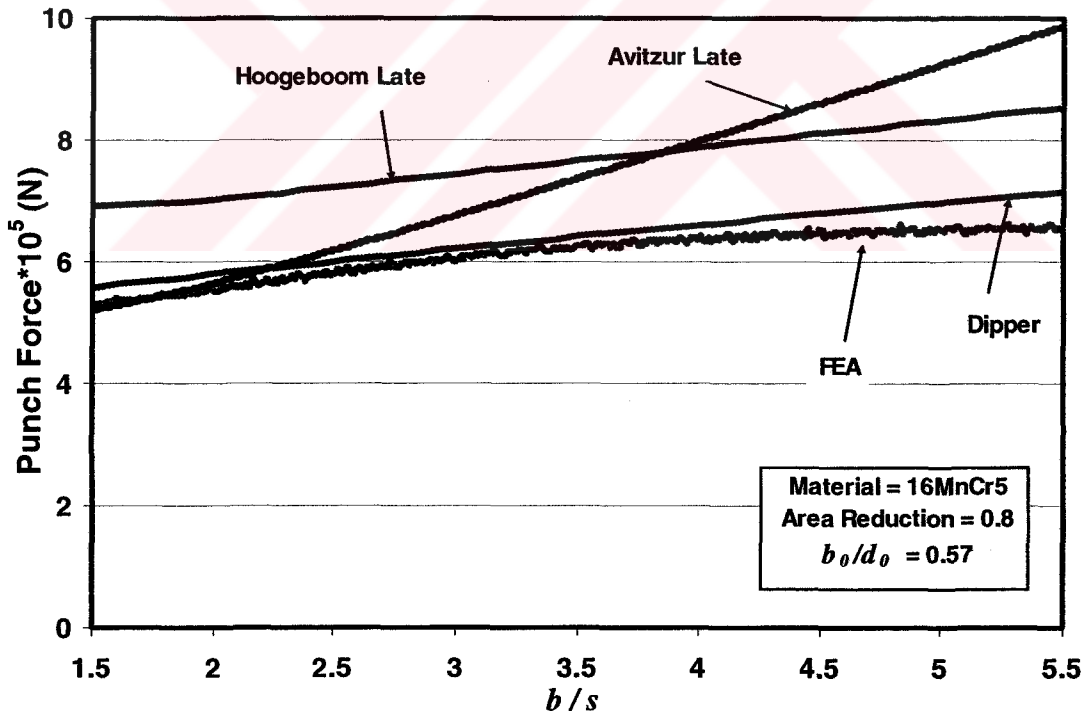
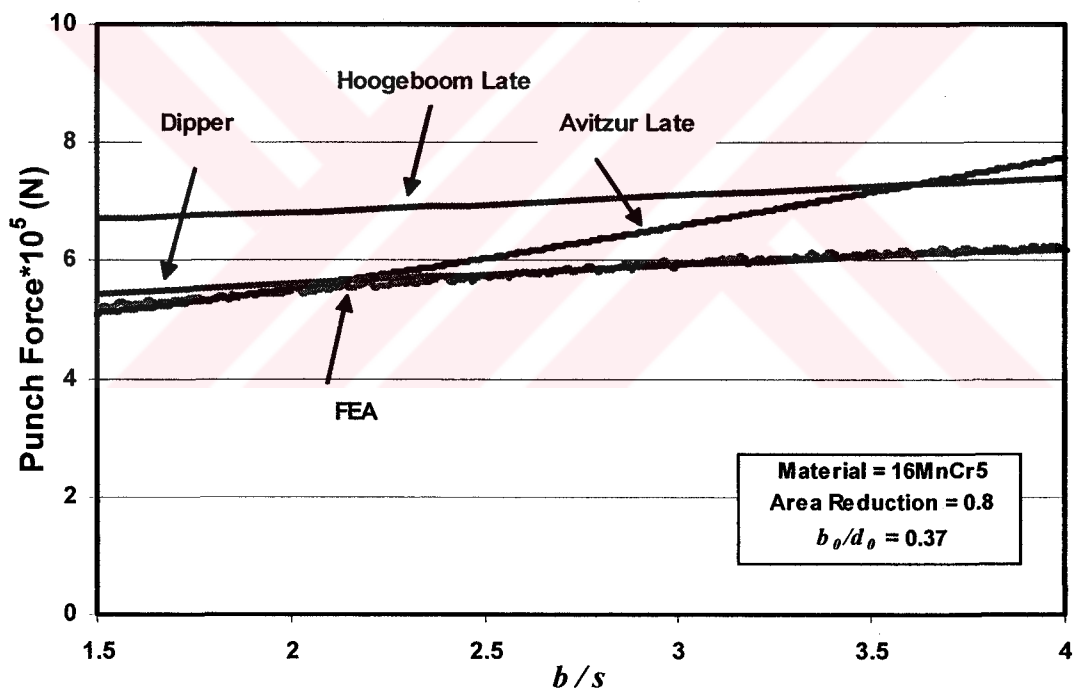


Figure 6.13 Total Power Comparison for 80% Area Reduction (Late Stage)

As the area reduction increases, the gap between the finite element analysis results and three-zone velocity field increases whereas the two-zone velocity field by Avitzur shows a more stable behavior. Dipper's solution improves as the area reduction increases, for 80% reduction; Dipper's solution gives nearly exact results. As it can be seen in Figure 6.14, the change in initial geometry does not affect the results for the case of no friction. This is due to the fact that, when friction is not present between the contact surfaces, the initial geometry does not have any effect of the total power.

For  $b_0/d_0$  ratio 0.37, Avitzur's solution still provides the best solution. Also Dipper's solution due to the fact that it is applicable to high area reductions, has a remarkable success for calculation of the total punch force (Figure 6.14)



**Figure 6.14** Total Power Comparison for 80% Area Reduc. ( $b_0=0.37$ ) (Late Stage)

For early stage of the solution, the results are different. The optimized three-zone velocity field gives better results. As the area reduction increases, the difference between FEA results and Hookebooms early solution increases. As it can be seen from the results Dipper's solution does not show a stable behavior.

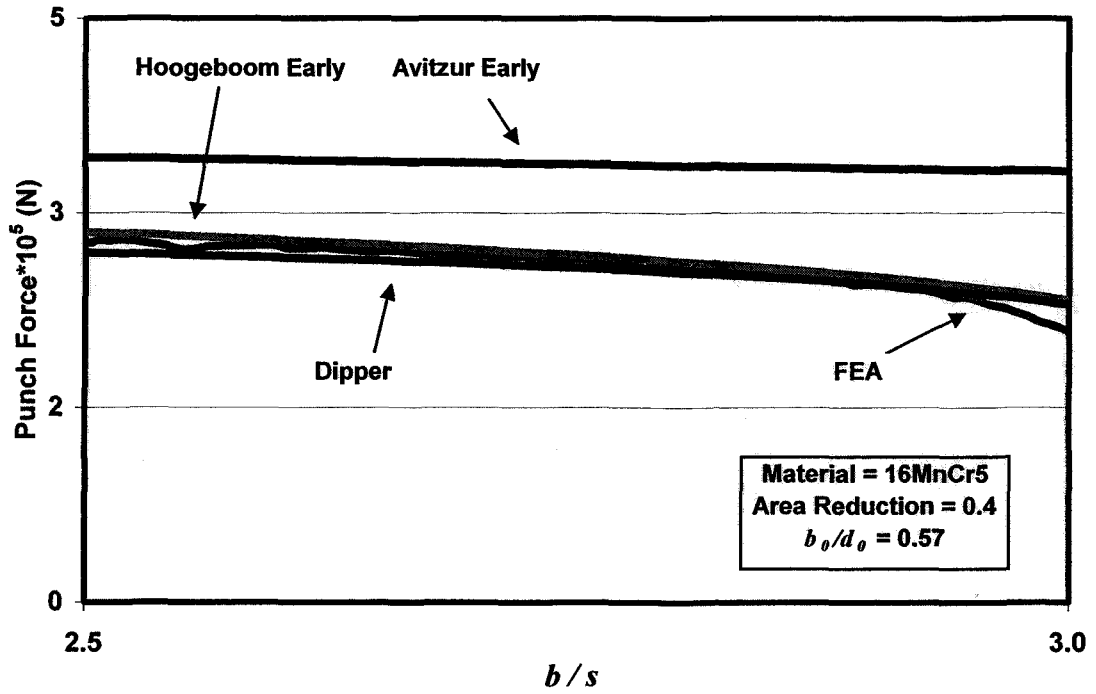


Figure 6.15 Total Power Comparison for 40% Area Reduction (Early Stage)

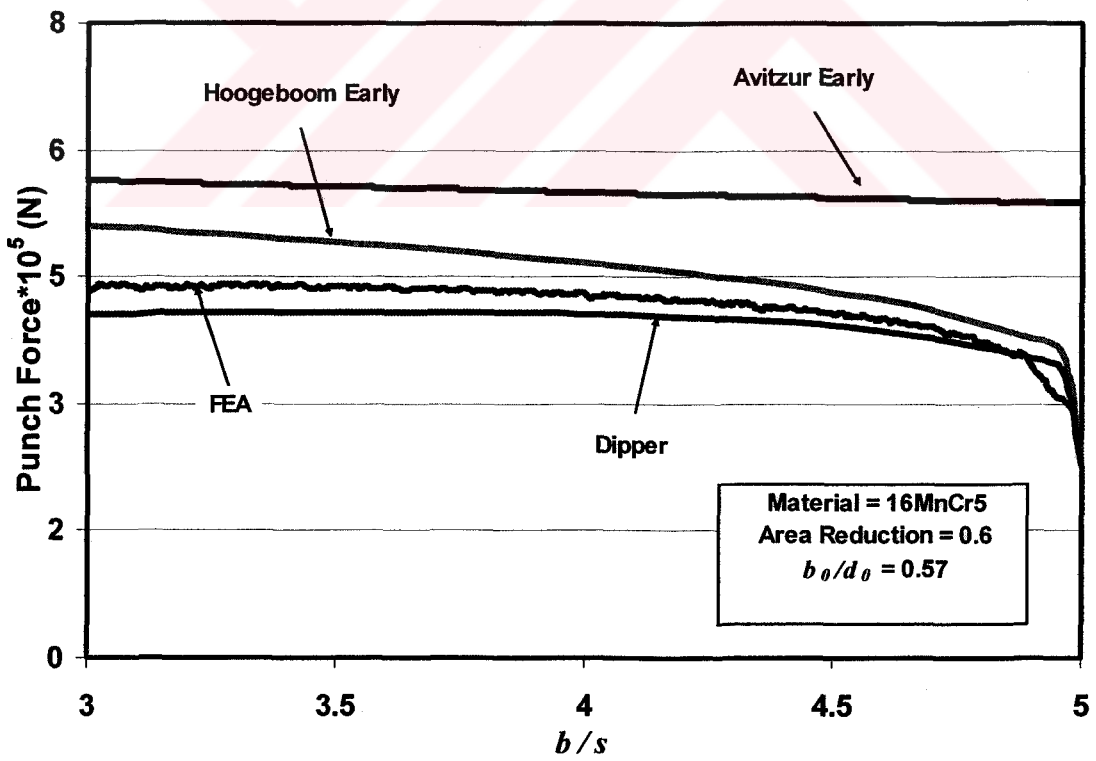


Figure 6.16 Total Power Comparison for 60% Area Reduction (Early Stage)



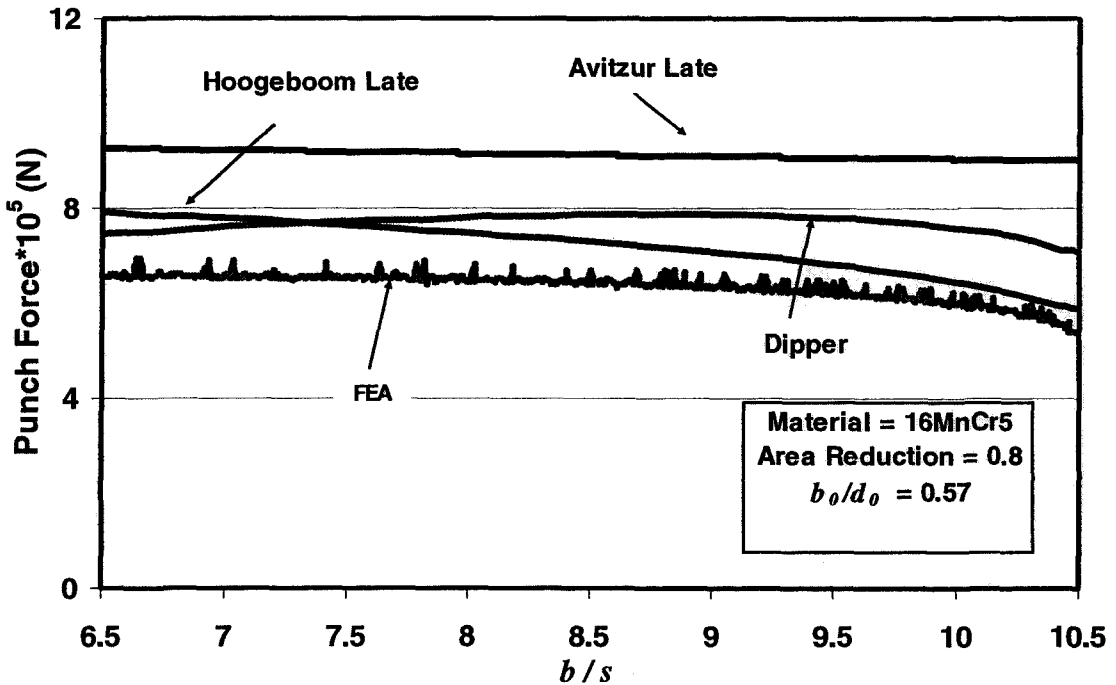


Figure 6.17 Total Power Comparison for 80% Area Reduction (Early Stage)

### 6.6.2 Comparison of Analytical Equations with FEA Results with Friction

In the previous section the comparison of internal deformation and shear terms were taken into account. In real life friction is always present, so it is important to examine the contribution of friction to the total power term for backward can extrusion. In upper bound solutions, shear model is used for friction definition. This value as stated in Chapter 2, can vary between zero and one, depending on the process.

In Figures 6.18-6.20 the results for 16MnCr5 for  $m=0.1$  are tabulated. The results are different from no-friction case. As explained in Chapter 5, the solution by Avitzur worsens when friction is introduced to the system. Hoogenboom's late stage solution predicts much lower forming force. The problem with Avitzur's and Hoogenboom's solution is that they diverge from FEA results as area reduction increases.

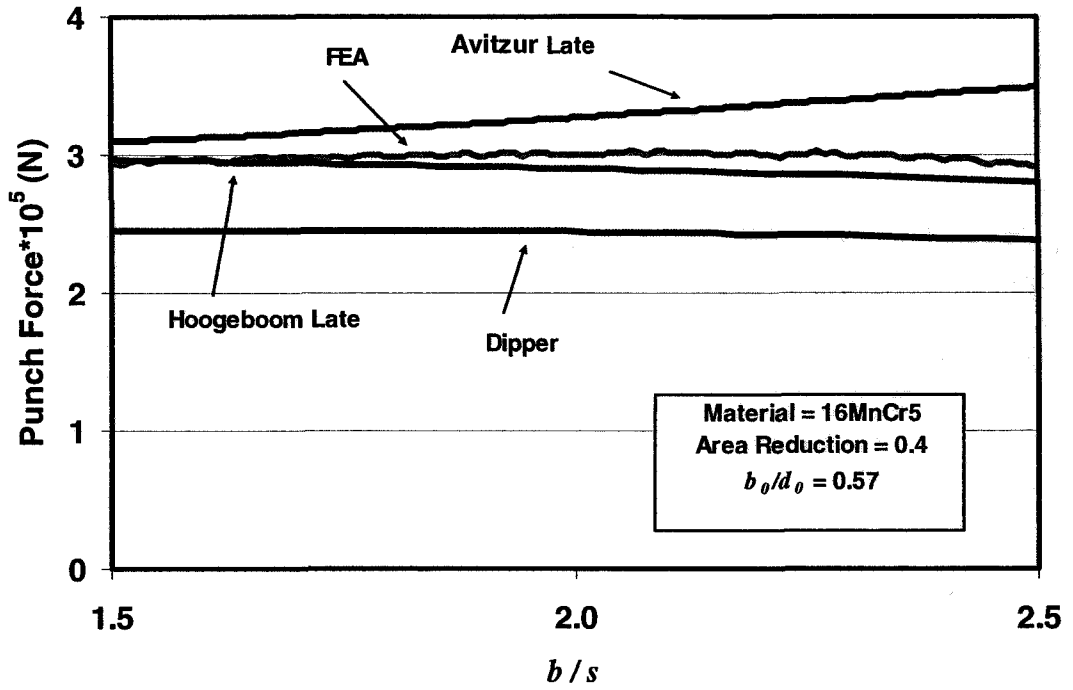


Figure 6.18 Total Power Comparison for 40% Area Reduction for Late Stage ( $m=0.1$ )

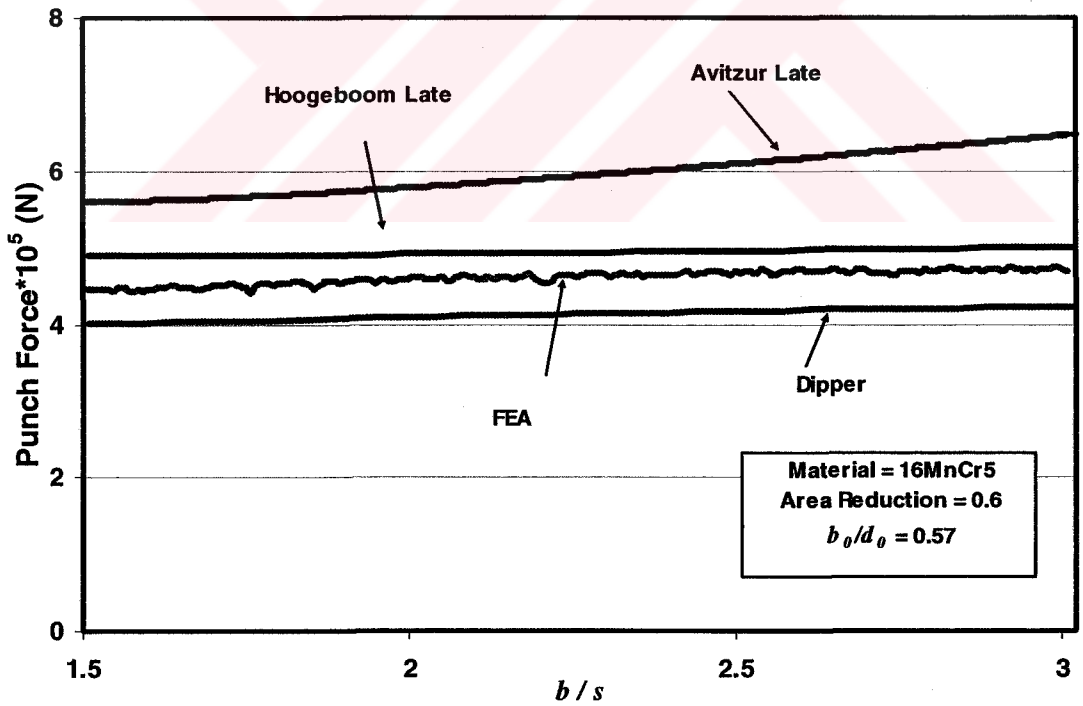


Figure 6.19 Total Power Comparison for 60% Area Reduction for Late Stage ( $m=0.1$ )

As expected Dipper solution improves as the area reduction increases due to its formulation. For late stage and high area reduction Dipper supplies the best solution.

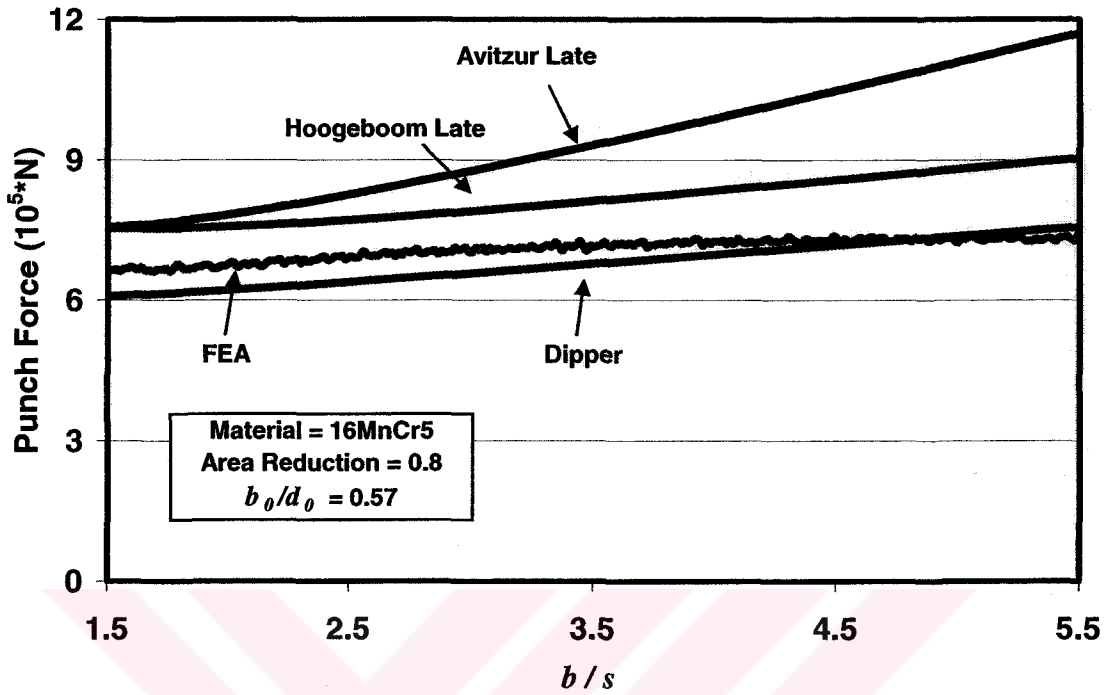


Figure 6.20 Total Power Comparison for 80% Area Reduction for Late Stage ( $m=0.1$ )

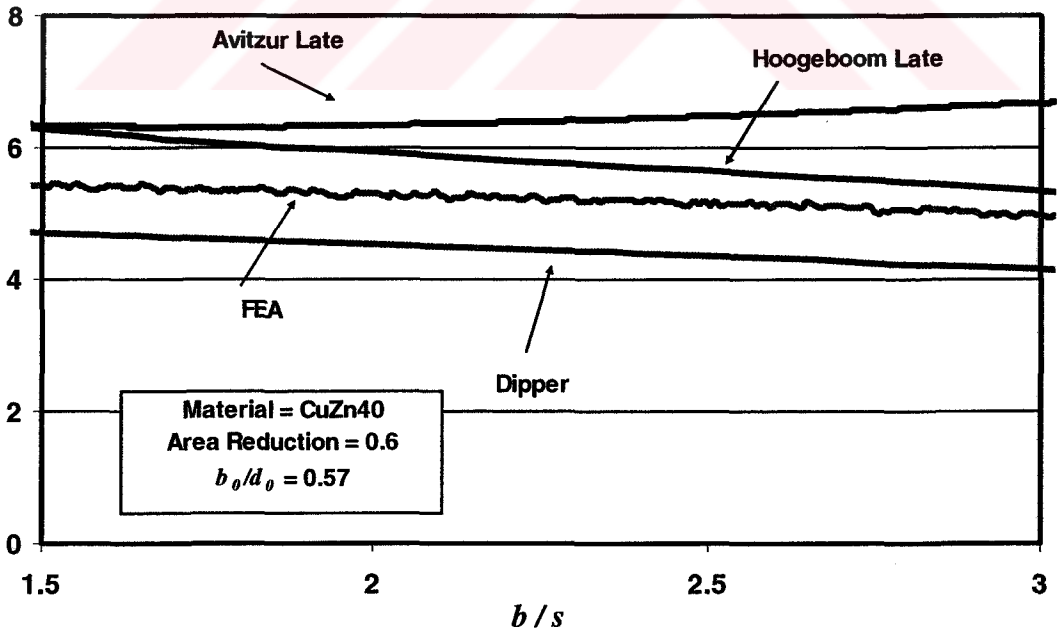
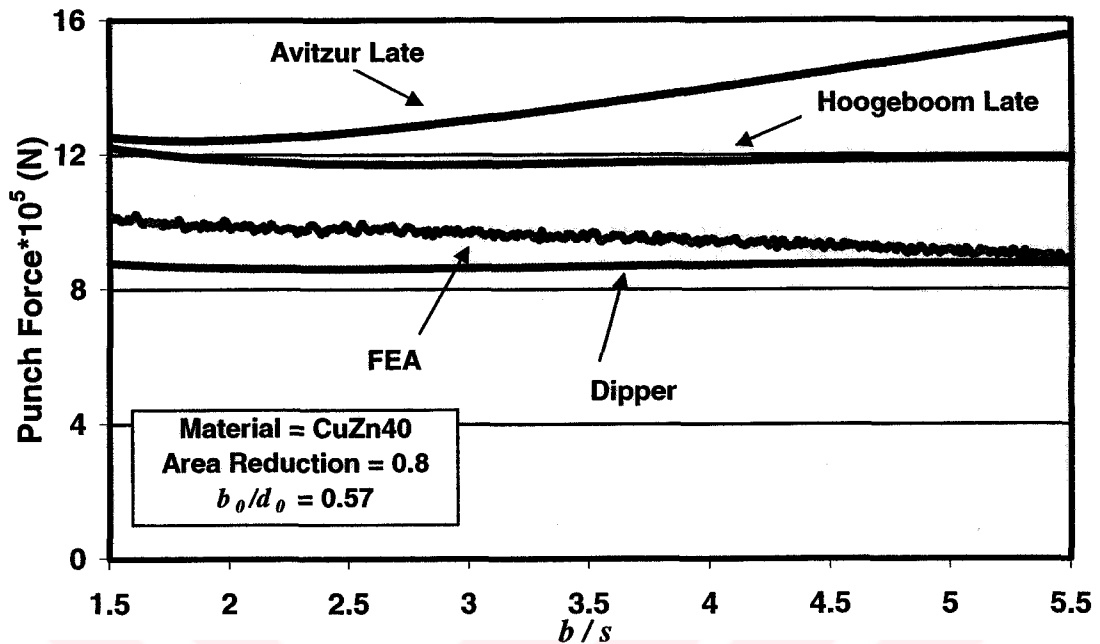


Figure 6.21 Total Power Comparison for 60% Area Reduction for Late Stage ( $m=0.2$ )



**Figure 6.22** Total Power Comparison for 80% Area Reduction for Late Stage ( $m=0.2$ )

In Figure 6.21 and Figure 6.22, the results for CuZn40 for  $m=0.2$  are tabulated. The changes in material and friction factor do not affect the performance of the equations. Dipper's and Hoogenboom's solutions are much better compared to Avitzur's two-zone velocity field. Especially for high area reductions the results obtained from Dipper's formulation are very successful. A set of results for Ck10 is also given in this study in Appendix C.

For the early stage solution, Hoogeboom's optimized three-zone solution is favorable compared to Avitzur's spherical velocity field. The results for 16MnCr 5 and  $m=0.1$  are tabulated in Figures 6.23-6.24. Hoogeboom's solution is very close to FEA results and much stable compared to Dipper's and Avitzur's solutions. Avitzur's early stage solution supplies quite poor results.

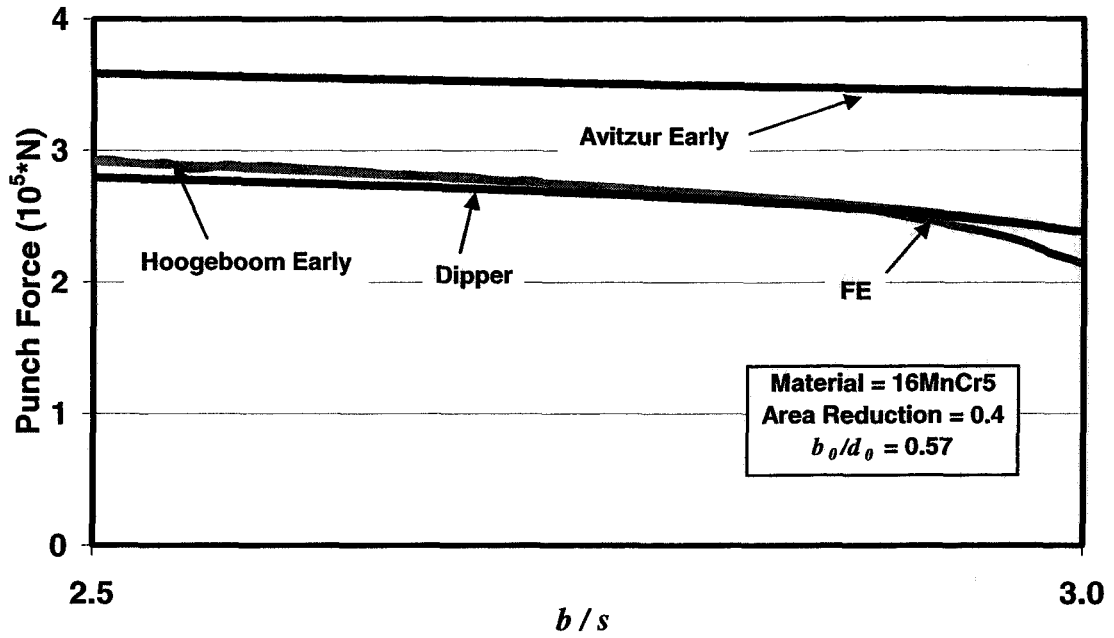


Figure 6.23 Total Power Comparison for 40% Area Reduction for Early Stage ( $m=0.1$ )

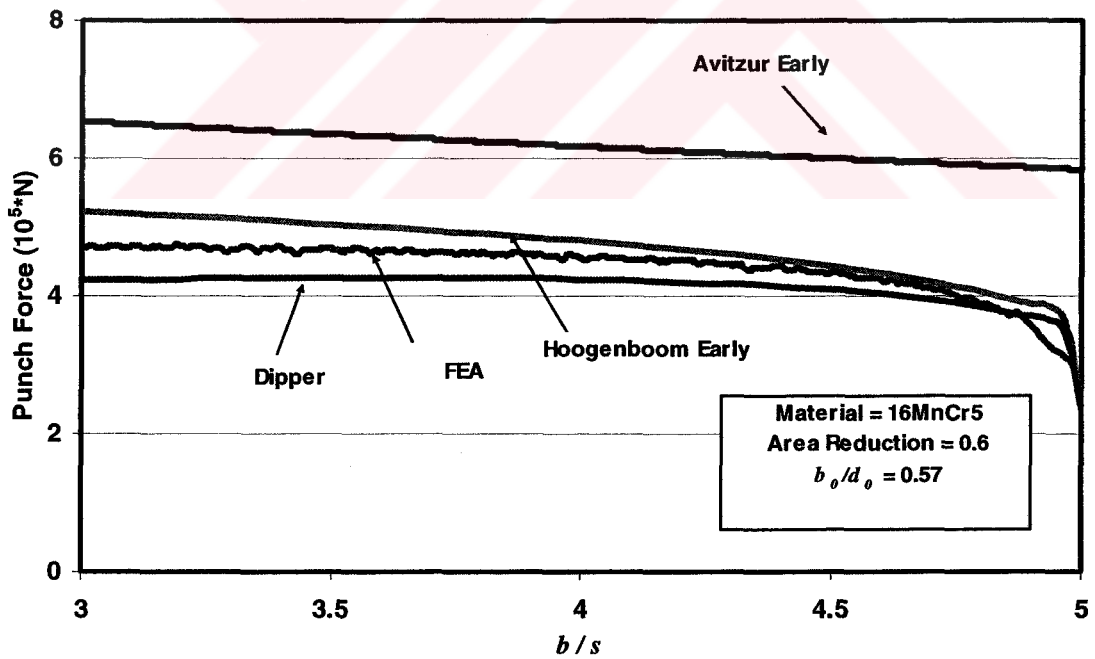


Figure 6.24 Total Power Comparison for 60% Area Reduction for Early Stage ( $m=0.1$ )

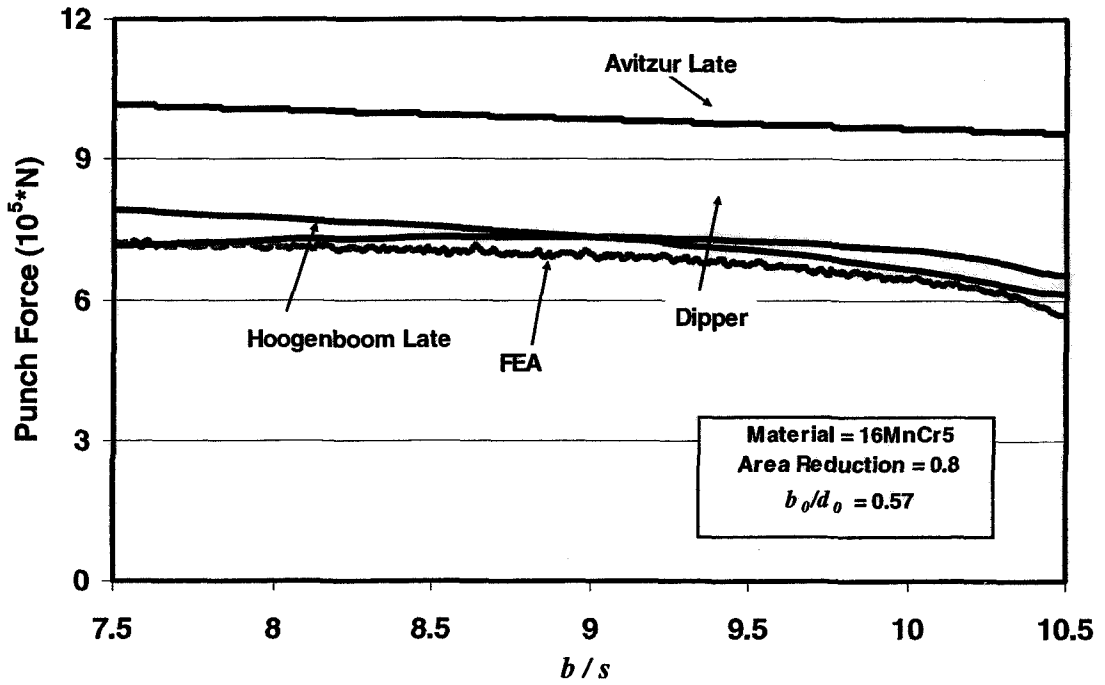


Figure 6.25 Total Power Comparison for 80% Area Reduction for Early Stage ( $m=0.1$ )

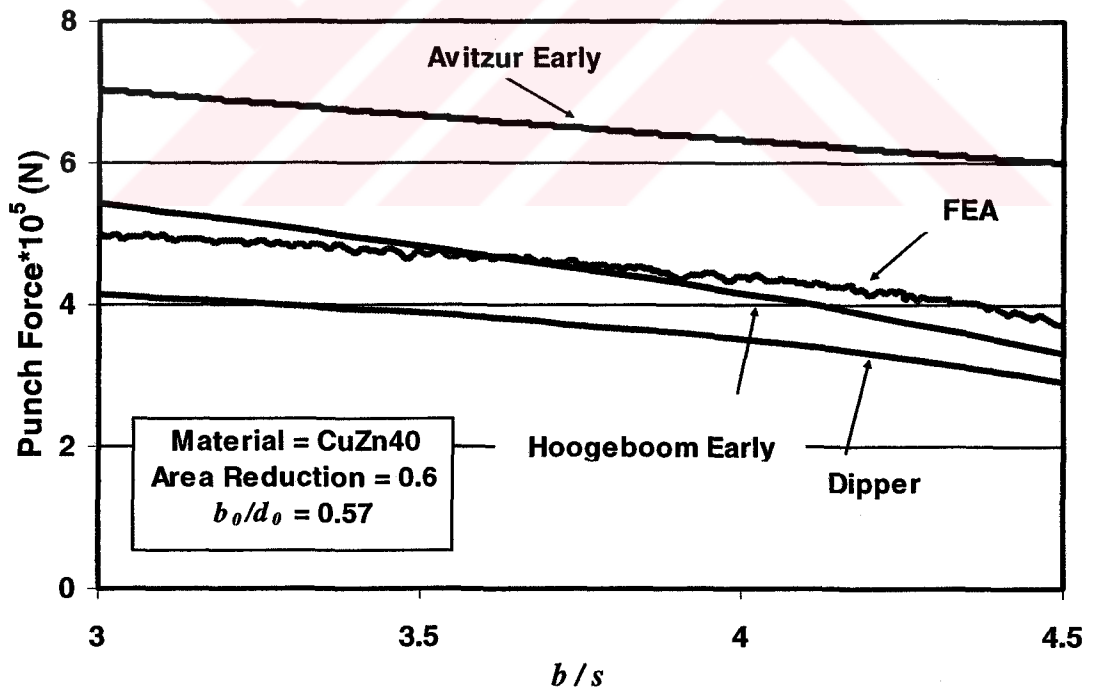
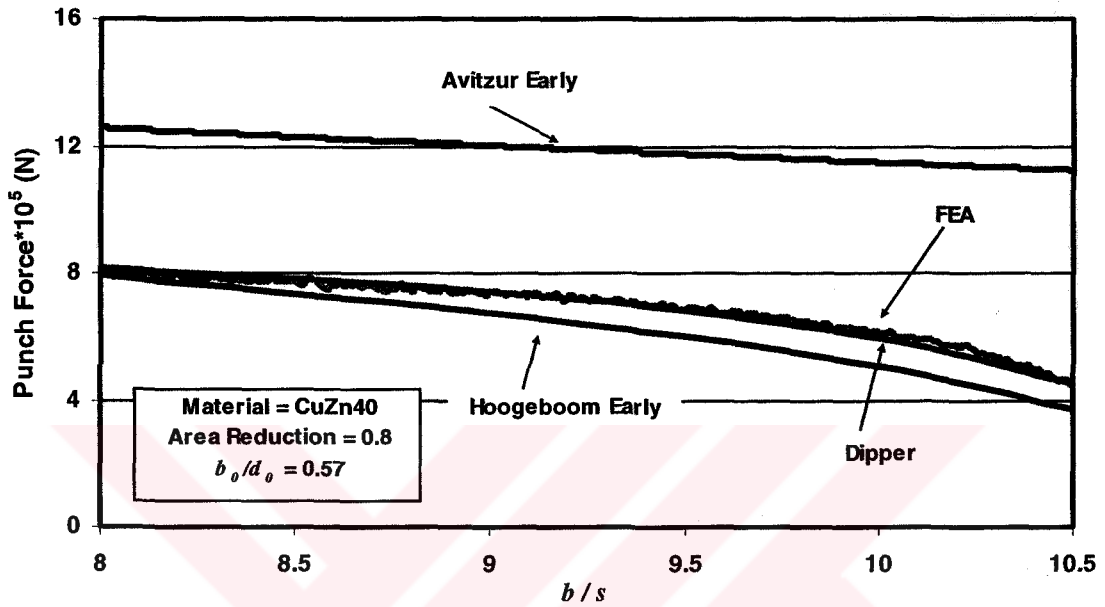


Figure 6.26 Total Power Comparison for 60% Area Reduction for Early Stage ( $m=0.2$ )

As seen in Figures 6.26 and 6.27, the results are not affected when friction factor and material change. When material is changed to CuZn40 and friction factor is set to 0.2, the performance of the analytical equations is the same. The solution of Dipper predicts best results for 80% area reduction. A set of results for Ck10 is also given in this study in Appendix D.



**Figure 6.27** Total Power Comparison for 80% Area Reduction for Early Stage ( $m=0.2$ )

### 6.7 The Effect of Initial Geometry

The geometry of the workpiece has an effect on the total power. The outcome of the variation of the initial geometry of the billet should be examined. For this purpose the initial diameter of the workpiece is kept constant and the initial height ( $b_0$ ) has been varied. The results that are tabulated are for  $b_0$  values of 7.4 mm, 11.4 mm, and 17.4 mm for a billet of 20 mm diameter. As stated in Chapter 5, the effect of initial geometry is valid when the friction between the contact surfaces is present. In case of no-friction for non-hardening materials, the initial billet length has no importance.

For hardening materials that are examined in this chapter, the same conditions are valid. As it can be in the Figure 6.28, for 16MnCr5, the punch force values for late

stage of the process is independent of the initial length of the billet when the friction factor is set to zero. For the case of no-friction, the punch-displacement curve is not affected by the increase in length as it can be seen in Figure 6.28

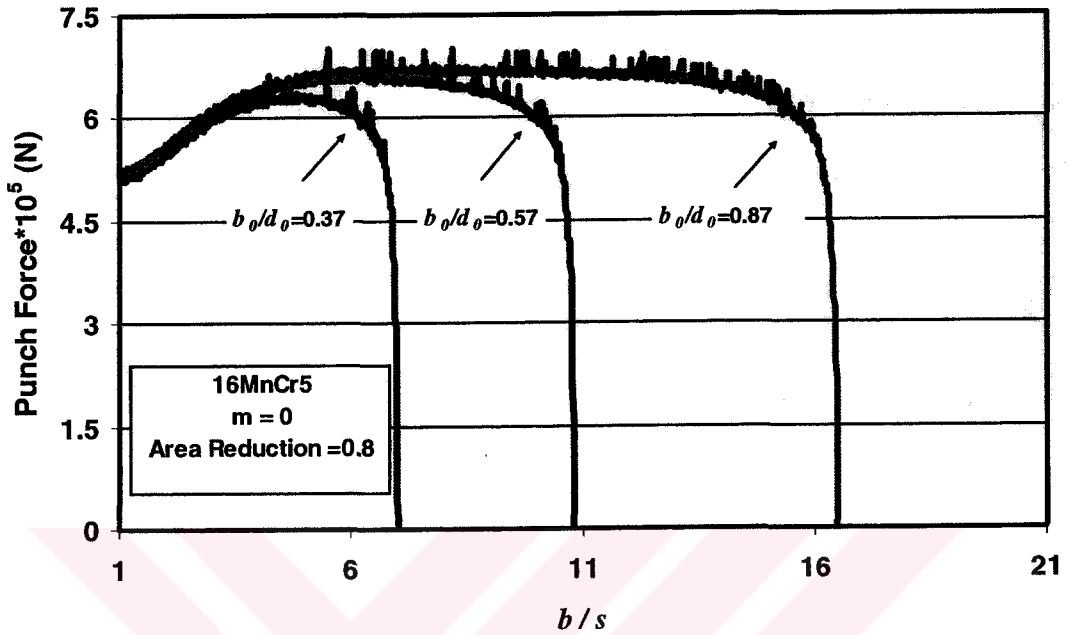


Figure 6.28 Effect of Initial Billet Length ( $m=0$ )

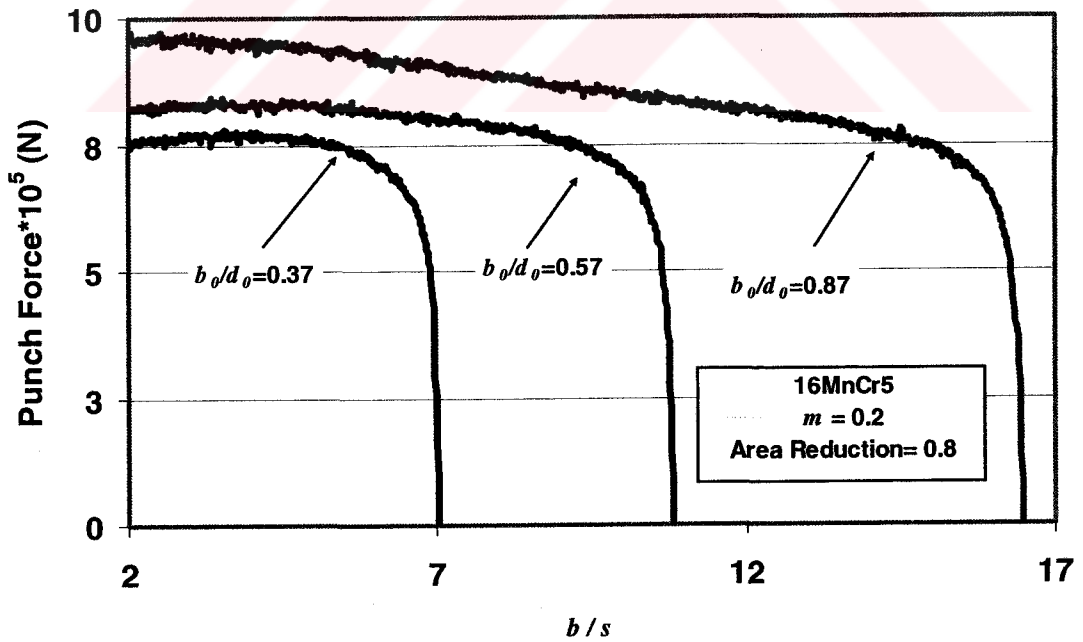
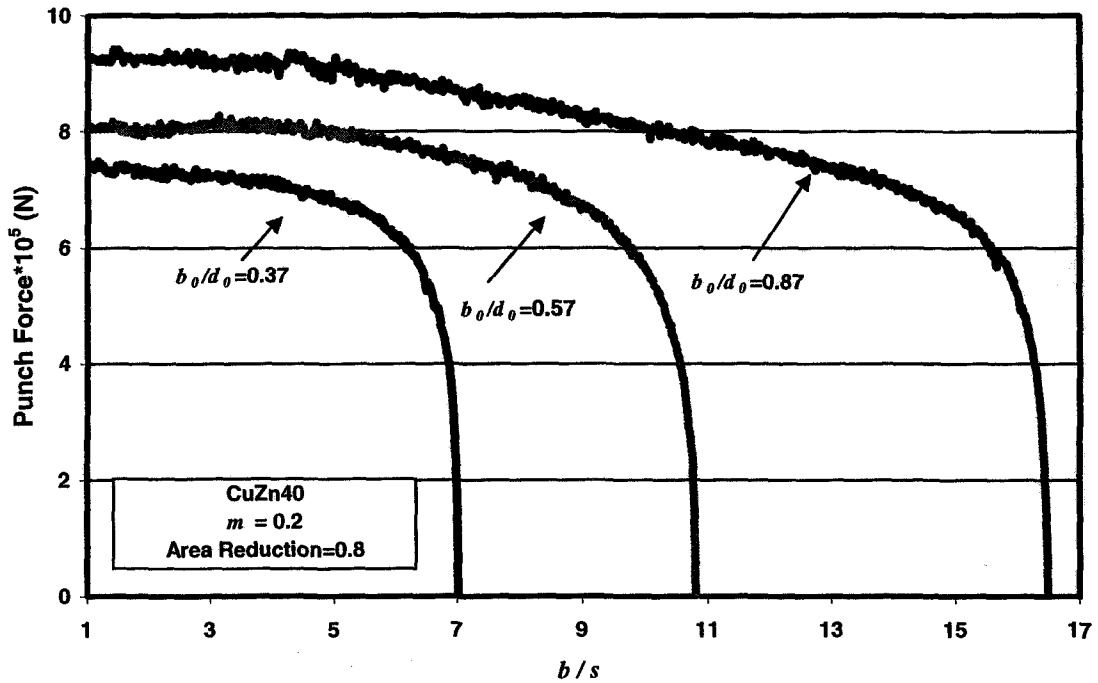


Figure 6.29 Effect of Initial Billet Length for 16MnCr5 ( $m=0.2$ )





**Figure 6.30** Effect of Initial Billet Length for CuZn40 ( $m=0.2$ )

This is due to the fact that the shear and internal deformation terms are independent of the initial height of the billet. As a result changing the initial height of the billet does not affect the total power. The initial geometry becomes a critical factor when friction is present between the surfaces. Increasing contact area results in an increase in the total forming power. As seen in Figures 6.29 and 6.30 for 16MnCr5 and CuZn40, this expected increase is at hand. The solutions by Tekkaya and Hoogenboom, are independent of the initial length as stated in Chapter 5. Avitzur's solution is the only solution that includes this effect.

## CHAPTER 7

### CONCLUSIONS AND DISCUSSIONS

The study has aimed to evaluate the major analytical equations that are available in the literature. In Chapter 3, the formulation of some of those equations is presented together with the derivation of upper bound solution for the three zone velocity field for thick-walled cans which is formulated by the author. The formulations that are used in this study are the elementary solution by Dipper and upper bound solutions by Avitzur and Hoogenboom. In Chapter 5, the assessed equations are compared with finite element analysis results and with each other. The performance of the formulations for various geometries and friction factors are evaluated. In Chapter 6, the non-hardening equations that are evaluated in Chapter 5 are modified using finite element analysis results so that they can be applicable to hardening materials. After the modifications are done, the results of the modified equations are compared with finite element analysis results for various materials, geometries and friction factors.

For three-zone velocity field, there are two types of solution. The thin and thick walled cans are considered for this velocity field definition. The thick walled solution both for late and early stage are derived by the author in Chapter 3. A similar optimization that is done by Hoogenboom (2002) is also done by the author for thick walled solutions:

$$\begin{aligned}
P_{T(early)} = & 1 + \sqrt{\frac{2}{3}} \left\{ \left[ \left( \frac{(r_i + s)^2}{sr_i^2(2r_i + s)} \zeta_3 \right) - \frac{(r_i + s)^2}{s(2r_i + s)} a \tanh \left( \frac{r_i^2}{\zeta_3} \right) \right] \right. \\
& - \left. \left[ \left( \frac{1}{s(2r_i + s)} \zeta_4 \right) - \frac{(r_i + s)^2}{s(2r_i + s)} a \tanh \left( \frac{(r_i + s)^2}{\zeta_4} \right) \right] \right\} \quad (7.1) \\
& + \frac{m+1}{\sqrt{3}} \gamma \left[ \frac{(r_i + s)^2}{r_i(2r_i + s)} \right] + \frac{m+1}{3\sqrt{3}} \frac{r_i}{s} \frac{1}{\gamma} + \frac{2}{\sqrt{3}} \frac{1}{s^2(2r_i + s)} \left[ \frac{s^2(2s + 3r_i)}{3} \right] \frac{1}{\gamma}
\end{aligned}$$

where  $\gamma$  is a free parameter and equal to  $a/s$ .

$$\gamma = \sqrt{\frac{r_i^2(2r_i + s)}{3s(r_i + s)^2} + \frac{2r_i(2s + 3r_i)}{3(r_i + s)^2} \frac{1}{m+1}} \quad (7.2)$$

The performance of the thin and thick walled solutions is evaluated in Chapter 5 and the thin walled solution found out to be supplying better results. As an outcome of this observation, the thin walled solution by Hoogenboom is used for the comparison of results later in the study

The evaluation of the total power terms are separated into two sections. In the first part only internal deformation and shear terms, which are named as the plastic deformation terms, are compared. The contribution of the friction terms to the total power is also examined and the effect of increasing friction is also presented.

In Chapter 6, finite element analysis results are utilized to define a total equivalent plastic strain for Avitzur's upper bound solution. The total equivalent plastic strain values for a deformed geometry are compared with formulation of strain that is defined in the literature with respect to the velocity field given in the solution. The results are used to make non-hardening upper bound solutions applicable to hardening materials.

Initial billet length is also a parameter that was examined in this study. The length of the workpiece becomes important when the friction is valid between the surfaces. The contribution of this parameter to the total force is only considered by Avitzur. For the original upper bound solution which is valid for non-hardening materials the effect of billet length is not so critical but for the hardening case which is shown in Chapter 6, increase of initial billet length results in more drastic changes in the total force.

The backward can extrusion is a two phase process, and for both of the phases various equations supply different results. Both of the stages are compared separately due to the difference in formulations.

The early stage solution by Hoogenboom is superior to other formulations for all conditions. Even though it has been formulated for non-hardening materials, after the modification for hardening materials, the solution behaves very stable for different types of materials and friction factors. The reason for the success of this formulation is due to the optimization done.

The early stage solution by Avitzur, predicts forces that are much higher than the results that are obtained from finite element analysis results. The presence of friction factor increases the gap between finite element analysis results, which is due to the modeling done by Avitzur. The modification done for converting the non-hardening equation to hardening equation is acceptable since the strain that have been obtained from finite element analysis results are very close to calculated values.

The late stage solution by Hoogenboom predicts higher forces compared to finite element analysis results for case of non hardening materials without friction. When friction is introduced to the formulation and the non-hardening solution is modified for hardening materials, it improves but the results lack stability.

The late stage solution by Avitzur is very successful for predicting the punch force behavior of the process. The non-hardening and no friction results are nearly exact. The introduction of friction causes divergence of the solution from FEA results. This can be a result of the friction modeling. For the modified hardening solution, when there is no friction present between the workpiece, the results are reasonable. This proves that the definition of strain and flow stress for the modification is correct.

Dipper's solution provides good results hardening materials. This is due to the fact that the definition of total equivalent strain and flow stress definitions are done clearly. It is superior to other solution for area reductions over 50%. This is the process limit for Dipper. The modification that has been done for friction modeling of Dipper seems to be reasonable referring to results for hardening materials with friction.

The finite element results were extremely helpful for finding the total plastic equivalent strain for the process. In the literature, the area that lies under the punch is assumed to be upsetted axially and the total plastic equivalent strain is defined according to this assumption. Finite element analysis results have proved that this assumption is correct. The punch force-displacement curves that have been obtained from analysis are as expected and clearly shows the decreasing behavior of the punch force for late stage.

## **CHAPTER 8**

### **FURTHER RECOMMENDATIONS**

In the last chapter, further recommendations for individual sections are given.

As recommendation for further studies, the velocity field that has been used for upper bound solutions can be altered. The combination of real life experiments and finite element analysis can be done. The experimental specimens can be examined to define new velocity fields that can lower the total power calculated.

The rigid bodies, the die and the punch can be modeled as elastically deformable tools for more realistic results.

Finally, the effect of punch shapes such as nosed ram can be examined and the results can be compared to finite element analysis results. The analytical calculations for the specified tool geometry can be done. The defects that are formed during the process can also be examined and be cross-check by finite element analysis results.

## REFERENCES

Avitzur, B., 1964, Analysis of Wire Drawing and Extrusion through Dies of Large Cone Angle, *J. Engrg. For Ind., Trans. ASME, Ser. B, Vol. 86*, pp. 305-316.

Avitzur, B., Bishop, E. D., and Hahn, W. C. Jr., 1972, Impact Extrusion-Upper Bound Analysis of Early Stage, *Trans ASME, Ser. B, Vol. 94, No. 4*, pp. 1079-1086.

Avitzur, B., 1979, *Metal Forming; Processes and Analysis*, Robert E. Krieger, Huntington, N.Y.

Avitzur, B., 1983, *Handbook of Metal Forming Processes*, John Wiley & Sons, Inc., New York.

Bay, N., 1983, Surface Stresses in Cold Forward Extrusion, *Annals of the CIRP*, 32/1: 195-199.

Belytschko, T., Liu, W.K., Moran, B., 2000, *Nonlinear finite elements for continua and structures*, John Wiley, New York.

DeGarmo E. P., Black JT., Kohser R. A., 1997, 8<sup>th</sup> Edition, *Prentice-Hall International Inc.*, New Jersey.

Dipper, M., 1949, "Cold Extrusion of Sleeves in Both Theory and Experiment" (*in German*), Dr.-Ing. Thesis, Technische Hochschule, Stuttgart; also *Arch. Eisenhüttenwes.*, 20, 1949, pp.275-286.

Drucker, D.C., Greenberg, H.J., and Prager, W., 1951, "The Safety Factor of an Elastic- Plastic Body in Plane Strain,"; *Journal of Applied Mechanics*, Vol 28, TRANS. ASME, Series E, Vol. 73, No. 4, Dec. 1951, pp. 371-378.

Gardner, R.W., 1958, *Technique and Material for Cold Extrusion*, Society of Automotive Engineers, Preprint 36A, March-April 1958, Evaluating the Producibility of Cold-Extruded Parts, *Tool Engineer*, 41, October 1958.

Hoogenboom, S. M., 2002, Upper Bound Method: Theory and Applications, Lecture Notes, Middle East Technical University, Ankara, Turkey.

Hosford W. F., Caddell R. M., 1983, *Metal Forming, Mechanics and Metallurgy*, Prentice Hall, Englewood Cliffs, New Jersey.

Everhart J. L., 1964, *Impact Extrusion of Metals*, Chemical Publishing Company, Inc, New York.

Johnson, W., Kudo, H., 1962, *The Mechanics of Metal Extrusion*, Manchester University Press, Mancheste

Kılıç, E., Tekkaya, A. E., 1997, *Introduction to Manufacturing Technologies*. Lecture Notes, Mechanical Engineering Department, Middle East Technical University Ankara, Turkey.

Kobayashi, S.; Altan, T., 1989, *Metal Forming and the Finite Element Method*. New York, Oxford University Press.

Kudo, H., 1960, Some Analytical and Experimental Studies of Axisymmetric Cold Forging and Extrusion, Parts I, II, *Internat. J. Mech. Sci.*: Vol. 2, pp. 102-127; Vol. 3, pp. 91-117 (1961)



Lange, K., 1985, Handbook of Metal Forming, Michigan Society of Manufacturing Engineers.

MARC Auto Forge, 1998 Command Reference. Palo Alto, CA, Marc Analysis Research Corporation.

Prager, W., and Hodge, P.G., Jr., 1951, *Theory of Perfectly Plastic Solids*, Wiley, New York

Sachs, G., 1951, A Review of Impact Extrusion and Some Related Processes, Sheet Metal Industries.

Schmitt, G., 1968, Untersuchungen über das Rückwärts-Napffliesspressen von Stahl bei Raumtemperatur, Berichte aus dem Institut für Umformtechnik, Universität Stuttgart, Nr. 7, Girardet, Essen.

Sieber, K., 1952, Developments on the Cold Flow Pressing and Extrusion of Steel, Lubrication Engineering, Machinery.

Tekkaya, A. E. 1999, Introduction to Finite Element Analysis. Lecture :Notes, Mechanical Engineering Department, Middle East Technical University, Ankara, Turkey.

Tekkaya A. E., 2001(a), Finite Element Analysis in Solid Mechanics, Lecture Notes, Middle East Technical University, Ankara, Turkey

Tekkaya A. E., 2001(b), Metal Forming Technology, Lecture Notes, Middle East Technical University, Ankara, Turkey

Tschätsch, H., 1997, Praxiswissen Umformtechnik, Friedr. Vieweg & Sohn Verlagsgesellschaft mbH, Braunschweig, Wiesbaden.

## APPENDIX A

### Upper Bound Solution for Upsetting

The upper bound solution for axis-symmetric upsetting is used for the formulation of the upper bound solutions for backward can extrusion since in Avitzur's (1979) and Hoogenbooms (2002) solutions, the material that lies under the punch is assumed to be upsetted radially.

#### A.1 Axis-symmetric Forming Processes

The conditions defining the axis-symmetry are:

$$\dot{u}_\theta = 0 \quad \text{and} \quad \frac{\partial}{\partial \theta} = 0 \quad (\text{A.1})$$

The strain rate in  $r$ -direction is:

$$\dot{\epsilon}_r = \frac{\partial \dot{u}_r}{\partial r} \quad (\text{A.2})$$

The strain rate in  $\theta$ -direction is:

$$\dot{\epsilon}_\theta = \frac{\dot{u}_r}{r} \quad (\text{A.3})$$

The strain rate in  $z$ -direction is:

$$\dot{\epsilon}_z = \frac{\partial \dot{u}_z}{\partial z} \quad (\text{A.4})$$

The strain rate in  $rz$ -plane is

$$\dot{\epsilon}_{rz} = \frac{1}{2} \left( \frac{\partial \dot{u}_r}{\partial z} + \frac{\partial \dot{u}_z}{\partial r} \right) \quad (\text{A.5})$$

The strain rates for  $z\theta$ -plane and  $r\theta$ -plane are equal to zero.

The total equivalent plastic strain rate is:

$$\dot{\bar{\epsilon}} = \sqrt{\frac{2}{3}(\dot{\epsilon}_r^2 + \dot{\epsilon}_\theta^2 + \dot{\epsilon}_z^2) + 2(\dot{\epsilon}_{\theta r}^2 + \dot{\epsilon}_{\theta z}^2 + \dot{\epsilon}_{zr}^2)} \quad (\text{A.6})$$

The local volume invariancy is given by:

$$\dot{\epsilon}_\theta + \dot{\epsilon}_r + \dot{\epsilon}_z = \frac{\partial \dot{u}_r}{\partial r} + \frac{\dot{u}_r}{r} + \frac{\partial \dot{u}_z}{\partial z} = 0 \quad (\text{A.7})$$

when rewritten it becomes

$$\frac{1}{r}(\dot{u}_r r)_r = -\frac{\partial \dot{u}_z}{\partial z} \quad (\text{A.8})$$

## A.2 Upsetting

The upper bound solution for axis-symmetric upsetting is as follows

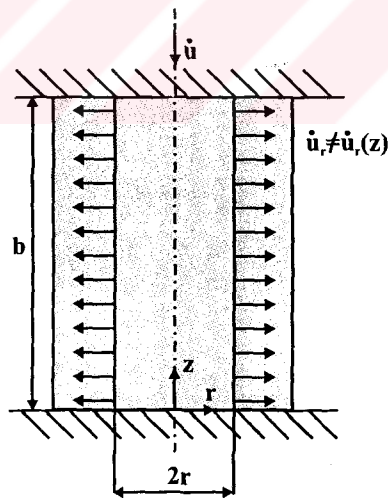


**Figure A.1** Velocity Field for Axis-symmetric Upsetting

The model for velocity field is chosen as

$$\dot{u}_r \neq \dot{u}_r(z) \quad (\text{A.9})$$

The velocity is assumed to be constant in z-direction.

When the global volume invariancy is applied on the volume shown in Figure A.1:

$$\dot{u}_r 2\pi r b = \dot{u} \pi r^2 \quad (\text{A.10})$$

The radial velocity becomes:

$$\dot{u}_r = \dot{u} \frac{r}{b} \quad (\text{A.11})$$

When Eq. (A.11) is substituted into the Eq. (A.8), then it will become

$$\frac{\partial \dot{u}_z}{\partial z} = -\frac{\dot{u}}{b} \quad (\text{A.12})$$

with the boundary condition

$$\dot{u}_{z(z=0)} = 0 \quad (\text{A.13})$$

When both sides of Eq. (A.12) are integrated

$$\int \partial \dot{u}_z = \int_0^z -\frac{\dot{u}}{b} \partial z \quad (\text{A.14})$$

The velocity in z-direction is

$$\dot{u}_z = -\frac{z}{b} \dot{u} \quad (\text{A.15})$$

When Eq. (A.18) and Eq. (A.15) are substituted into Eq. (A.2), Eq. (A.3), Eq. (A.4) and Eq. (A.6), the strain rates are obtained:

$$\dot{\epsilon}_{\theta} = \dot{\epsilon}_r = -\frac{1}{2}\dot{\epsilon}_z = \frac{\dot{u}}{2b} \quad (\text{A.16})$$

and from the Eq. (A.6), the total equivalent average strain rate will be

$$\dot{\bar{\epsilon}} = \sqrt{\frac{2}{3}(\dot{\epsilon}_r^2 + \dot{\epsilon}_{\theta}^2 + \dot{\epsilon}_z^2) + 2(\dot{\epsilon}_{\theta r}^2 + \dot{\epsilon}_{\theta z}^2 + \dot{\epsilon}_{rz}^2)} = \frac{\dot{u}}{b} \quad (\text{A.17})$$

## APPENDIX B

### Material Data

The two types of materials, non-hardening and hardening, that are used in this study have certain properties as tabulated below. For a non hardening material the flow stress is equal to a constant value but for hardening materials, Ludwik's Equation is valid with C and n values tabulated in Table B1 (Tschätsch, 1997).

**Table B.1** Material Data

Material	$\sigma_{f0}$ (MPa)	C (MPa)	n
16MnCr5	402	805	0.11
Ck10	260	730	0.216
CuZn40	240	800	0.33
Mbk6	333	600	0.138
Non-Hardening	402	402	0

The corresponding flow curves of the materials can be seen in Figure B1

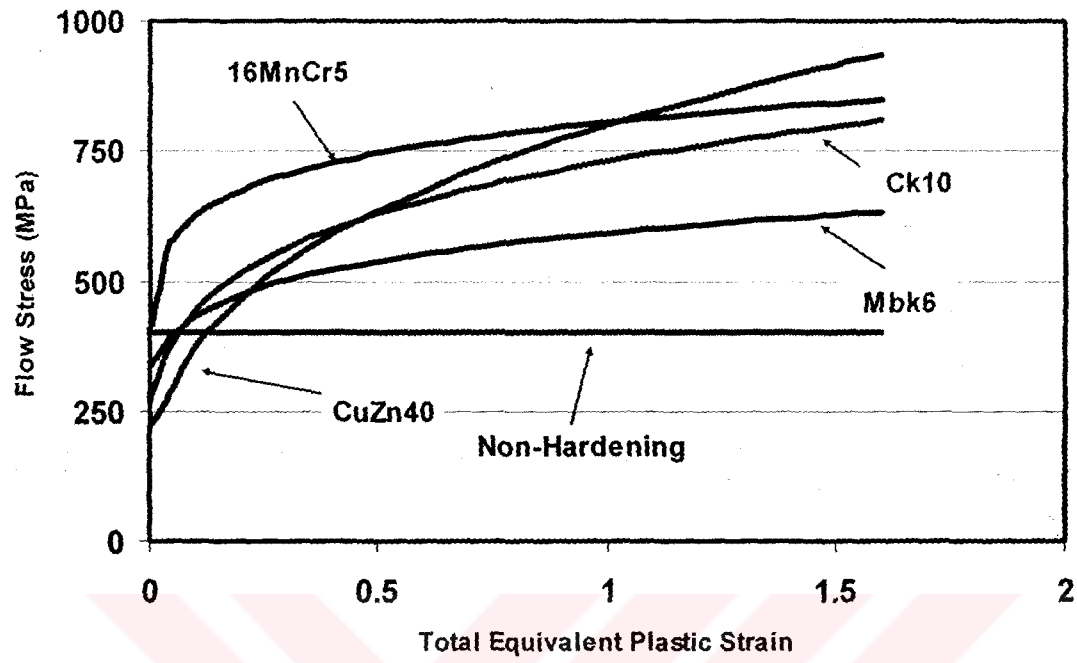


Figure B.1 Flow Curves

## APPENDIX C

### Results for Hardening Materials

The results for Ck10 and friction factor,  $m=0.2$ , are tabulated below:

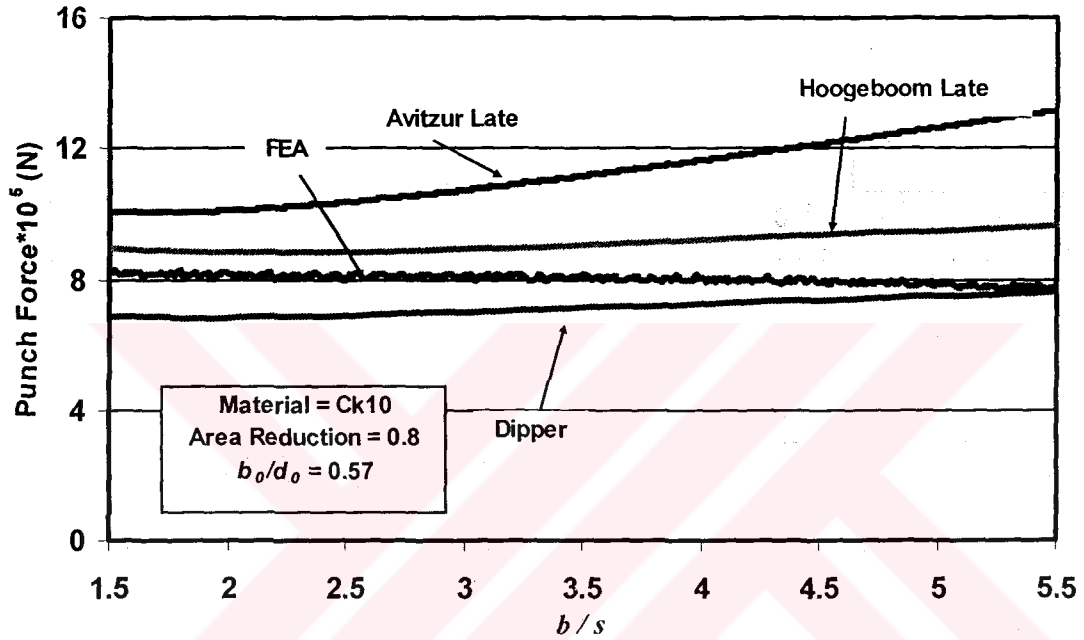


Figure C.1 Total Power Comparison for 80% Area Reduction for Late Stage for Ck10 ( $m=0.2$ )



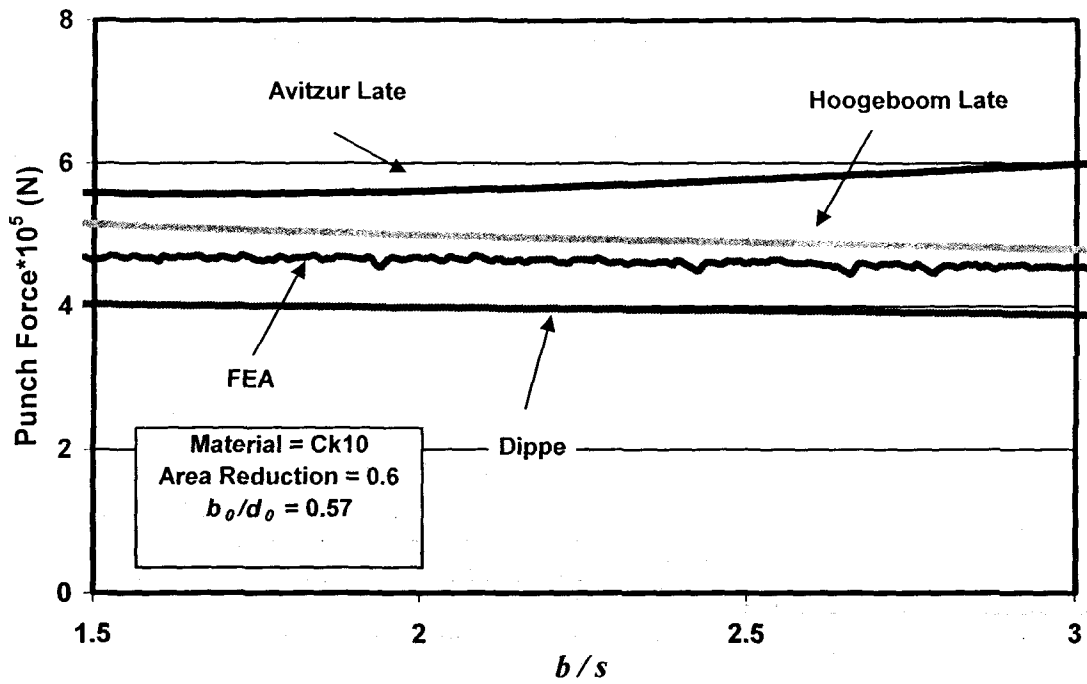


Figure C.2 Total Power Comparison for 60% Area Reduction Late Stage for Ck10 ( $m=0.2$ )

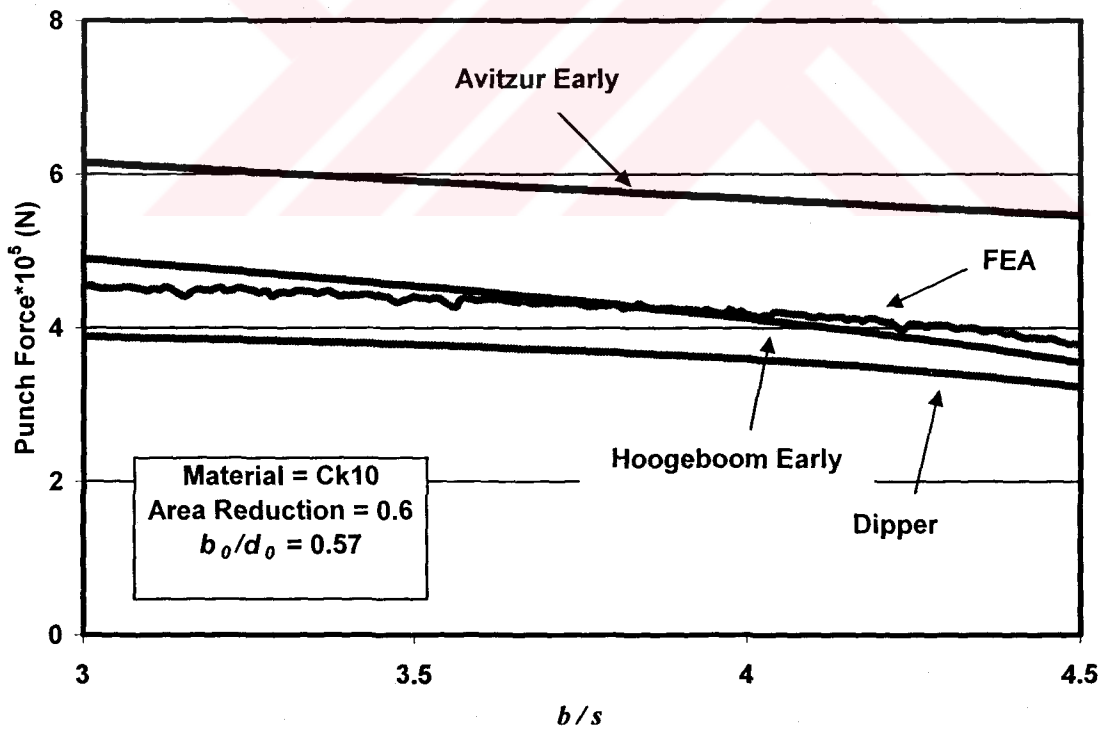


Figure C.3 Total Power Comparison for 60% Area Reduction Early Stage for Ck10 ( $m=0.2$ )

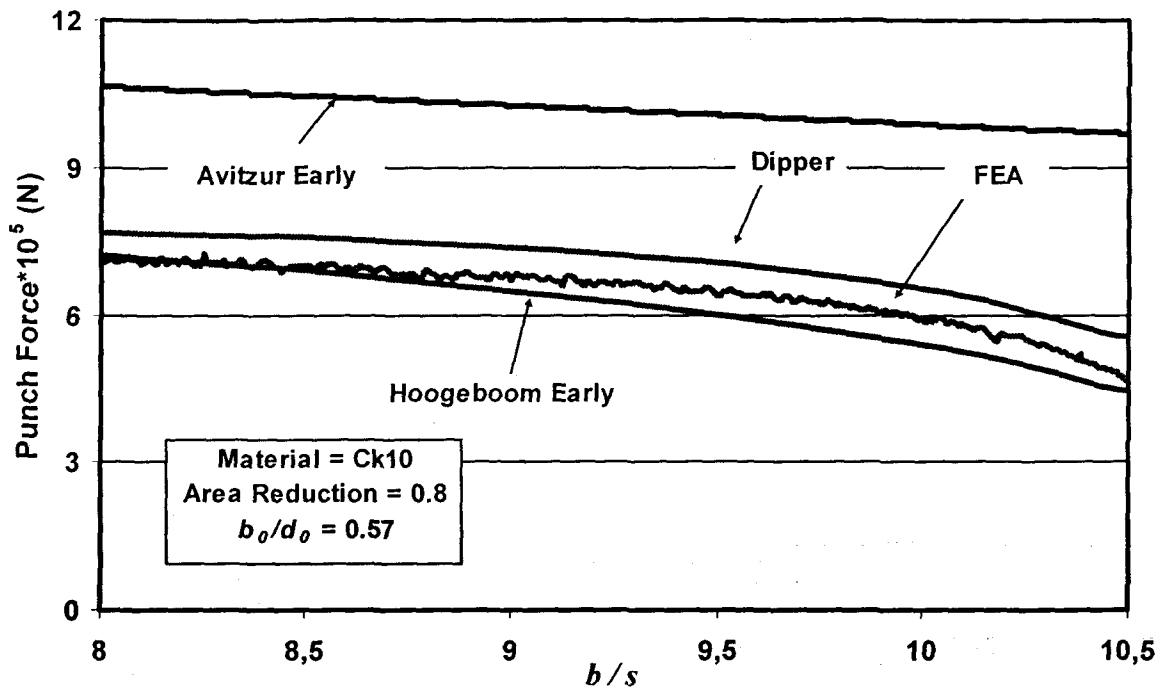


Figure C.4 Total Power Comparison for 80% Area Reduction Early Stage for Ck10 ( $m=0.2$ )

## APPENDIX D

### The Geometry of Punch for Verification Simulations

In this study finite element analysis results are assumed to be the exact value for the forming forces. In chapter 4, the finite element model is checked comparing it with experimental data. Later in Chapter 5 and 6, the results are used for assessment and improvement of analytical equations.

### The Geometry of the Punch for Verification Simulations

The die geometry that is used in Schmitt's (1968) study is different than the geometry used for in Chapter 5 and Chapter 6. The geometry of the punch used for verification of FEA results in Chapter 4 is given in Figure D.1

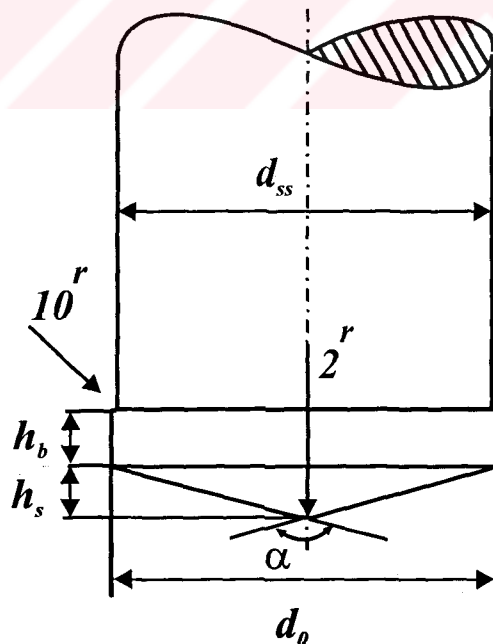


**Figure D.1** Punch Geometry for Experimental Verification

The dimensions are:

$$\alpha=150^\circ \quad d_0 = 30 \text{ mm} \quad d_{ss}=d_0-0.4 \text{ mm} \quad h_b=2 \text{ mm}$$

The area reduction values and their corresponding punch diameters are given in Table D.1.

**Table D.1** Dimensions of Nosed Punch

Area Reduction (%)	$d_i$ (mm)
16	12.0
57	22.7

The dimension of the initial billet geometry is:

**Table D.2** Initial Billet Dimensions for Verification of FEA Results

$b_0/d_0$	$b_0$ (mm)
0.37	11.1
0.67	20.1
1.07	32.1

### The Geometry of the Punch for Assessment of Analytical Equations

The punch geometry that is used for the assessment of the analytical equations has a defined geometry named as flat punch. The tip of the punch is flat as seen in Figure D.2 (Avitzur, 1983). The punch show results a very severe deformation due to its flat geometry. The analytical equations in the literature are derived for this kind of punch

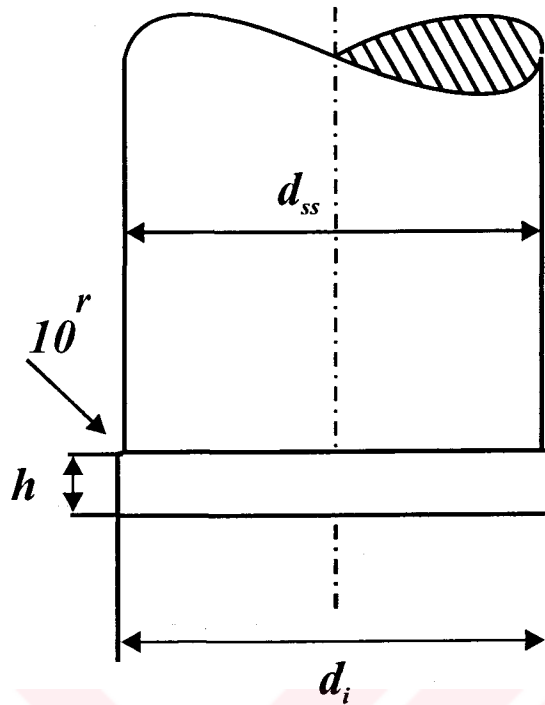


Figure D.2 Flat Punch

The dimensions are:

$$d_{ss} = d_i - 1 \text{ mm}$$

$$h_b = 1.5 \text{ mm}$$

The area reduction values and their corresponding punch diameters are given in Table D.3.

Table D.3 Dimensions of the Flat Punch

Area Reduction (%)	$d_i$ (mm)
40	12.65
50	14.14
60	15.49
70	16.73
80	17.89

The dimension of the initial billet geometry is:

**Table D.4** Initial Billet Dimensions for Flat Punch

$b_0/d_0$	$b_0$ (mm)
0.37	7.4
0.57	11.4
1.07	17.4



## APPENDIX E

### Visual Basic Code

#### E.1 Introduction

In summer 2002, the author of this thesis worked in Neumayer/GmbH for two months for development of a software for calculations of metal forming processes. The tool used for the program was Visual Basic and the interface of the program runs on MsOffice-Excel.

#### E.2 Material Data

The material data is obtained from three different sources:

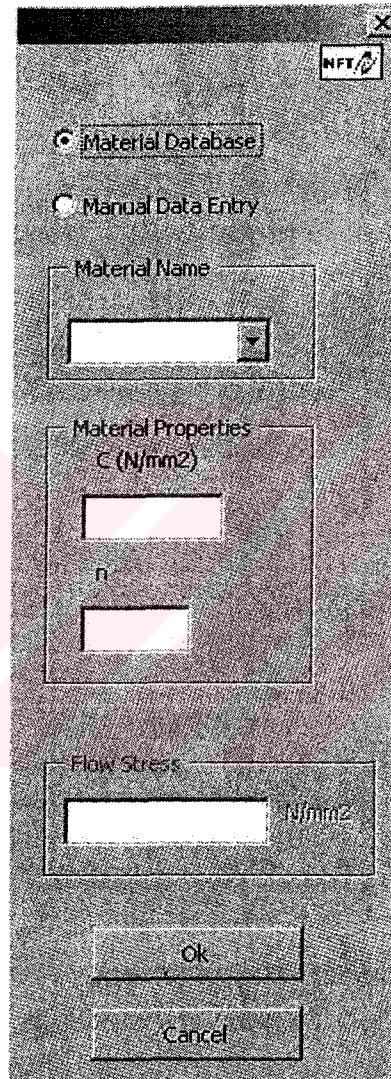
- Flow Curves Atlas (in German)
- The Flow Curves supplied by Neumayer

The program contains material data for both cold and hot forming processes. As soon as material is selected from the pull down menus the related material properties appear on the screen. Since the calculations depend on the material selected the material properties have to be specified before the calculation. For the material selection, the MATERIAL button on the main menu is utilized. If the material properties do not change between the processes then the initially selected material properties will be used by the program. As soon as the material data is updated by the user, new values are used for the calculations.

For cold forming operations, the data which is available are the  $C$  and  $n$  values of the

material (which are obtained by tensile test at 20°C). It is also possible to use a non-

strain hardening material and enter a constant stress value simply by choosing the MANUAL DATA ENTRY option from the menu.



**E.1 Material Database Menu**

For hot forming operations, the data which was taken from the Flow Curves Atlas is used. The range of temperature varies from material to material. The available temperatures from the specific material can be selected from pull down menu. The constant stress value for the specified material and corresponding temperature appear



in the text field. The user can enter external material data, simply by clicking the MANUAL DATA ENTRY option and writing the stress value on the text field.

### E.3 Main Menu

The main menu has eight buttons that helps the user to cruise through the calculations. The MENU button is initially used to enter the initial values for the process and also serves as a mean to for the heading of the printout. The name of the product, customer, date and material name can all be entered to the heading by clicking this button.

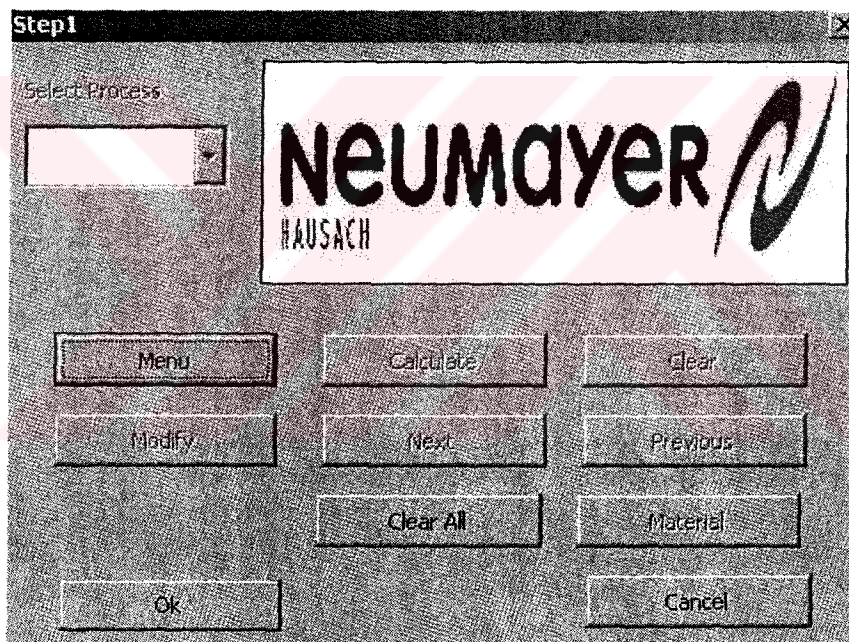


**Figure E.2 Main Menu**

The DELETE button is utilized to clear the data for the process that is active where as DELETE ALL button is used for cleaning the entire worksheet.

The CALCULATE button is used to call the menu for the specified process. It activates the menu for the process that has been selected.

The MATERIAL button is utilized for the selection of material which initially activates a submenu for the selection of the type of material data (COLD or HOT) then once the user selects from the two options available on the sub menu, another submenu for the material properties popup.

The NEXT and PREVIOUS buttons are used for moving back and forth in the calculation chain also gives the user the ability to change the calculation parameters.

The CHANGE button is to modify the process data. It activates the MATERIAL and CALCULATE buttons. The user can directly change the geometrical data by clicking the CALCULATE button. Once this is done, user cannot change the material data since the results are material dependent. If the intention of the user is to change the material data as well as the geometrical data then the MATERIAL button should be selected first.

#### **E.4 Language Selection**

The program can operate in two languages (GERMAN AND ENGLISH). This selection menu is the first menu to popup as soon as the file is opened. The user can select the appropriate language for an easy cruise thorough the calculations. The number of languages can be increased just by adding the necessary words to the SPRACHE worksheets which is in the excel file.

#### **E.4 Saving and Opening a Previous Worksheet**

Once the calculations are complete, simply by saving the file the user can keep the results in the file. If there is need for a change in the calculations following has to be done. The menus that will popup after the language selection asks the user if the previous worksheets should be kept. By pressing YES or NO buttons, one erases or keeps the previous worksheet. Once it is kept then necessary changes can be done.

## E.5 Available Processes

There are 9 processes available in the software:

- Upsetting
- Ring Upsetting
- Forward Rod Extrusion
- Forward Tube Extrusion
- Backward Can Extrusion
- Setting
- Ring Setting
- Setting ( Lens Form)
- Tapering

The screenshot shows a software window titled 'step1' with a 'Daten/Grenze' tab. The interface is divided into several sections:

- Daten:** Includes input fields for 'Reibwert' (friction coefficient), 'Vorverfestigung' (pre-strain), 'rd' (radius), and 'Max. Werkzeugbelastung' (max. tool load) in N/mm.
- Verfahrensgrenzen:** Contains 'Max. Stauchgrad' (max. reduction) set to 1.6, and constraints:  $5 \leq \text{Verhältnis } h_0/d_0 \leq 10$  and  $\text{Verhältnis } d_2/d_1 < 2$ .
- Dimensions:** Fields for diameters  $d_0$ ,  $d_1$ ,  $d_2$  and heights  $h_0$ ,  $h_1$ ,  $h_2$  in mm. A 'Linsenförmig' (lens-shaped) button is present.
- Volumen Berechnung:** Fields for volumes  $V_0$ ,  $V_1$ ,  $V_2$  in mm<sup>3</sup> and 'Volumenabweichung' (volume deviation) in %.
- Diagrams:** Two technical drawings. The left one shows a cylinder with diameter  $d_0$  and height  $h_0$ . The right one shows a tapered cylinder with diameters  $d_0$  and  $d_2$ , and heights  $h_0$ ,  $h_1$ ,  $h_2$ . Volume elements  $V_0$ ,  $V_1$ , and  $V_2$  are indicated.

Figure E.3 Process Data Menu



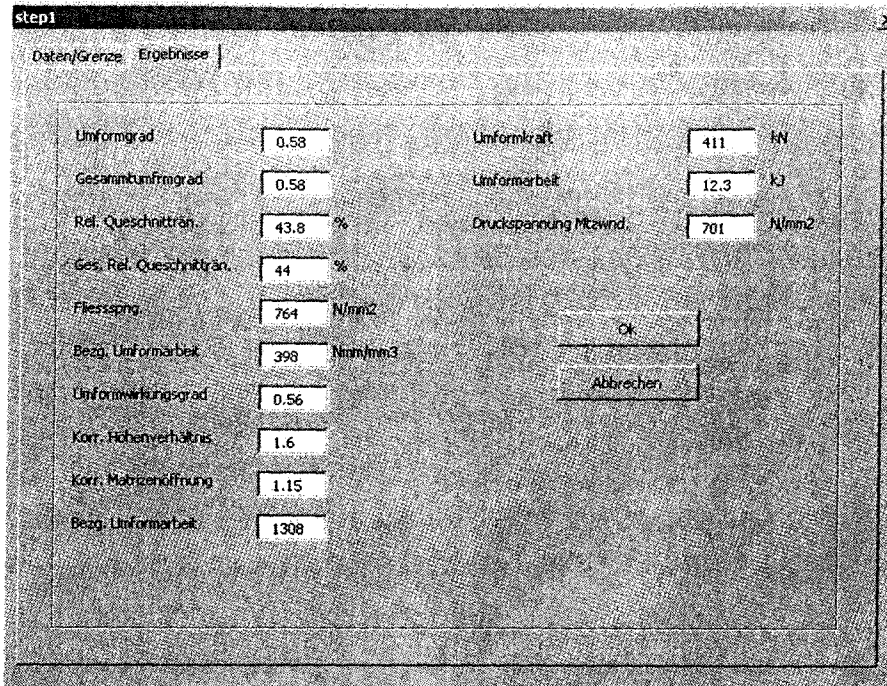


Figure E.4 Process Results Menu

The process parameters, limits and the calculations are formularized within the program. The program warns the user if the process is outside the process boundaries.

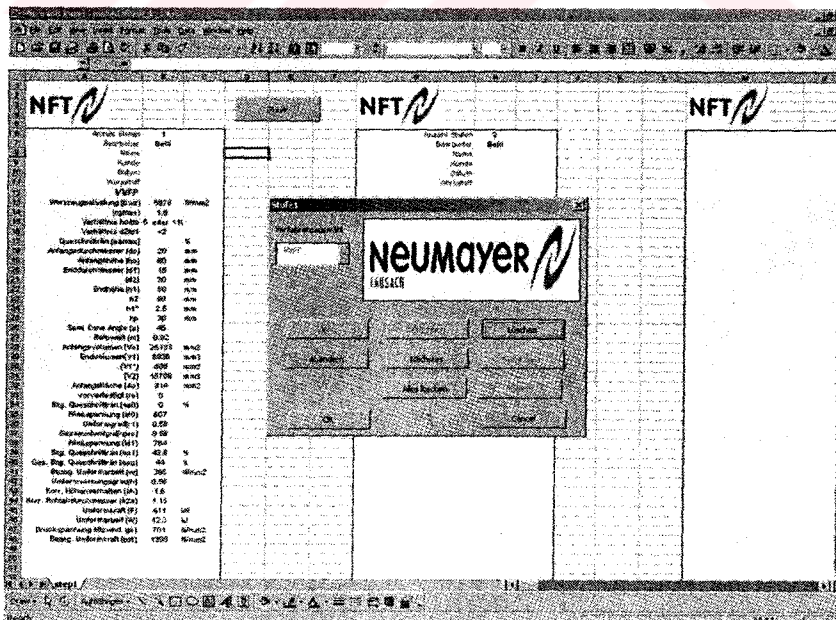


Figure E.5 Excel Worksheet